

University of Southampton

Faculty of Physical Sciences and Engineering

Zepler Institute

**Applications of Femtosecond Laser
Micro-machining for Fabrication of Novel
Optical Sensing Devices**

By

Andrei Donko

May 2020

Thesis submitted for the degree of
Doctor of Philosophy

Research Thesis: Declaration of Authorship

Print name: Andrei Donko

Title of thesis: Applications of Femtosecond Laser Micro-machining for Fabrication of Novel Optical Sensing Devices

I declare that this thesis and the work presented in it are my own and has been generated by me as the result of my own original research.

I confirm that:

1. This work was done wholly or mainly while in candidature for a research degree at this University;
2. Where any part of this thesis has previously been submitted for a degree or any other qualification at this University or any other institution, this has been clearly stated;
3. Where I have consulted the published work of others, this is always clearly attributed;
4. Where I have quoted from the work of others, the source is always given. With the exception of such quotations, this thesis is entirely my own work;
5. I have acknowledged all main sources of help;
6. Where the thesis is based on work done by myself jointly with others, I have made clear exactly what was done by others and what I have contributed myself;
7. Parts of this work have been published as:

Redding, B., Murray, M., Donko, A., Beresna, M., Masoudi, A., and Brambilla, G. (2020) Low-noise distributed acoustic sensing using enhanced backscattering fiber with ultra-low-loss point reflectors. *Optics Express*, 28 (10), 14638-14647.

Donko, A., Nunez-Velazquez, M., Beresna, M., Barua, J. Sahu, G. Brambilla (2018) "Point-by-point femtosecond laser micro-processing of independent core-specific fiber Bragg gratings in a multi-core fiber. *Optics Express*, 26 (2), 2039-2044.

Donko, A., Núñez-Velázquez, M., Barua, P., Guzman Cruz, F., Ismaeel, R., Lee, T., Sahu, J., Beresna, M., and Brambilla, G. (2017) Femtosecond inscription and thermal testing of Bragg gratings in high concentration (40 mol%) Germanium-doped optical fibre. *Optics Express*, 25 (26), 32879-32886.

Signature: Date:

Abstract

University of Southampton
Zepler Institute
Doctor of Philosophy

Applications Of Femtosecond Laser Micro-machining For Fabrication Of Novel Optical Sensing Devices

by Andrei Donko

Recently, femtosecond micro-machining has been established as a powerful fabrication tool for optical devices. Relying on the fundamental mechanisms of multiphoton absorption and avalanche ionisation, transparent bulk materials can be restructured. Subsequently, femtosecond micro-machining has emerged as an alternative to UV-based inscription techniques. The ability to introduce stark refractive index modifications, without the need for a photosensitive material, offers a solution to issues encountered by UV-based methodologies. As the process is intensity dependent, wavelengths that are transparent to polymers can be used, meaning the removal of fibre coating is not necessary prior to inscription. Hence, femtosecond laser writing offers a powerful solution for the fabrication of optical fibre sensing devices.

Exploiting these aspects, a fibre Bragg grating was fabricated in a high concentration (>40 mol%) gemrania fibre using the point-by-point technique. Thermal tests revealed the grating was stable up to 800 °C for 30 minutes. The point-by-point technique offers the advantages of precision and control compared to interferometric based techniques. The precision enabled the inscription of four 3rd order gratings into separate cores of a 7 core multicore optical fibre.

Fibre Bragg gratings are fundamental sensing elements. In particular, recent publications have focussed upon fabricating continuous gratings and grating arrays to improve the signal to noise ratio in distributed acoustic sensing systems (DAS). Traditionally, DAS systems have utilised the Rayleigh backscatter of single mode fibres but their low signal-to-noise ratio (SNR) limits their capabilities. Fabricating low loss, consistent gratings are an engineering challenge.

Femtosecond micro-machining offers a solution to the SNR issue faced by DAS systems. By utilising the smooth refractive index regime, reflectors could be inscribed into the fibre causing a Fresnel reflection of the forward propagating mode. Using this mechanism meant the reflectors were wavelength independent. These intricate low-loss structures were inscribed into a single mode fibre, improving the SNR by up to 23 dB with respect to the Rayleigh backscatter. The fibre was measured to have an attenuation of 1.5×10^{-5} dB/reflector. The fibre was functionally characterised, and compared with standard sensing fibre in two vibration measurements: a phase-based optical time domain reflectometry (ϕ -OTDR) measurement; and an optical frequency domain reflectometry measurement. When the fibre was used in conjunction with the dual-pulse ϕ -OTDR methodology, an immunity to signal fading was demonstrated. This is the first known report of an ultra low-loss, wavelength independent, temperature immune, femtosecond inscribed, enhanced reflectivity fibre.

Acknowledgements

First, and foremost, I would like to thank my PhD supervisors Professor Gilberto Brambilla, Dr Martynas Beresna and Dr Ali Masoudi. Gilberto, thank you for pestering me to apply to Southampton and providing unconditional support through my PhD. Martynas and Ali, thank you for your advice, expertise and patience. Their contribution and continued belief in my abilities as an optical engineer have been invaluable.

I must also recognise my undergraduate supervisor who did not believe in my capabilities to complete a PhD. Without you I would not have had the hunger and determination to complete my course.

I would like to thank all my collaborators who have provided support in completing experiments and assembling my experimental set ups. Thanks to the students from Eindhoven University of Technology: Sjoerd Tunissen, Jian Kok, Gjis Linskens and Frank Bouwmans for assisting with building a solid automated fabrication system. Thank you to Dr Stephen Kreger from Luna Innovations for testing our enhanced reflectivity fibre with his OFDR set up. Thank you to Dr Brandon Redding from the US Naval Research Laboratories for assessing my work with his ϕ -OTDR set up.

I would like to thank all my friends at the Zepler Institute and the University of Southampton for supporting me over the last four years. In particular Alex Wright and Jon Gorecki who have provided emotional support with hours in the Snooker room.

I must take this time to also recognise Laura. Laura assisted with my growth and development as a person at a time that was most needed. Without your help, none of this would have been possible. You are incredible at what you do and I hope you are recognised for the help and support you provide to people.

My final thanks go to my family and Lucy. Thank you for always believing in me and supporting me on this journey. Hopefully this is the beginning rather than the end.

Nomenclature

ϕ -OTDR	- phase optical time domain reflectometry
AOM	- acousto-optic modulator
ADC	- analogue to digital convertor
AMP	- amplifier
BOCDA	- Brillouin optical correlation domain analysis
BOTDA	- Brillouin optical time domain analysis
BOTDR	- Brillouin optical time domain reflectometry
CAD	- computer-aided design
CMOS	- complimentary metal-oxide semiconductor
D	- dichroic mirror
DAS	- distributed acoustic sensing
DS	- diffraction slit
DWDM	- dense wavelength division multiplexer
EDFA	- erbium-doped fibre amplifier
EOM	- electro-optic modulator
ERF	- enhanced reflectivity fibre
F	- fibre
FBG	- fibre Bragg grating
FFT	- fast Fourier transform
FORJ	- fibre optic rotary joint
FUT	- fibre under test
FLOG	- faint long grating
IS	- integrating sphere
ISO	- isolator
LED	- light emitting diode
LS	- laser source
M	- mirror
MZI	- Mach Zehnder interferometer
NA	- numerical aperture
O	- objective
OFDR	- optical frequency domain reflectometry
OSA	- optical spectrum analyser
OSC	- oscilloscope
OSSR	- optical side scattering radiometry
OTDR	- optical time domain reflectometry
PbP	- point by point

PBS	-	polarisation beam splitter
PC	-	polarisation controller
PD	-	photodetector
PG	-	pulse generator
PSO	-	position synchronised output controller
PZT	-	Piezoelectric transducer
SC	-	supercontinuum
SHG	-	second harmonic generation
SMF	-	single mode fibre
TLS	-	tunable laser source
WDM	-	wavelength division multiplexer
WP	-	waveplate

Contents

1	Introduction	1
1.1	Femtosecond Micro-machining	1
1.2	Distributed Fibre Sensing	2
1.3	Research Objectives	3
1.4	Thesis Structure	3
2	Ultrafast Laser Micro-machining	5
2.1	Ultrafast Lasers	5
2.2	Laser-material interaction	6
2.2.1	Free electron plasma formation	6
2.2.2	Energy deposition	7
2.2.3	Modification	8
2.3	Conclusion	11
	Bibliography	13
3	Point-by-point Fibre Bragg Gratings	16
3.1	Introduction	16
3.2	Fibre Bragg Gratings: Fundamental Principles	16
3.3	Bragg Grating Fabrication Techniques	20
3.3.1	Point-by-point femtosecond gratings	20
3.3.2	Multicore fibre Bragg gratings	21
3.3.3	High concentration germanium fibre Bragg gratings	22
3.4	Experimental Methodology	23
3.4.1	Optical Fibre Specification	23
3.4.2	Bragg Grating Fabrication	24
3.4.3	Computational Analysis	26
3.5	Multicore Bragg Gratings	27
3.5.1	Results	27
3.5.2	Conclusions	29
3.6	High concentration Germanium-doped fibre	30
3.6.1	Results	30
3.6.2	Thermal testing	32
3.6.3	Conclusions	34
	Bibliography	35
4	Distributed Acoustic Sensing and Enhanced Signal Fibres: Principles and Literature Review	38
4.1	Introduction	38
4.2	Fundamental Theory of Distributed Fibre Sensing	40
4.2.1	Theory of Light Scattering	40
4.2.2	Comparing Rayleigh and Brillouin Scattering	42

4.3	Distributed Acoustic Sensors - Rayleigh Scattering	42
4.3.1	Optical Time Domain Reflectometry	42
4.3.2	ϕ -Optical Time Domain Reflectometry	43
4.3.3	Optical Frequency Domain Reflectometry	46
4.4	Distributed Acoustic Sensors - Brillouin Based	47
4.4.1	Brillouin Optical Time Domain Reflectometry	47
4.4.2	Brillouin Optical Time Domain Analysis	48
4.4.3	Optical Correlation Domain Analysis	50
4.5	Enhanced Signal Fibres	51
4.5.1	Fibre Bragg Grating Solutions	52
4.5.2	Inscribed Scattering Centres	55
4.6	Conclusions	58
	Bibliography	59
5	Ultra-Low loss Enhanced Signal Fibre	64
5.1	Introduction	64
5.2	Principle of Femtosecond Scatterers	65
5.3	Experimental methodology	67
5.3.1	Fabrication of Reflectors	67
5.3.2	Optical time domain reflectometry	67
5.3.3	Optical side scattering radiometry	68
5.4	Results and Discussion	69
5.4.1	Optical Time Domain Reflectometry	69
5.4.2	Optical Side Scattering Radiometry	70
5.4.3	Reflectivity Variation	71
5.5	Conclusions	72
	Bibliography	74
6	An Automated Reel-to-reel Fabrication System	76
6.1	Introduction	76
6.2	Process Overview	77
6.3	Fibre winding	77
6.3.1	Mechanical Design	78
6.3.2	Software Design	86
6.4	Fibre Positioning	90
6.4.1	The Fibre	90
6.4.2	Camera Configuration	90
6.4.3	The Positioning Process	91
6.4.4	Y-Positioning: Computer Vision Techniques	92
6.4.5	Y-Positioning: Search Logic	96
6.4.6	Z-Focussing	98
6.5	Inscription	100
6.6	OTDR Monitoring	101
6.7	Conclusions	102
	Bibliography	104
7	Distributed Acoustic Sensing: Characterization of Enhanced Reflectivity Fibre	105
7.1	Introduction	105
7.2	Experimental Methodology	106
7.2.1	Reflector Fabrication	106
7.2.2	Distributed Acoustic Sensing Measurement: ϕ -OTDR	106
7.2.3	Distributed Acoustic Sensing Measurement: OFDR	108

7.3	Results and Discussion	109
7.3.1	1 km Sample of ERF: OTDR	109
7.3.2	Reflector Attenuation: Cut-back Measurement	112
7.3.3	Distributed Acoustic Sensing Measurement: ϕ -OTDR	113
7.3.4	Distributed Acoustic Sensing Measurement: OFDR	117
7.4	Conclusions	120
	Bibliography	122
8	Conclusions	124
8.1	Summary	124
8.2	Future Work	125
	Bibliography	127

List of Figures

2.1	Non-linear photoionization processes: a) Multiphoton ionization; b) Avalanche ionization comprised of free carrier absorption, superseded by impact ionization.	7
2.2	Schematic illustration of exciton level and two basic routes for exciton generation: a) Inelastic scattering of the multiphoton-excited electrons; b) Direct resonant absorption of multiple photons [28].	9
2.3	Structural models of perfect SiO ₂ lattice and most-abundant laser-induced defects. Purple spheres, silicon; red, oxygen. Oxygen deficiency centres: E', asymmetrically relaxed oxygen vacancy with an unpaired electron localized in a sp ³ -like orbital of a single silicon atom; ODC(II), divalent Si atom. Oxygen excess centre: NBOHC, oxygen dangling bond [10]. . .	10
3.1	Schematic showing the structure of a uniform Bragg Grating in a waveguide of effective modal index n_{eff} . The black regions indicate areas of larger refractive index separated by period Λ . The periodicity causes the reflection of light corresponding to the Bragg wavelength $\lambda_B = \frac{2n_{eff}\Lambda}{m}$, where m is the order number.	17
3.2	Reflection spectra of an ideal uniform grating with $\kappa L = 8$ (solid) and $\kappa L = 2$ (dotted). Wavelengths have been normalised to λ_{max} , the wavelength of maximum reflection.	17
3.3	The measured transmission spectra of a Gaussian Bragg grating, 5 mm long of a "dc" index change $\overline{\delta n_{eff}} = 2 \times 10^{-3}$, where the uncoated fibre is a) immersed in index matching oil simulating an infinite cladding; b) immersed in glycerine; and c) surrounded by air, thus supporting the propagation of cladding modes. The inset of each figure shows the relation of the surrounding environmental index n_s to the cladding index n_{cl} , as well as a ray diagram of the radiation and cladding modes induced [6]. .	19
3.4	Annotated microscope image of the 7 core MCF cross section used for the fabrication of FBGs.	23
3.5	The refractive index profile of the high concentration germania doped optical fibre.	24
3.6	Schematic diagram of the femtosecond writing arrangement. M - mirror, A - attenuator, DS - diffraction slit, D - dichroic mirror, O - objective lens, F - fibre, SC - Supercontinuum, OSA - Optical Spectrum Analyser, PSO - position synchronised output controller.	24
3.7	a) beam evolution near focus not using slit; b) energy distribution in YZ plane not using slit; c) beam evolution near focus using slit; d) energy distribution in YZ plane using slit where x corresponds with the direction of the beam translation and the waveguide axis [31]	25
3.8	Transmission spectra recorded from cores 2, 3, 4 and 6.	27

3.9	The transmission spectra of the grating inscribed within core 4 of Bragg resonance $\lambda_B = 1532.66 \pm 0.02$ nm. Computational analysis applied a line of best fit and deduced the refractive index modulation associated to the grating planes $\delta n = (2.07 \pm 0.02) \times 10^{-3}$	28
3.10	The transmission spectra of the grating inscribed within core 3 of Bragg resonance $\lambda_B = 1541.01 \pm 0.02$ nm. Computational analysis applied a line of best fit and deduced the refractive index modulation associated to the grating planes $\delta n = (2.92 \pm 0.06) \times 10^{-3}$	29
3.11	The transmission spectra of the high concentration germania-doped FBG.	30
3.12	Simulated x component of the electric field for the HE_{11} , TE_{01} , TM_{01} and HE_{21} modes. The TE_{01} and TE_{01} modes were degenerate with an effective modal index of $n_{eff} = 1.4583$. The HE_{11} and HE_{21} had effective modal indices of $n_{eff} = 1.4850$ and 1.4578 , respectively.	31
3.13	The transmission spectra of the HE_{11} self coupling resonance recorded during the thermal tests for temperatures up to 750 °C.	32
3.14	A thermal sensitivity plot of the high concentration germania fibre. A quadratic regression line (solid) was applied to the data.	33
4.1	Three types of intrinsic optical fibre sensors (a) single point sensor (b) quasi-distributed sensor, and (c) distributed sensor. LS - Laser source; FC - Fibre coupler; PD - Photodetector; BBLS - Broad-band laser source; C - Circulator; FBG - Fibre Bragg grating; PLS Pulsed laser source [1].	39
4.2	A diagram of Brillouin scattering λ_B of incident light λ_p from interacting with thermally generated acoustic wave λ_a [1].	41
4.3	Schematic diagrams of the experimental arrangements for ϕ -OTDR measurements: a) Dual-pulse regime (b) Spatial or time derivative methodology (c) Electrical domain measurement. AOM - Acoustic Optic Modulator [1].	44
4.4	A diagram demonstrating the sensing principle of an interferometric ϕ -OTDR sensor using a) signal gating measurement technique and (b) distributed measurement technique [18].	45
4.5	A schematic of the experimental set up to make an optical frequency domain reflectometry measurement. FFT - Fast Fourier transform [18].	46
4.6	A schematic of an experimental set up to make Brillouin optical time domain reflectometry measurements. EOM - Electro optic modulator; ESA - Electronic Spectrum Analyser [18].	47
4.7	A schematic of an experimental set up to make Brillouin optical time domain analysis measurements. EOM - electro optic modulator; SBS - stimulated Brillouin scattering [18].	48
4.8	A 3D plot of an exemplar Brillouin gain spectrum mapped along a 100 m sensing fibre as a function of Brillouin frequency shift. The quadrature point at the slope of the local gain spectra have been labelled. In the top left, the insert shows the values of the quadrature points over the distance of the fibre [18].	49
4.9	A schematic of a typical Brillouin optical correlation domain analysis set up [18].	50
4.10	A schematic of a FLOG distributed fibre sensor. The basic elements are a frequency tunable laser source, pulse shaping modulator and a circulator. The diagram shows how if a strain or temperature change occurs along the FLOG, a drop in signal will be observed in the back-reflected trace [48].	52

4.11	A schematic of a Talbot interferometer fibre Bragg grating writing set up. The system is a continuous direct writing methodology, interfering the diffractive orders from a phase mask to create a fringe pattern within the optical fibre. The fibre moves at velocity v , whilst the interference pattern is moved using a phase modulator. The modulator is driven by a saw-tooth function of frequency f . [51].	53
4.12	A schematic of a UV-based weak FBG array fabrication set up. For post processing, automated stripping and re-coating of the optical coating is required. The stripping is performed with a CO ₂ laser. It is integral this is done with high precision as not to leave any particulates on the surface of the fibre as this could be detrimental to the quality of grating [60].	54
4.13	A schematic of a UV-phase mask, continuous grating inscription set up. A reel-to-reel methodology is used to print overlapping, chirped gratings to cover a 10 nm bandwidth [41].	55
4.14	A schematic of the experimental set up to fabricate femtosecond voids in polymer optical fibres [68].	56
4.15	Microscope images of femtosecond modifications in GK-40 fibre at focal depths of 100 μm , 200 μm and 300 μm . Each structure was inscribed with a single 5 μJ laser pulse focussed through a 0.6 NA lens [68].	56
4.16	Incoherent-OFDR trace of the 12 scattering voids inscribed in the single mode fibre. [68].	57
4.17	Normalised power spectral density at vibration frequency of 25 Hz at a distance of 80 km for: a) a standard single mode fibre and b) a modified single mode fibre with scattering voids inscribed [71]. The power spectral density has been normalised with respect to that from the Rayleigh backscatter.	57
5.1	A schematic diagram of an interrogating pulse propagating through an unmodified fibre (left) and a fibre with inscribed femtosecond planes (right.) For the enhanced fibre, the spacing of reflecting planes is set to $W/4 < l < W/2$	66
5.2	A schematic of the femtosecond writing set up used to inscribe the reflectors. SHG - second harmonic generation.	67
5.3	A schematic of the OTDR set up. PG - pulse generator; PD - photodetector; and Osc - oscilloscope.	68
5.4	A schematic diagram of the OSSR arrangement [26]. IS - integrating sphere; FUT - fibre under test and PD - photodetector. The experiment was conducted with the assistance of Dr. Sandoghchi.	68
5.5	The captured OTDR power spectrum from the reflector fibre.	69
5.6	The recorded side scattered loss from the OSSR measurement for the enhanced reflector fibre.	70
5.7	The recorded power of the femtosecond laser: after second harmonic generation (blue); and after the microscope objective (orange). Lines of best fit for each data set has been plotted (black).	71
5.8	Photographs of glycerol: before irradiation (left) and after irradiation (right). A white LED was shone through the cover slide to highlight any optical changes.	72

6.1	A flow diagram of the fabrication process of the enhanced reflector fibre. First, the hardware is initialised and calibrated with the assistance of a human. After the fabrication process can begin: first with the unwinding of fibre, followed by placement under a microscope objective, and finally with inscription. To ensure reflectors were being inscribed in the core, real time optical time domain reflectometry is completed.	77
6.2	A schematic diagram of the feeding bobbin (left) and the receiving bobbin (right). The receiving bobbin support occurs after the flexible shaft coupler due to the presence of the connection joint to the OTDR feedback system. The receiving bobbin arrangement is also placed on a single axis translation stage to ensure the fibre is wound evenly.	78
6.3	A force diagram of the tension compensation system where: $2l$ is the distance between the centre of mass of the two stationary pulleys; r_{pulley} is the radius of the pulleys; h_1 is the height from the centre of mass of the pulley located on the carriage, to the plane in line with the stationary pulleys; \vec{F}_n is the normal force acting upon the moveable pulley; \vec{F}_s is the axial tension in the fibre; $\vec{F}_{s,x}$ is the x-component of the axial tension in the fibre; and g is the acceleration due to gravity; m is the mass of the moveable pulley, carriage and reflection plate.	79
6.4	A 3D CAD drawing of the tension compensation pulley. The system comprises of a low friction bearing rail and carriage, with a 3D printed white reflection plate and pulley attached. The carriage had a combined mass of 87g.	80
6.5	A 3D CAD drawing of the distance measurement component.	81
6.6	A graph of the encoder counts recorded when 1600 steps is sent to the stepper motor.	82
6.7	A diagram of the mechanical design within the laser safety enclosure to position fibre beneath the microscope objective.	82
6.8	A diagram illustrating the xz -plane difference between the first and second part of the winding system.	83
6.9	A 3D CAD drawing of the input roller box.	84
6.10	A schematic force diagram of the fibre passing over the y -axis cylinder: on the left, without z axis cylinders; and on the right, with z -axis cylinders. Without the z axis cylinders the axial tension F_t decouples into an x and y component, $F_{t,x}$ and $F_{t,y}$, respectively. This decoupling leads to the fibre slipping down the cylinder, as the cylinder rotates around the y -axis	85
6.11	A 3D CAD drawing of the roller holders located on the z -stages. R1, R2 and R3 are three custom made low friction, rotating cylinders.	85
6.12	The velocity profile of the stepper motors coupled to the feeding and receiving bobbins. The final constant velocity period is variable in duration, altered by learning control algorithms.	87
6.13	A schematic of the station stop control problem. A train is travelling at a constant velocity v_0 , at position s_0 and needs to stop at a station, located at position s_f	88
6.14	Graph of the encoder error for 1000 iterations drawing 0.5 m per iteration (top); and 1 m per iteration (bottom).	88
6.15	A box-plot showing the distribution of errors recorded for the 1000 iteration winding tests of: 0.5 m per iteration (left) and 1 m per iteration (right.) The whiskers of the plots are set at $\pm 2.7\sigma$ and outliers are marked with red crosses.	89

6.16	A diagram of the cross section of the single mode telecommunications fibre used. The fibre is made up of an outer coating (largest grey circle), an inner coating (inner grey circle), cladding (outer white circle) and core (central circle.) The intended inscribed structure is displayed as a black box surrounding the core.	90
6.17	An annotated CMOS image of the single mode telecommunications fibre (Corning SMF-28e.) The fibre has two coatings: the outer (coating 2) for mechanical reinforcement; and the inner (coating) to protect against chemical degradation. The core has been emphasised due to its low contrast.	91
6.18	The image image of the single mode telecommunications fibre (Corning SMF-28e.)	92
6.19	A diagram illustrating how a 3-by-3 median filter is applied to a matrix. On the left is the original matrix, before the median filter is applied. The red highlighted cell shows the pixel that is being processed. The red outlined area shows the 3-by-3 comparison area. On the right is the result after applying the median filter. The white value is the new pixel value - the median of the 9 values that were compared.	93
6.20	A CMOS image of SMF-28e optical fibre (left) and the subsequent binary image (right) after application of the MATLAB Sobel operator and threshold filtering.	93
6.21	A diagram defining the parameters of the Hesse normal transform for a line formed from a series of Cartesian co-ordinates. ρ is the length of a normal from the origin to this line; θ is the orientation of ρ with respect to the x axis. Within MATLAB, the Hough transform algorithm defines negative theta as the orientation of ρ to the negative x axis, increasing in absolute value in a counter-clockwise direction till the y -axis.	94
6.22	The resultant Hough parameter space from the transform performed on the binary image in Fig. 6.20. The maximum points of intersection have been marked with squares.	95
6.23	A summary of all the image processing steps used for the Y-positioning algorithm (from right to left): the image captured by the CMOS camera; the image after a median filter is applied; the binary image outputted after the Sobel filter and thresholding is applied; and the edges (blue) drawn from the lines (green) that were identified by the Hough transform. The red line is the midline of the image.	96
6.24	CMOS images of the core at heights from -30 micron to +30 micron. When the camera is imaging beneath the core, the core-cladding interface appears white. When the camera is imaging above the core, the core cladding interface appears a dark grey. When at the centre of the core, the core cladding interface is barely visible.	98
6.25	Average pixel intensity of the optical fibre at -10 micron (top). The normalised pixel intensity after a high-pass filter was applied (bottom.) The triangular markers show the result of the peak detection algorithm. As peaks were identified immediately, the algorithm has determined the imaging plane lies beneath the core.	98
6.26	A plot of the focus parameter calculated for 201 images from -100 μm below the core to 100 μm above the core. A clear convergence to a minima at the position $z = 0$ is visible demonstrating the suitability of this parameter for focussing.	99

6.27	A schematic diagram of the femtosecond writing set up used for reflector fabrication. M - mirror, A - attenuator, SHG - second harmonic generation, D - dichroic mirror, PBS - polarisation beam splitter, BS - beam stop, O - objective lens, F - fibre, WP - waveplate, PSO - position synchronised output controller, LED - light emitting diode, OTDR - optical time domain reflectometer, CMOS - complimentary metal-oxide semiconductor camera.	100
6.28	A schematic diagram of the OTDR set up used for monitoring the fabrication of the enhanced reflector fibre sample. EOM - electro-optic modulator, DWDM - dense wave division multiplexer, EDF erbium-doped fibre, WDM - wave division multiplexer, AOM - acousto-optic modulator, ISO - isolator, PD - photodiode, AMP - amplifier, OSC - oscilloscope	101
6.29	An image of the OTDR connection to the sample. The connection is maintained via a fibre optic rotary joint which was secured in place using a bespoke 3D-printed part.	102
7.1	A schematic diagram of the dual-pulse ϕ -OTDR arrangement. Two 20 ns pulses, offset by 25 kHz, were combined and launched into the ERF. The back-reflected trace was sent into a polarization diversity receiver. The interference of the two pulses was recorded with a high speed digitizer. .	106
7.2	A schematic of the sensing regions used to measure the PZT oscillation for a) enhanced reflectors and b) the Rayleigh backscatter from unmodified areas. The sensing regions were 2 m in length and separated by a 20 m sensing aperture.	107
7.3	A schematic of the Luna OBR 4600 measurement mechanism. The system is made up of a trigger interferometer, a measurement interferometer and a polarisation diversity receiver. TLS - tunable laser source, PD - photodiode, FUT - fibre under test, PBS - polarisation beam splitter, ADC - analogue to digital convertor PC - polarisation controller. . . .	108
7.4	a)The OTDR trace recorded from the 1.35 km sample. The sample shows 268 signal enhancements with an average reflection of 22.03 db above the Rayleigh backscatter. b) The OTDR trace from 0.5 to 0.75 km showing an error in the fabrication system. No reflector was inscribed at 0.590 km. c) The OTDR trace from 1.43 to 1.63 km. The trace shows the reflector at 1.45 km was ~ 12 dB lower than anticipated. A reflector was expected at 1.57 km, but due to an error in the fabrication system, no structure was inscribed.	110
7.5	A CMOS image of the optical fibre after inscription of a reflector at 0.42 km. No structure was inscribed and damaging of the coating was observed.	111
7.6	A histogram of the reflectivities of the inscribed structures with respect to the Rayleigh backscatter signal. A normal distribution was applied to the data and revealed a mean reflectivity of 22.03 dB and a standard deviation of 0.92 dB.	112
7.7	A graph of the transmitted power as sections of 100 reflectors are removed during a cutback measurement. An exponential line of best fit was applied to the data and revealed an attenuation coefficient, $\alpha_{ERF} = 3.2 \times 10^{-5}$ per reflector.	113
7.8	An OTDR trace of the ERF used for the ϕ -OTDR measurements. The sample had 10 reflectors spaced 20 m apart. The sample was spliced onto 600 m of telecommunication single mode fibre.	113

7.9	a) The measured phase at each position along the fibre. PZT was located between reflector 8 and 9 at ~790 m. b) The phase noise power spectral density at each position along the fibre. A 2 kHz signal is visible at ~790 m.	114
7.10	The induced phase by the PZT as a function of the drive voltage using reflector 8 and 9.	115
7.11	a) The phase noise power spectral density at 3 positions along the fibre: a sensor formed from reflectors 8 and 9; a sensor from the Rayleigh backscatter also covering the region wrapped on the PZT; and a sensor formed from reflectors 9 and 10. The sensor using reflector 9 and 10 show a non-local signal suppression of >50 dB. b) The phase noise power spectral density at 2 positions along the fibre: a sensor formed using reflector 2 and 3; and a sensor using the Rayleigh backscatter 2 m after reflectors 2 and 3.	116
7.12	The phase and amplitude of a) Rayleigh backscatter sensor b) ERF during an experiment where a PZT was driven at 2 KHz and the seed laser was frequency modulated at 100 Hz with a deviation of 10 MHz.	117
7.13	The OFDR trace of back reflected light from the 48 point reflectors. The reflectors were positioned 20 cm apart between 11 and 21 m. The reflectors achieved a mean return loss of -50.5 dB.	118
7.14	The optical phase distribution as a function of distance when measuring a 50 Hz excitation for a) the point reflector array, and c) the Rayleigh scatter sensor. The phase response spectrum from 0 to 1 kHz as a function of distance for b) the point reflector array and d) the Rayleigh scatter sensor.	119
7.15	The power spectral density at a point away from the imparted vibration for a) the Rayleigh scatter sensor with 1×, 2×, 4×, 8× and 16× averaging b) the ERF.	119

List of Tables

3.1	A summary of the computational analysis completed on the FBG transmission spectra	27
-----	---	----

Chapter 1

Introduction

1.1 Femtosecond Micro-machining

In 1996, Hirao's group demonstrated how ultrashort laser pulses could be utilised to fabricate waveguides within bulk silica. Since then, femtosecond micro-machining has evolved rapidly, having been developed by a multitude of research groups across the globe for a range of applications. Previously, sub-picosecond lasers were elaborate pieces of hardware, that could only be found in a research environment and their use was restricted to extensively trained individuals. Technological advancements in laser engineering made high quality, stable, ultrafast light sources readily available. Demonstrations of the Kerr effect and semi-conductor saturable absorbers offered new methods for mode locking a laser. These alternative techniques generated stable sub-picosecond pulse trains of high peak intensities on the order of 10 TWcm^{-2} . At such intensities, light pulses can ionize bulk transparent glass, creating a plasma of free electrons that alters the arrangement and structure of the material. After it cools, a change in the refractive index remains. Unlike longer pulses ($> 10 \text{ ps}$), the effects of irradiation are confined strictly to the focal volume. Heating of the material lattice happens after the pulse has finished, limiting energy deposition to the targeted region. Hence, laser pulses on the femtosecond regime are able to machine precise structures into bulk transparent material on a micro-scale.

Femtosecond micromaching, also used interchangeably with femtosecond writing or femtosecond inscription throughout this piece, holds many advantages over alternative fabrication techniques. Primarily, the scale of the modifications is ideal for applications within photonics. Structures on the order of microns are useful for fabrication of waveguides, manufacture of in-fibre devices and production of optical components such as lenses. The process is direct and as opposed to lithography, it does not require a mask or costly cleanroom facilities. Furthermore, the process is solely dependent on intensity and as such, the wavelength of the machining beam is not of critical importance. Therefore, infrared wavelengths can be selected that are transparent to polymers allowing inscription through the coating of fibres. There is low dependence on the bandgap of the material, meaning the majority of glasses can be modified without a radical changes to the irradiation parameters. The range of media eligible for inscription also extends to crystalline materials and polymers, providing more variety than other techniques. Finally, femtosecond writing is truly three dimensional. It grants more

freedom to fabricate more geometrically complex components by simply moving the sample with respect to the focus. Therefore, fabrication of innovative architecture designs that could not be achieved with other technologies became a reality.

The ability to inscribe stark refractive index contrasts in silica-based glass, without the removal of polymer coatings, makes femtosecond micro-machining an extremely powerful tool in the fabrication of in-fibre devices. The exploitation of femtosecond lasers for grating fabrication has been reported for the last 15 years. However, there in-lies opportunity to demonstrate its full capability by fabricating grating devices in areas where traditional UV-based techniques have struggled. As such, the first part of this piece accentuates two significant benefits of femtosecond micro-machining over its UV counterpart: the ability to machine non-photosensitive materials; and its precision. These were demonstrated with the fabrication of Bragg gratings in a high concentration germania fibre and a multicore fibre.

1.2 Distributed Fibre Sensing

Sensors are an integral part of modern society, allowing accurate monitoring and detection of parameters with minimal human input. Optical fibres have established themselves as a class of sensors due to their ruggedness, accuracy and sensitivity. Under the umbrella of optical fibre sensors sits the subcategory of distributed fibre sensors, which measures parameters over large distances at spatially resolved intervals. Distributed fibre sensors have been demonstrated to determine a host of parameters such as magnetic field strength, temperature and strain. They offer the further benefit of being smaller in size and simpler to implement over large distances than electrical based sensors, which require large power cables in order to function.

Recently, sensors based on the inelastic processes of Raman and Brillouin scattering have been the focus for distributed fibre sensing studies. Both sensor types are relatively simple and highly sensitive, establishing them as the predominant methodologies in several applications such as determining temperature in power cables and strain in large constructions. However, the magnitude of the Raman and Brillouin signals are very low meaning large amounts of averaging are required to make measurements. Consequently, recording a reading with Brillouin or Raman sensors is a relatively long process. Therefore, these systems are only suitable for environments where the parameters are constant or change very slowly with respect to time.

Strain sensors based upon Rayleigh scattering have emerged to fulfil the application shortfalls of Brillouin sensors. Rayleigh sensors have a couple of advantages over its counterparts. First, the stronger magnitude of signal strength can reduce or in some cases, remove entirely the need for averaging. Secondly, the coherent nature of the light is of use for dynamic strain measurements in ϕ -OTDR measurements. Currently, commercial coherent Rayleigh sensors are limited to a range of approximately 100 km. This restriction is due to the attenuation of the weak backscattered signal, caused by the stochastic impurities frozen in the fibre during the fabrication process.

Femtosecond micro-machining has the potential to provide a solution to the issues faced by Rayleigh-based strain sensing systems. An array of Bragg grating solutions have been demonstrated in literature, but provide a wavelength limitation for distributed strain measurements which causes issues in high temperature environments. The wave-

length dependence also puts a limit on the strain that can be detected; wavelength shifts beyond the linewidth of the detectors cannot be detected. Prior to this work, there have been no reports of femtosecond laser writing being utilised to provide a low-loss, wavelength independent, enhanced signal solution for distributed strain sensing measurements. Thus, an opportunity was identified to create such a novel sensing fibre for dynamic strain sensing.

1.3 Research Objectives

The first objective was to fabricate Bragg gratings in fibres that have proven problematic for traditional UV-based fabrication techniques. Using the point-by-point technique, individual grating planes can be inscribed in high concentration germania fibre and a multicore fibre. High concentration germania fibre has proven extremely difficult to fabricate gratings in due to its highly-photosensitive nature. Femtosecond inscription overcomes this issue due to the fundamental mechanisms underpinning it. The point-by-point technique is extremely powerful for multicore writing as individual cores can be targeted. Furthermore, the technique also allowed simple control of the Bragg grating wavelength. Pursuing this work had secondary personal objectives of gaining experience and understanding of fibre-based femtosecond machining.

The second objective was to utilise the smooth refractive index regime of femtosecond writing to fabricate low-loss, wavelength independent reflectors for distributed acoustic sensing applications. Distributed sensing systems suffer from a low signal to noise ratio due to its exploitation of the naturally occurring Rayleigh backscatter. This limits its capabilities and hence, restricts its use to certain applications. Femtosecond laser writing possess the ability to introduce a stark refractive index contrast. The fundamental idea was to replicate the density fluctuations that are frozen in the fibre at its conception by inscribing artificial defects. The magnitude of refractive index change that can be achieved with a femtosecond laser means theoretically, it could be possible to produce a signal enhancement 30 dB greater than the Rayleigh backscatter. This would be extremely beneficial for the oil and gas sector, one of the biggest applications of distributed acoustic sensing systems. The poor signal to noise ratio in this application is further worsened by rugged cabling, employed to protect the fibre from the harsh environment.

1.4 Thesis Structure

The following piece comprises of 7 further chapters detailing critical analysis of literature and the experimental work that was completed.. Below is a short summary of each chapter.

Chapter 2: The theory of femtosecond micro-machining is outlined. A brief history and overview of ultrafast lasers is presented. The fundamental physics of the femtosecond laser-material interaction is described. The formation of free electron plasma, deposition of energy and resultant modification are all outlined.

Chapter 3: The basic principles of fibre Bragg gratings are summarised. A literature review of femtosecond inscribed Bragg gratings is provided. The experimental details of

the point-by-point femtosecond inscribed Bragg gratings fabricated within a multicore fibre and high concentration germania fibre are described.

Chapter 4: The fundamental principles behind distributed fibre sensors are summarised. A literature review of distributed dynamic strain sensors utilising Rayleigh and Brillouin scattering is also provided. After, a detailed review of enhanced signal fibres is presented. Solutions based upon grating technology and scattering regions are critically assessed.

Chapter 5: The concept of an ultra-low loss, femtosecond micro-machined, enhanced reflectivity fibre is experimentally demonstrated. The results of the optical time domain reflectometry and optical side scattering experiments are displayed.

Chapter 6: An automated fabrication system was assembled to produce long lengths of enhanced reflectivity fibre. The chapter covers an explanation of the mechanical components and the logic behind its design. After, the software logic is detailed, including a review of the computer vision and learning control algorithms that were implemented.

Chapter 7: The concept of the enhanced reflectivity fibre presented in Chapter 5 is realised. A 1.35 km sample is interrogated with an optical time domain reflectometry measurement. The attenuation of the enhanced reflectivity fibre is assessed with a cut-back measurement. After, the results of two dynamic strain experiments are presented. Vibrations were measured with a phase optical time domain reflectometry system and an optical frequency domain reflectometry system. A comparison with standard single mode sensing fibre is detailed.

Chapter 8: A summary of the results and conclusions from the experimental work conducted. An outlook of the future for enhanced reflectivity fibres and potential future work is discussed.

Chapter 2

Ultrafast Laser Micro-machining

2.1 Ultrafast Lasers

Femtosecond micromachining would not be possible without the developments in laser engineering over the last 40 years. The seminal demonstration of a Ti:sapphire Kerr-lens mode-locked (KLM) laser, achieving a < 60 fs pulse, led to its widespread use in early femtosecond writing experiments. More recently, the Ti:sapphire laser has fallen out of favour to various crystalline gain media lasers, which are based upon rare-earth-ion doping (Nd^{3+} ; Yb^{3+} ; Er^{3+} ; Tm^{3+} ; Ho^{3+}) [1]. The Ti:Sapphire laser has a short upper state lifetime requiring a high intensity pump. Hence, these lasers require more complex pumping architecture, such as a frequency doubled neodymium-doped yttrium aluminium garnet (Nd:YAG), to meet the necessary threshold intensity. The rare-earth-ion systems are pumped by much simpler laser diodes increasing the system efficiency whilst decreasing their size. Despite these systems providing a smaller gain bandwidth, their improved stability makes them suitable for precise and controlled laser micro-machining. A ytterbium-doped potassium gadolinium tungstate (Yb:KGW) crystal can deliver pulse energies of millijoules at variable repetition rates (1 kHz - 2 MHz), with a temporal pulse duration of hundreds of femtoseconds. These parameters are more than sufficient for material processing.

Fibre lasers are emerging as the other alternative to solid state lasers. The large area of the gain medium (fibre core) grants them attractive thermal management properties; simple air cooling is required for stable operation. They also possess very good beam quality due to their formation within a fibre. Pulses of the order tens of femtoseconds have been achieved with microjoule pulse energies[2]. Typically, fibre lasers operate at > 1 MHz meaning the time between pulses is shorter than the heat diffusion time, causing undesirable heat accumulation effects for waveguide writing [3, 4]. The introduction of a Pockels cell into these systems permits lower repetition rates to be achieved. Recently, advantages have been identified for operating at GHz frequencies for ablation and drilling applications [5].

2.2 Laser-material interaction

In 1996 Davis et al. focussed sub-picosecond pulses beneath the surface of a transparent glass substrate and observed a refractive index change in the focal region [6]. As the laser - material interaction is highly non-linear in nature, the effects are confined strictly to the focal volume. High intensity is required on the order of TWcm^{-2} . After the pulse is absorbed, excited electrons lose their energy to the material lattice causing a change in refractive index. The process can be subdivided into 3 processes: free electron plasma formation, energy deposition and material modification.

2.2.1 Free electron plasma formation

Nonlinear photoionization

Photoionization is the excitation of electrons via a laser electric field. Electrons within the material are promoted from the valence band to the conduction band via two processes: non-linear photoionization and avalanche ionisation. Laser pulses of visible or near-IR wavelengths do not have enough energy to directly promote electrons. The bandgap of fused silica is ~ 9 eV whereas a $1 \mu\text{m}$ photon has an energy $E = h\nu \sim 1.2$ eV, where h is Planck's constant and ν the photon frequency. Depending on the intensity and repetition rate of the laser, non-linear photoionization in the form of multiphoton absorption and quantum tunnelling can occur [7]. In multiphoton absorption, multiple photons simultaneously excite an electron from the valence band into the conduction band (Fig. 2.1). To surpass the bandgap of the material E_g , the electron must absorb m photons such that $m h\nu > E_g$. Multiphoton absorption dominates at high laser intensity and low frequency. At low laser intensity and high frequency, quantum tunnelling dominates. The large electric field warps the band structure and thus, reduces the potential barrier. This increases the probability of electrons tunnelling from the valence band to the conduction band. The balance of these two non-linear photoionization processes can be described by the Keldysh parameter [8]:

$$\gamma = \frac{\omega}{e} \sqrt{\frac{m_e c n \epsilon_0 E_g}{I}} \quad (2.1)$$

where ω is the laser frequency, I is the laser intensity at the focus, m_e is the mass of an electron, c is the speed of light in a vacuum, e is the fundamental charge of an electron, n is the refractive index and ϵ_0 is the relative permittivity of free space. If $\gamma \ll 1.5$, tunnelling dominates. If $\gamma \gg 1.5$, multiphoton ionization dominates. If $\gamma \sim 1.5$, photoionization consists of a balance between both processes. For waveguide fabrication, $\gamma \sim 1$ and is therefore a combination of tunnelling and multiphoton ionisation [9]. The Keldysh parameter was calculated for the system used in this work. For the Fibre Bragg gratings fabricated in Chapter 3, $\gamma \sim 0.3$, indicating tunnelling was predominantly responsible. For the fabrication of the devices in Chapter 7, the Keldysh parameter was ~ 1 , indicating both processes were responsible for the resultant index change. In the multiphoton regime, the rate of photoionization $P_{PI}(I)$, is highly dependent on intensity I such that:

$$P_{PI}(I) = \sigma_k I^k \quad (2.2)$$

where σ_k is the multiphoton absorption coefficient for k photon absorption. Equation 2.2 informs us that the process is more efficient for shorter pulses. If the pulse duration

becomes too long ($> \text{ns}$), the excitation process becomes dependent on impurities whose energy levels lie in close proximity to the conduction band. As the impurity location is random, the process becomes less exact and thus, the properties of the resultant modification cannot be accurately predicted [10].

Avalanche ionisation

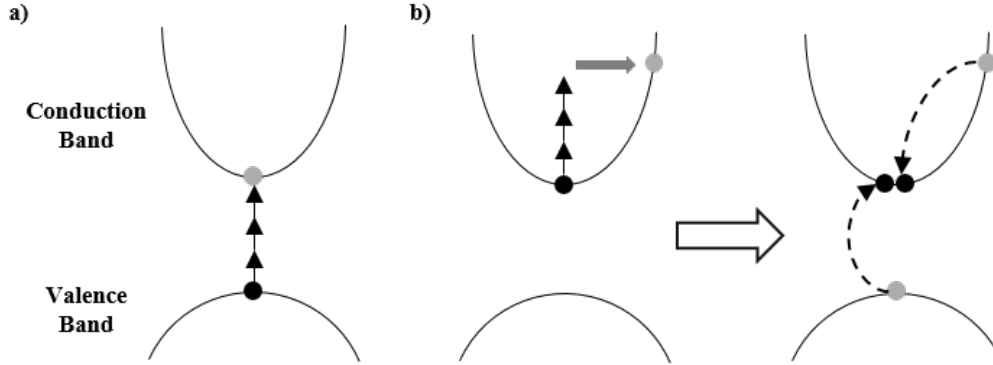


Figure 2.1: Non-linear photoionization processes: a) Multiphoton ionization; b) Avalanche ionization comprised of free carrier absorption, superseded by impact ionization.

For avalanche photoionization to take place, sufficient conduction band seed electrons are required. Seed electrons can be generated via multiphoton absorption. When a material is irradiated with an electromagnetic field, the seed electrons oscillate, increasing their energy within the conduction band. If this additional energy is greater than the band gap energy, the excited electron can ionise an additional electron from the valence band. The excited electron transfers the required energy to a bound electron via collisions. Energy transfer and ionisation through collisions is known as impact ionisation. The process results in two electrons with the minimum conduction band energy (Fig.2.1). If the laser pulse is still irradiating the focal volume, the process can repeat itself causing further ionisation. The density of electrons $\eta_a(t)$, can be calculated as a function of time t , using:

$$\eta_a(t) = \eta_0(t)2^{\omega_i t} \quad (2.3)$$

where, η_0 is the seed electron concentration and ω_i is the probability of impact ionisation. As equation 2.3 shows, avalanche ionisation is dependent on the number of seed electrons present, which is intrinsically determined by the material properties. If impurities are present, electrons could be excited via thermal excitation or linear absorption from low lying energy levels [9]. It has been reported that for short pulses ($< 100\text{fs}$) multiphoton absorption is the dominant ionization process, whereas for longer pulses, avalanche ionisation is the predominant process. For very short pulses ($< 10 \text{fs}$), it has been reported that in fused silica, photoionization can dominate over avalanche ionisation and generate a plasma density that can damage the material [11].

2.2.2 Energy deposition

Once the electrons have been excited into the conduction by one of the aforementioned processes, energy is evenly distributed via carrier-carrier scattering (10-100 fs) and

carrier-phonon scattering (> 10 ps) [10]. The former process ensures an even distribution of energy amongst the electrons whilst the latter equates the electron and lattice temperatures. Once energy has been transferred to the lattice, a modification ensues. The traits of the resultant modification depends on the irradiation parameters, such as pulse energy, pulse duration, polarization and repetition rate, as well as the intrinsic properties of the material.

If the created electron plasma density has a sufficient amount of energy, the transfer via defect formation and the electron-phonon interaction can cause damage. If the machining pulse irradiates a region for a time on the order of 10 ps, the resultant phonon can transfer energy to the surrounding material through thermal diffusion. If the temperature of the material is raised above the melting point a strong tension gradient forms. The tension leads to a poor quality modification due to the creation of fractures. The threshold fluence for damage has been reported to scale with the square root of the pulse duration, dictated by the rate of energy deposition and subsequent thermal diffusion [12]. However, the law capitulates for pulses shorter than 10 ps.

For sub-picosecond pulse durations, localized energy deposition takes place. As the lattice heating time is on the order of 10 ps, any pulse shorter than this duration has finished irradiating the focal volume when heat begins to be transferred to the lattice [9]. Hence, the electrons in the focal volume can reach extremely high temperatures whilst the surrounding material remains unaffected. Once the machining pulse has finished, the energy transfer remains strictly within the focal volume, reducing the heat affected zone in comparison to longer pulses (> 10 ps). Attempts have been made to express the damage threshold in terms of plasma density, although permanent damage has been reported at sub-critical plasma concentrations [13, 14].

2.2.3 Modification

The size of the modifications induced are on the scale of micrometers due to the high intensities required. Hence, the parameters of the focussing optics are a major contributing factor to the resultant machined structure. These can be classified into three categories based upon the numerical aperture (NA) of the lens used.

In the low NA regime ($NA < 0.1$), the focussing power is not strong enough to produce a permanent modification with a single pulse [15?]. Within a bulk, the femtosecond beam turns into a filament. The low focussing power has led to the adoption of low NA lenses for the surface modification as self focussing is not a factor of major influence.

For NAs from 0.1 to 0.5, a permanent modification within the bulk of fused silica can be machined. Spherical aberration plays a significant role in the beam propagation. At the air-silica interface, due to the difference in refractive index ($n_{silica} = 1.45$, at 1030 nm), the light is refracted. The degree of refraction is greater at the edge of the beam compared to the central part. Consequently, the adjacent element of the beam is focussed further into the substrate in comparison to the centre. In turn, reduction of the the angular spectrum of the beam occurs, increasing the beam size. The magnitude of the spherical aberration effect increases with NA. To mitigate against this, specialist spherical aberration correction optics, immersion optics, or adaptive optics can be introduced [16, 17].

Finally, oil immersion lenses with large NAs ($NA > 0.9$) can be used to achieve tight

focussing, as well as to compensate for refractive index differences. The tight focussing generates a small, intense focal volume allowing material modifications at nanojoule energies [18, 19].

In fused silica, for pulse durations < 200 fs, it is possible to create three types of modification: a smooth refractive index change [6], nanogratings [20] and void formation [21].

Homogeneous refractive index change

Davis et al. reported the first observation of homogeneous refractive index change [22]. The group demonstrated the ability to write waveguides exhibiting a low loss of < 0.15 dB/cm. The tracks were written by a Ti:sapphire laser and induced a positive index change between 0.01-0.035. The positive change in refractive index can be explained by two models: defect formation and material densification.

Defect formation and refractive index change Explanations have been proposed for refractive index change via a Kramers-Kronig mechanism related to absorption [23]. The model suggests that increased absorption due to the generation of defects, subsequently causes an increase in refractive index. The process of femtosecond laser defect formation is complex in nature and is not clearly understood. Attempts have been made to explain the phenomenon through the relaxation of self-trapped excitons [24].

After an electron has been promoted to the conduction band, an exciton can form comprising of an electron and hole bound together via the Coulomb force. The recombination represents a neutrally charged electronic excitation [25]. Excitons can be generated in two ways: inelastic scattering of electrons or by resonant absorption of multiple photons [26]. Excitons are formed from electron-hole pairs on a very fast time-scale, often shorter than 1 ps in wide bandgap materials [27].

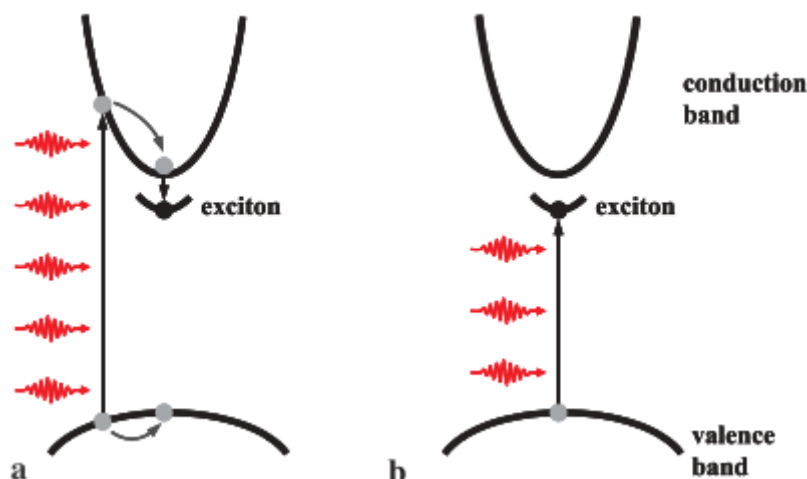


Figure 2.2: Schematic illustration of exciton level and two basic routes for exciton generation: a) Inelastic scattering of the multiphoton-excited electrons; b) Direct resonant absorption of multiple photons [28].

Excitons can relax in either a localized or delocalized manner. The relaxation process begins on the order of tens of picoseconds after excitation from the laser pulse. Exciton self trapping describes the energy conversion process from electronic excitation into changes in the atomic structure [29]. During self-trapping a carrier becomes restricted to a lattice site. Small atomic displacements can take place in the trapped region caused by short-range covalent molecular bonding or long-range electrostatic polarization deriving from displacement of ions. These small fluctuations in atomic positioning can deepen the Coulomb potential well that the carrier is trapped within. Thermal fluctuations are sufficient for triggering instantaneous deformation of the lattice for the exciton self trapping process to start.

In silica, local self trapping occurs in conjunction with strong distortion of the silica lattice. SiO_2 comprises of SiO_4 tetrahedra with silicon at the centre and a single oxygen atom at each of the four corners [13]. The Si-O-Si bonds are weakened and an oxygen atom becomes displaced from its equilibrium point within the tetrahedral. In turn, silicon and oxygen dangling bonds are formed [28]. The hole and electron of the self trapped exciton, remains on the oxygen and silicon dangling bonds, respectively.

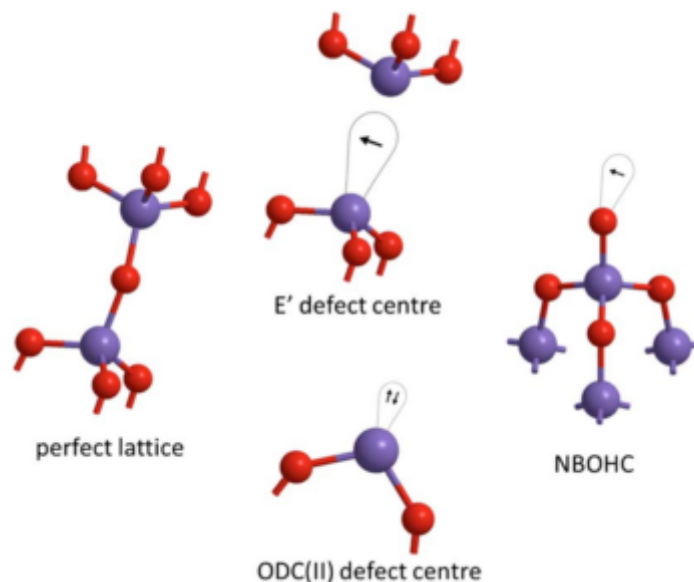


Figure 2.3: Structural models of perfect SiO_2 lattice and most-abundant laser-induced defects. Purple spheres, silicon; red, oxygen. Oxygen deficiency centres: E' , asymmetrically relaxed oxygen vacancy with an unpaired electron localized in a sp^3 -like orbital of a single silicon atom; $ODC(II)$, divalent Si atom. Oxygen excess centre: $NBOHC$, oxygen dangling bond [10].

Femtosecond laser inscription has been reported to cause a number of different defects (summarised in Fig.2.3) to the silica tetrahedra ($\equiv\text{Si-O-Si}\equiv$). Two forms of oxygen deficient centres can form [24]. The first, $ODC(I)$ is composed of four valent silicon-silicon bonds ($\equiv\text{Si-Si}\equiv$). The second, $ODC(II)$ is comprised of divalent silicon atoms ($=\text{Si}^0$) [24]. The E' defect is a similar oxygen related vacancy but differs from the $ODC(II)$ as the unpaired electron is confined to an sp^3 orbital [30]. The last type of defect involves an excess of oxygen [31] known as non-bridging oxygen hole centre ($NBOHC$, $\equiv\text{Si-O}\bullet$), which consists of an oxygen dangling bond [32].

These defects give rise to the refractive index change. Furthermore, they stimulate

further refractive index change on the multi-pulse regime by supplying absorption centres, encouraging further ionization. However, at 400 °C, defects can be annealed [33]. However, the refractive index change can still be observed up to 900 °C. Therefore, the refractive index change is only partially explained by defect formation.

Restructuring of glass matrix

In silica, the refractive index modulation caused by femtosecond laser radiation can also be partially attributed to the rearrangement of the silica network. This occurs due to the rapid temperature change that takes place when the focal volume is irradiated. Raman spectroscopy has been used to analyse the refractive index changes and has revealed increases in the three and four member rings in the silica structure, indicating densification of the glass [34]. Furthermore, the femtosecond interaction causes an increase in fictive temperature in the focal volume. For amorphous glass, the fictive temperature is representative of the matrix order and reflects the thermal history of the material [35]. The relationship is inversely correlated: higher fictive temperatures are representative of lower order. Typically, for the majority of glasses, a slower cooling rate causes a matrix order of higher density. Silica is an anomalous glass and exhibits the highest density at a fictive temperature of 1500 °C [36]. Furthermore, glass restructuring is also caused by shock waves [37]. Expanding material in the focal volume can cause strain in the vicinity and subsequently, cause a refractive index increase.

Birefringent refractive index change

With higher fluences, a birefringent refractive index change can be induced. It has been reported that the birefringence is caused by interference between the electromagnetic field of the laser and the electron plasma wave [20]. The interference causes structures known as nanogratings to form. These are orientated orthogonal to the polarization direction of the writing beam. The period of the nano-scale structures was $\sim \frac{\lambda}{2n}$ irrespective of writing speed, implying that nanogratings are formed by a self replicating process [38].

Void formation

At very high fluences giving peak intensities $> \sim 10^{14} \text{ Wcm}^{-2}$, pressures larger than the Young's modulus are created within the focal volume. Subsequently, after the energy has been deposited in the lattice, a shockwave can be created. Depending on the writing beam intensity and the material, this results in either a less dense area or a hollow core, otherwise known as a void. By conservation of mass, the lower refractive index region is surrounded by an area of higher density [39].

2.3 Conclusion

In summary, the chapter detailed the fundamental physical phenomenon of the interaction between a femtosecond laser pulse and bulk transparent glass. The high intensity of the laser pulse generates a free electron plasma through the processes of multiphoton

absorption and avalanche ionisation. Explained through the formation of self-trapping excitons, energy is transferred to the lattice. After exposure to the electromagnetic radiation has finished, a refractive index change remains. The change in refractive index can be explained by a change in the defect population and restructuring of the glass matrix, described as an increase in the fictive temperature of the glass. The characteristics of the resultant modification are dependent on the irradiation parameters. At lower fluences either a smooth or birefringent refractive index change is induced. At high fluences, void formation occurs.

Bibliography

- [1] Sibbett, W.; Lagatsky, A. A.; Brown, C. T. A. The development and application of femtosecond laser systems. *Optics Express* **2012**, *20*, 6989.
- [2] Fermann, M. E.; Hartl, I. Ultrafast fibre lasers. *Nature Photonics* **2013**, *7*, 868–874.
- [3] Graf, R.; Fernandez, A.; Dubov, M.; Brueckner, H. J.; Chichkov, B. N.; Apolonski, A. Pearl-chain waveguides written at megahertz repetition rate. *Applied Physics B* **2007**, *87*, 21–27.
- [4] Eaton, S.; Zhang, H.; Herman, P.; Yoshino, F.; Shah, L.; Bovatsek, J.; Arai, A. Heat accumulation effects in femtosecond laser-written waveguides with variable repetition rate. *Optics Express* **2005**, *13*, 4708–4716.
- [5] Kerse, C.; Kalaycıođ Lu, H.; Elahi, P.; Çetin, B.; Kesim, D. K.; Akçaalan, Ö.; Yavaş, S.; Aşık, M. D.; Öktem, B.; Hoogland, H.; Holzwarth, R.; Ilday, F. Ö. Ablation-cooled material removal with ultrafast bursts of pulses. *Nature* **2016**, *537*, 84–88.
- [6] Davis, K. M.; Miura, K.; Sugimoto, N.; Hirao, K. Writing waveguides in glass with a femtosecond laser. *Optics Letters* **1996**, *21*, 1729–1731.
- [7] Stuart, B. C.; Feit, M. D.; Herman, S.; Rubenchik, A. M.; Shore, B. W.; Perry, M. D. Nanosecond-to-femtosecond laser-induced breakdown in dielectrics. *Physical Review B* **1996**, *53*, 1749–1761.
- [8] Keldysh, L. V. Ionization in the field of a strong electromagnetic wave. *Soviet Physics JETP* **1965**, *20*, 1307–1314.
- [9] Schaffer, C. B.; Brodeur, A.; Mazur, E. Laser-induced breakdown and damage in bulk transparent materials induced by tightly focused femtosecond laser pulses. *Measurement Science and Technology* **2001**, *12*, 1784–1794.
- [10] Beresna, M.; Gecevicius, M.; Kazansky, P. G. Ultrafast laser direct writing and nanostructuring in transparent materials. *Advances in Optics and Photonics* **2014**, *6*, 293–339.
- [11] Lenzner, M.; Krüger, J.; Sartania, S.; Cheng, Z.; Spielmann, C.; Mourou, G.; Kautek, F. Femtosecond optical breakdown in dielectrics. *Physical Review Letters* **1998**, *80*, 4076–4079.
- [12] Perry, M. D.; Stuart, B. C.; Banks, P. S.; Feit, M. D.; Yanovsky, V.; Rubenchik, A. M.; Perry, M. D.; Stuart, B. C.; Banks, P. S.; Feit, M. D.; Yanovsky, V.; Rubenchik, A. M. Ultrashort-pulse laser machining of dielectric materials. **2012**, *6803*.
- [13] Papazoglou, D. G.; Zergioti, I.; Tzortzakis, S. Plasma strings from ultraviolet laser filaments drive permanent structural modifications in fused silica. *Optics Letters* **2007**, *32*, 2055–2057.
- [14] Sudrie, L.; Couairon, A.; Franco, M.; Lamouroux, B.; Prade, B.; Tzortzakis, S.; Mysyrowicz, A. Femtosecond laser-induced damage and filamentary propagation in fused silica. *Physical Review Letters* **2002**, *89*, 186601.

-
- [15] von der Linde, D.; Schüler, H. Breakdown threshold and plasma formation in femtosecond laser–solid interaction. *Journal of the Optical Society of America B* **1996**, *13*, 216.
- [16] Marcinkevičius, A.; Mizeikis, V.; Juodkazis, S.; Matsuo, S.; Misawa, H. Effect of refractive index-mismatch on laser microfabrication in silica glass. *Applied Physics A: Materials Science and Processing* **2003**, *76*, 257–260.
- [17] Simmonds, R. D.; Salter, P. S.; Jesacher, A.; Booth, M. J. Three dimensional laser microfabrication in diamond using a dual adaptive optics system. *Optics Express* **2011**, *19*, 24122.
- [18] Streltsov, A. M.; Borrelli, N. F. Fabrication and analysis of a directional coupler written in glass by nanojoule femtosecond laser pulses. *Optics Letters* **2001**, *26*, 42.
- [19] Schaffer, C. B.; Brodeur, A.; García, J. F.; Mazur, E. Micromachining bulk glass by use of femtosecond laser pulses with nanojoule energy. *Optics Letters* **2001**, *26*, 93.
- [20] Shimotsuma, Y.; Kazansky, P. G.; Qiu, J.; Hirao, K. Self-organized nanogratings in glass irradiated by ultrashort light pulses. *Physical Review Letters* **2003**, *91*, 247405.
- [21] Glezer, E. N.; Milosavljevic, M.; Huang, L.; Finlay, R. J.; Her, T.; Callan, J. P.; Mazur, E. Three-dimensional optical storage inside transparent materials. *Optics Letters* **1996**, *21*, 2023.
- [22] Davis, C. *Fiberoptic Sensor Technology Handbook* by. **1982**, 5225.
- [23] Hirao, K.; Miura, K. Writing waveguides and gratings in silica and related materials by a femtosecond laser. *Journal of Non-Crystalline Solids* **1998**, *239*, 91–95.
- [24] Sun, H.-B.; Juodkazis, S.; Watanabe, M.; Matsuo, S.; Misawa, H.; Nishii, J. Generation and recombination of defects in vitreous silica induced by irradiation with a near-infrared femtosecond laser. *The Journal of Physical Chemistry B* **2000**, *104*, 3450–3455.
- [25] Ueta, M.; Kanzaki, H.; Kobayashi, K.; Toyozawa, Y.; Hanamura, E. *Excitonic Processes in Solids*; Springer Berlin Heidelberg: Berlin, Heidelberg, 1986; pp 309–369.
- [26] Vasilev, A. N.; Fang, Y.; Mikhailin, V. V. Impact production of secondary electronic excitations in insulators: multiple-parabolic-branch band model. *Physical Review B - Condensed Matter and Materials Physics* **1999**, *60*, 5340–5347.
- [27] Haglund Jr, R. F.; Itoh, N. *Laser Ablation, Principles and Applications*, ed. JC Miller. 1994.
- [28] Mao, S. S.; Quéré, F.; Guizard, S.; Mao, X.; Russo, R. E.; Petite, G.; Martin, P. Dynamics of femtosecond laser interactions with dielectrics. *Applied Physics A: Materials Science and Processing* **2004**, *79*, 1695–1709.
- [29] Toyozawa, Y. In *Relaxation of Elementary Excitations*; Kubo, R., Hanamura, E., Eds.; Springer Berlin Heidelberg: Berlin, Heidelberg, 1980; pp 3–18.
- [30] Skuja, L. Optically active oxygen-deficiency-related centers in amorphous silicon dioxide. *Journal of Non-Crystalline Solids* **1998**, *239*, 16–48.

-
- [31] Zoubir, A.; Rivero, C.; Grodsky, R.; Richardson, K.; Richardson, M.; Cardinal, T.; Couzi, M. Laser-induced defects in fused silica by femtosecond IR irradiation. *Physical Review B - Condensed Matter and Materials Physics* **2006**, *73*, 1–5.
- [32] Skuja, L.; Kajihara, K.; Hirano, M.; Hosono, H. Oxygen-excess-related point defects in glassy/amorphous SiO₂ and related materials. *Nuclear Instruments and Methods in Physics Research, Section B: Beam Interactions with Materials and Atoms* **2012**, *286*, 159–168.
- [33] Streltsov, A. M.; Borrelli, N. F. Study of femtosecond-laser-written waveguides in glasses. *Journal of the Optical Society of America B* **2002**, *19*, 2496.
- [34] Chan, J. W.; Huser, T.; Risbud, S.; Krol, D. M. Structural changes in fused silica after exposure to focused femtosecond laser pulses. *Optics Letters* **2001**, *26*, 1726.
- [35] Bressel, L.; de Ligny, D.; Sonnevile, C.; Martinez-Andrieux, V.; Mizeikis, V.; Buividas, R.; Juodkazis, S. Femtosecond laser induced density changes in GeO₂ and SiO₂ glasses: fictive temperature effect. *Opt. Mater. Express* **2011**, *1*, 1150–1158.
- [36] Brückner, R. Properties and structure of vitreous silica. I. *Journal of Non-Crystalline Solids* **1970**, *5*, 123–175.
- [37] Vailionis, A.; Gamaly, E. G.; Mizeikis, V.; Yang, W.; Rode, A. V.; Juodkazis, S. Evidence of superdense aluminium synthesized by ultrafast microexplosion. *Nature Communications* **2011**, *2*, 445–446.
- [38] Birks, T. A.; Mangan, B. J.; Díez, A.; Cruz, J. L.; Murphy, D. F. Photonic lantern - spectral filters in multi-core fibre. **2012**, *20*, 13996–14008.
- [39] Juodkazis, S.; Nishimura, K.; Tanaka, S.; Misawa, H.; Gamaly, E. G.; Luther-Davies, B.; Hallo, L.; Nicolai, P.; Tikhonchuk, V. T. Laser-induced microexplosion confined in the bulk of a sapphire crystal: Evidence of multimegabar pressures. *Physical Review Letters* **2006**, *96*, 1–4.

Chapter 3

Point-by-point Fibre Bragg Gratings

3.1 Introduction

The discovery of fibre Bragg gratings (FBGs) in 1978 has had a profound effect on photonics [1]. Developments over the following decades aided the establishment of FBGs as fundamental optical components. Their significance is best illustrated by their utilisation as reflectors or band rejection filters in a vast array of applications such as telecommunications, sensing and fibre laser engineering [2]. For decades, UV based inscription techniques have been developed and exploited on a commercial scale to produce a variety of grating types. The discovery of ultrafast laser micro-machining has opened a new alternative to these methodologies.

The following chapter covers the experimental work fabricating Bragg gratings in two novel fibres: a multicore fibre; and high concentration germanium fibre. Working with these two fibres pose issues for classical UV based techniques due to the fundamental principles they rely on. Using ultrafast micro-machining, these issues are not encountered. The first section cover the fundamental theory behind uniform Bragg gratings. After, a literature review of fabrication techniques is presented. The final sections detail the experimental methodology, results and conclusions of the fabrication of Bragg gratings in these two unique fibres.

3.2 Fibre Bragg Gratings: Fundamental Principles

Fibre Bragg gratings comprise of periodic perturbations in refractive index along a waveguide longitudinal axis (Fig.3.1). By coupling counter-propagating core modes resonant with the structure, light of Bragg wavelength λ_B is reflected. Since the reflected light travels within the core, Bragg gratings can be utilised as reflectors or band rejection filters. Light that is confined by the waveguide will encounter each grating plane as it travels through the core. If the grating pitch does not equal a half integer of the wavelength of light in the medium, wave fronts reflected from each plane will

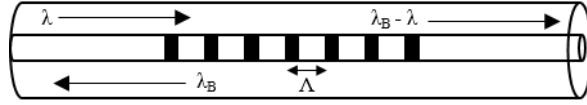


Figure 3.1: Schematic showing the structure of a uniform Bragg Grating in a waveguide of effective modal index n_{eff} . The black regions indicate areas of larger refractive index separated by period Λ . The periodicity causes the reflection of light corresponding to the Bragg wavelength $\lambda_B = \frac{2n_{eff}\Lambda}{m}$, where m is the order number.

become increasingly out of phase and eventually will negate one another via destructive interference. Thus, for reflection to occur, the Bragg condition must be met:

$$\lambda_B = \frac{2n_{eff}\Lambda}{m} \quad (3.1)$$

where λ_B is the Bragg wavelength, n_{eff} is the effective modal index, Λ is the grating period and m is the mode number. The strongest reflection occurs for the first order mode, $m = 1$. When radiation of wavelength λ_B is incident on the structure, reflections from each plane are in phase with one another and thus, combine constructively to form a back-reflected mode.

Given the variety of possible Bragg structures, a number of modelling approaches have been developed to numerically describe the optical characteristics of a FBG [3, 4, 5]. Most commonly, coupled-mode theory forms the basis for several techniques due to its relative simplicity and accuracy when predicting the optical characteristics of a grating [6].

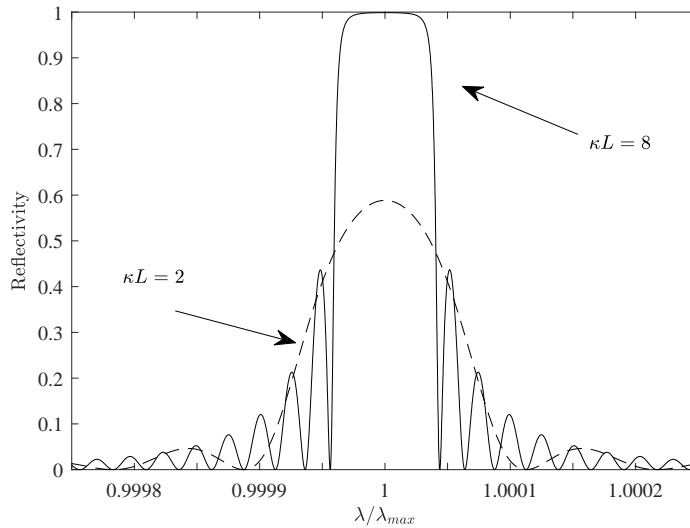


Figure 3.2: Reflection spectra of an ideal uniform grating with $\kappa L = 8$ (solid) and $\kappa L = 2$ (dotted). Wavelengths have been normalised to λ_{max} , the wavelength of maximum reflection.

Fundamentally, the theory is based upon the superposition of counter-propagating modes through an optical waveguide. In an ideal waveguide these counter-propagating modes do not exchange energy as they are orthogonal. However, when a dielectric perturbation is introduced, these modes couple together. It is assumed that FBGs

formed by ultraviolet (UV) radiation comprise of a perturbation in the effective refractive index, n_{eff} . This dielectric fluctuation is experienced by the guided mode along the length of fibre, z . The effective index profile of the perturbation can be described mathematically by:

$$\delta n_{eff} = \overline{\delta n_{eff}}(z) \left(1 + \nu \cos \left[\frac{2\pi}{\Lambda} z + \phi(z) \right] \right) \quad (3.2)$$

where $\overline{\delta n_{eff}}$ is the “dc” index change averaged over a grating period, ν is the fringe visibility of the index change, Λ is the grating period and $\phi(z)$ describes the grating chirp, ($= 0$ for a uniform grating). Thus, considering light of wavelength λ_B interacting with a uniform grating, further analysis leads to a single Ricatti differential equation describing the local reflectivity. This can be solved using numerical integration techniques to give the power reflection coefficient:

$$r = \frac{\sinh^2(\sqrt{\kappa^2 - \hat{\sigma}^2} L)}{\cosh^2(\sqrt{\kappa^2 - \hat{\sigma}^2} L) - \frac{\hat{\sigma}^2}{\kappa^2}} \quad (3.3)$$

where κ is the “AC” coupling coefficient, $\hat{\sigma}$ is the “dc” coupling coefficient and L is the length of the fibre grating. For a uniform, single mode grating κ and $\hat{\sigma}$ are found to be:

$$\kappa = \frac{\pi}{\lambda} \nu \overline{\delta n_{eff}} \quad (3.4)$$

$$\hat{\sigma} = \frac{2\pi}{\lambda} \overline{\delta n_{eff}} \quad (3.5)$$

For more complex structures the “dc” coupling coefficient can describe grating chirping and any any detuning effects [6]. By simplifying equation 3.3 the maximum reflectivity of the grating can be calculated using:

$$r_{max} = \tanh^2(\kappa L) \quad (3.6)$$

Equation 3.6 implies the reflectivity of a FBG depends on two parameters: grating length and size of refractive index modulation. Using this equation, the ideal reflection spectrum can be plotted (Fig.3.2). The spectra take the form of a sinc function, originating from the finite extent when a harmonic signal is Fourier transformed. If the grating was infinitely long, the reflection spectrum would take the form of a delta function. Thus, as the length of a grating increases, the bandwidth of the reflection peak decreases.

As well as reflecting into a backward propagating mode, FBGs also possess the ability to couple light into the cladding. This can be useful for applications or where light needs to be pushed out of the core such as sensing [7]. In FBGs, the spectral appearance of the cladding modes depends on the refractive index relationship between the fibre cladding and the surrounding environment (Fig. 3.3). The figure shows the transmission profile of the LP₀₁ mode through a 5 mm Gaussian fibre grating of an index change $\overline{\delta n_{eff}} = 2 \times 10^{-3}$.

In Fig. 3.3a, the fibre section containing the FBG was immersed in an index matching oil such that the refractive index of the cladding, n_{cl} was equal to the refractive index of the surrounding environment, n_s . Thus, this has the impact of simulating an infinite cladding. The result is a smooth transmission profile for wavelength < 1540 nm. This is due to a loss of light coupled from the fundamental mode to radiation modes. In Fig. 3.3b, the bare fibre has been immersed in glycerine, such that $n_{cl} < n_s$. In a case where

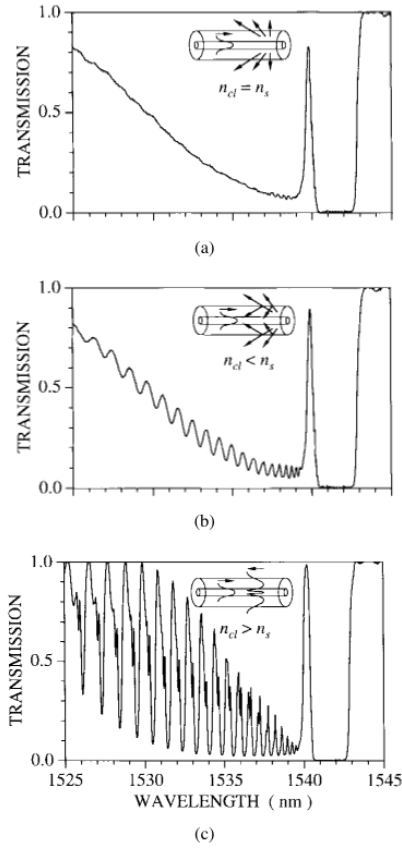


Figure 3.3: The measured transmission spectra of a Gaussian Bragg grating, 5 mm long of a "dc" index change $\overline{\delta n_{eff}} = 2 \times 10^{-3}$, where the uncoated fibre is a) immersed in index matching oil simulating an infinite cladding; b) immersed in glycerine; and c) surrounded by air, thus supporting the propagation of cladding modes. The inset of each figure shows the relation of the surrounding environmental index n_s to the cladding index n_{cl} , as well as a ray diagram of the radiation and cladding modes induced [6].

the surrounding environment index is greater than the cladding index, the transmission spectrum exhibits fringes similar to Fabry Perot interference. This is caused by the partial reflection of the radiation modes from the cladding-glycerine boundary. In the final plot, Fig. 3.3c, the bare fibre is surrounded by air only. For wavelengths < 1540 nm, the LP_{01} mode is coupled into backward propagating cladding modes. The spectra shows a clearly defined resonance peak for each individual mode. Cladding modes are bound by the condition $1 \leq n_{eff} \leq n_{cl}$ assuming the fibre is surrounded by air. It can be shown that the grating period required for counter-propagating coupling between a core mode of index n_{eff}^{co} and a cladding mode of index n_{eff}^{cl} is $\Lambda = \lambda / (n_{eff}^{co} + n_{eff}^{cl})$ [6]. Further analysis has been completed around cladding and radiation mode coupling, but their analysis is beyond the scope of this work [8, 9, 10].

3.3 Bragg Grating Fabrication Techniques

The first observation of gratings in photosensitive media dictated three decades of UV based fabrication techniques [11]. Today, most commonly interferometric and phase mask techniques are used to inscribe gratings. However, as UV writing relies on exploiting the photosensitive properties of a fibre, there is a limitation on the possible materials eligible for inscription.

Femtosecond writing offers an alternative to UV based techniques for FBG fabrication. Via multiphoton absorption and avalanche ionisation, femtosecond writing can alter the properties of bulk transparent glass. As such, femtosecond writing has bypassed the restrictions of UV-based techniques and expanded FBG fabrication to materials considered non-photosensitive to nanosecond lasers. Furthermore, the dependency of the process on laser intensity allows infra-red (IR) wavelengths to be employed. This offers an additional advantage due to the transparency to the fibre coating [12] at these wavelengths. Typically, most commonly used fibre coatings are not transparent to UV radiation and their removal is necessary prior to FBG fabrication.

3.3.1 Point-by-point femtosecond gratings

Apart from phase mask and interferometric techniques, the other main fabrication method for FBGs is the PbP methodology. Malo et al. first demonstrated the point-by-point technique in 1993 using an excimer laser to inscribe Bragg gratings in D-shaped fibres [13]. Its name derives from the systematic methodology Malo used: each refractive index modification was inscribed individually, “point-by-point” (PbP). The experimental set up was relatively simple - the excimer laser beam was focussed through a 0.25 NA objective lens to produce a small enough focal volume, the fibre was secured by two clamps and then translated beneath the objective using computer controlled stages. In comparison to the phase mask and interferometric methodologies, the PbP technique had the added benefit of controlling the period of the gratings by altering the translation position of the fibre. Thus, complex grating structures could be produced with relative ease [14].

The first demonstration of the PbP technique using a femtosecond laser was by Martinez et al. in 2004 [15]. Using a Ti:sapphire laser, first, second and third order gratings were inscribed in commercial single mode telecommunication fibres. Higher order gratings are characterised by the period spacing of index perturbations (Eq. 3.1); second and third orders translate to a period spacing twice and three times that of a first order grating. The work showed the power of using a femtosecond laser over of a UV laser as a non-photosensitised fibres were used. Furthermore, the PbP technique did not require the fabrication of an intricate phase mask, nor the precise alignment required for interferometric techniques. Combined with the ability to inscribe through the coating of the fibre, the FBG fabrication process had been gravely simplified compared to UV-based interferometric techniques; only a femtosecond laser focussed through a microscope objective were used.

However, their work also highlighted the limitation of the technique when producing lower order gratings due to poor phase coherence between the grating planes. The sharply defined nature of induced modifications are a stark contrast to the smooth sinusoidal refractive index profiles produced by UV-photosensitive techniques [16]. Fur-

thermore, the larger spot size in the fibre core of the femtosecond laser during inscription, compared to a UV beam, leads to overlapping of grating planes at lower orders. At 1550 nm, a first order grating should have a period of ~ 500 nm. For a $1 \mu\text{m}$ femtosecond laser, this occurs under below the diffraction limit of the beam. Although, sub-diffraction limit structures have been demonstrated using femtosecond micro-machining, working in this regime is extremely difficult to control as the writing parameters are at the threshold of the highly non-linear fundamental processes at work. Thus, higher order gratings are preferred when using the PbP technique as less precision is required and their extinction at the Bragg wavelength is more prominent. The work of Martinez et al. demonstrated that high spectral quality FBGs could be produced; all had a low insertion loss of < 2 dB, 0.1 - 0.2 nm bandwidth and a strong extinction of ~ 25 dB at the resonant Bragg wavelength. PbP gratings do have limitations in its spectral quality outside of the resonant Bragg wavelength. The highly localized nature of the index perturbation, causes strong coupling to cladding modes [17]. The transverse planar nature of relatively high index change, leads to different coupling behaviour compared to homogenous gratings formed with interferometric fabrication techniques. Homogenous gratings lead to coupling to and from azimuthally independent fibre modes [9]. On the other hand, PbP gratings allow efficient access to higher order fibre modes [18]. The effects of cladding mode coupling increase with grating length. Therefore, this effect can be minimised by writing as short a grating as possible.

3.3.2 Multicore fibre Bragg gratings

Multicore fibre Bragg gratings (MC-FBGs) are of great interest due to their potential application in space division multiplexing (SDM) systems [19]. SDM looks to improve the data capacity of a fibre by increasing the number of fibre cores, propagation modes or a combination of both. Each additional core and / or mode is utilised as an independent information channel. MC-FBGs are a key conceptual component in SDM systems for dispersion compensation or filtering purposes.

Recently, successful fabrication of MC-FBGs has been reported [20, 21]. In both cases, successful inscription was achieved using a UV source to simultaneously illuminate all cores using a single phase mask. The technique successfully fabricated reasonable spectral quality gratings. However, the non-uniform absorption of UV radiation leads to effective Bragg grating period discrepancies. The effect can be mitigated against using various scanning techniques, but is difficult to eliminate entirely. Furthermore, the simultaneous inscription of all cores with a single phase mask means all gratings have the same pitch. In SDM, as all cores are independent of one another, fabricating FBGs of varying pitch would be a more pragmatic solution.

Femtosecond laser assisted inscription is a viable option for producing core-specific MC-FBGs. To permit isolated FBG fabrication the point-by-point (PbP) technique was employed. This fabrication methodology is based upon focussing the writing beam through a high numerical aperture lens, allowing the targeting of each core individually. The technique also provides extra flexibility in producing complex grating structures such as chirp or amplitude modulation without significantly modifying the inscription set-up [14]. In the experiment conducted, the PbP technique was used with a femtosecond laser, to fabricate four FBGs into a 7-core MCF. Computational simulations were completed to generate lines of best fit to determine the characteristics of the inscribed FBGs.

3.3.3 High concentration germanium fibre Bragg gratings

High concentration ($> 40\%$) germania-doped fibres have two attractive traits: low attenuation in the mid - IR and their highly non-linear behaviour originating from their large Raman scattering cross section. In comparison to other glass forming oxides, germania has one of the highest peak value of Raman scattering cross section - at a glass frequency shift of 420 cm^{-1} its cross section is 9.2 times that of silica [22]. The large cross section means germania-doped optical fibres have the potential to be extremely efficient Raman fibre lasers and amplifiers, tunable across a wide spectral region. As well as its large Raman scattering cross section, the non-linear refractive index coefficient n_2 of germania is 3-fold that of silica, which has been reported to be beneficial for four wave mixing [23]. Davey et. al observed that at a glass frequency shift of 440 cm^{-1} , the Raman gain coefficient increased linearly with the concentration of germania within the fibre core [24]. The Raman gain coefficient doubled when the normalised refractive index difference of the core and cladding Δn , was increased from 0.005 to 0.04 .

In spite of these properties, the full potential of germania-doped waveguides has not been reached. Their application has been stifled by the difficulty in inscribing FBGs using UV-based techniques. This is caused by the complex dynamics underpinning the UV-fabrication process [25]. At low dosage levels of UV ($< \text{GWcm}^{-2}$), the phenomenon of photosensitivity can be explained by a change in the defect population and material densification [26, 27]. The linear absorption of UV radiation is directly proportional to the concentration of germania in the fibre core. As radiation is absorbed the material's absorption spectrum changes; some absorption bands increase whilst others are bleached. The changes in the absorption spectrum and the balance of the underlying physical processes differ depending on the chemical composition of the material and the irradiation characteristics. Furthermore, the 242 nm absorption coefficient of a germania-doped silica fibre α_{242} , scales with the concentration of germania by 36 dB/mm per mole % [28]. Therefore, $\alpha_{242} = 1.44 \text{ dB } \mu\text{m}^{-1}$ for a 40%mol [12]. The high absorption makes FBG fabrication in these fibres difficult. Asymmetric grating planes with poor phase coherence are likely to form leading to cladding mode generation. Thus, a low spectral quality reflector is produced.

Femtosecond laser assisted machining offers a solution to this problem. The refractive index change induced relies on different fundamental physical phenomena. Multiphoton absorption breaks Si-O bonds and avalanche ionisation causes the melting and re-solidifying of glass [29, 30]. Thus, the photosensitive phenomena does not effect the inscription process. In the experiments conducted, a FBG was fabricated in a 40%mol germania-doped optical fibre using a femtosecond laser. The point-by-point technique was used whereby grating planes are written individually by focussing the writing beam through a high numerical aperture lens. After fabrication, the FBG was annealed at $500 \text{ }^\circ\text{C}$ and thermally tested up to $750 \text{ }^\circ\text{C}$.

3.4 Experimental Methodology

3.4.1 Optical Fibre Specification

Multicore Fibre

A 7-core MCF was used in the experiments. The MCF was fabricated within the ORC using the stack-and-draw technique. The seven single mode fibre (SMF) cores are arranged in a hexagonal array (Fig. 3.4). A continuous air hole was introduced for orientation purposes. Each core is $10 \pm 0.2 \mu\text{m}$ diameter and the fibre has a $198 \pm 0.2 \mu\text{m}$ cladding diameter. The numerical aperture of each SMF core is 0.12 and the average core pitch is $50 \mu\text{m}$. Each core was connected to an SMF telecommunication fibre (SMF 28, Corning) via a fan-in-fan-out device.

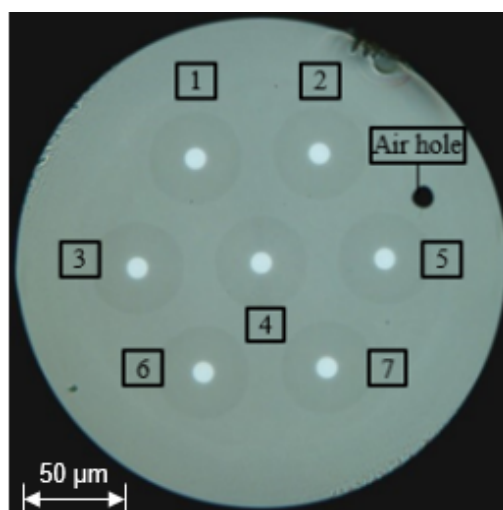


Figure 3.4: Annotated microscope image of the 7 core MCF cross section used for the fabrication of FBGs.

High Concentration Germania-doped Fibre

The fibre was produced in-house at the ORC. The preform was fabricated using the modified chemical vapour deposition (MCVD). DSM-314 cured by photo-polymerisation was used to coat the fibre. The DSM-314 coating was favourable over other alternatives due to its high refractive index which inhibits cladding mode propagation. The refractive index profile of the fibre was recorded using a multi-wavelength optical fibre analyser (IFA-100, ASM Technologies.) The refractive index profile was plotted to further understand its structure (Fig. 3.5.) The core and cladding diameters were recorded to be $3.72 \pm 0.2 \mu\text{m}$ and $106 \pm 0.2 \mu\text{m}$, respectively. The measurement had an accuracy of $\pm 1.0 \times 10^{-4}$.

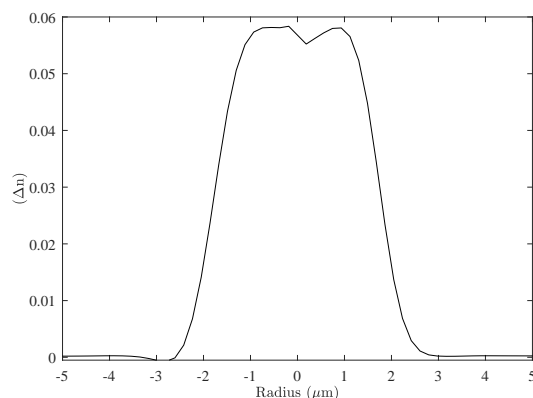


Figure 3.5: The refractive index profile of the high concentration germania doped optical fibre.

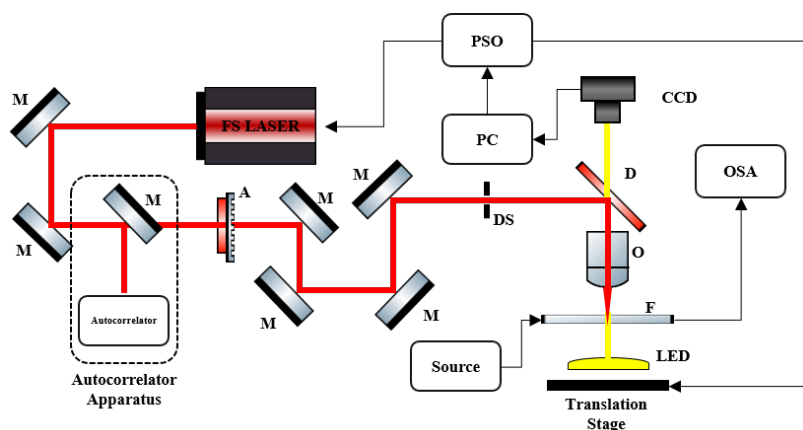


Figure 3.6: Schematic diagram of the femtosecond writing arrangement. *M* - mirror, *A* - attenuator, *DS* - diffraction slit, *D* - dichroic mirror, *O* - objective lens, *F* - fibre, *SC* - Supercontinuum, *OSA* - Optical Spectrum Analyser, *PSO* - position synchronised output controller.

3.4.2 Bragg Grating Fabrication

A femtosecond laser writing set up was assembled to fabricate the FBGs (Fig.3.6). A 1030 nm solid state Yb:KGW (ytterbium-doped potassium gadolinium tungstate) laser system (Pharos, Light Conversion Ltd) was used for inscription. At this wavelength the polymer coating is transparent meaning its removal is not necessary prior to inscription. Using an autocorrelator (Geco, Light Conversion), the temporal pulse duration was measured to be 206 ± 5 fs, assuming a Gaussian pulse shape. The laser frequency was set to 1 kHz for the fabrication of both FBGs. The pulse energy was measured to be $2.1 \pm 0.2 \mu\text{J}$ and $1.1 \pm 0.2 \mu\text{J}$ for the MCF and the germanium-doped fibre, respectively. Immediately after the pulse was emitted from the laser cavity, the beam was guided by mirrors through an attenuator to control the pulse energy. After, the beam propagated through a diffraction slit orientated parallel to the fibre propagation axis. The diffraction slit was inserted to control the symmetry of the modification cross section induced within the fibre.

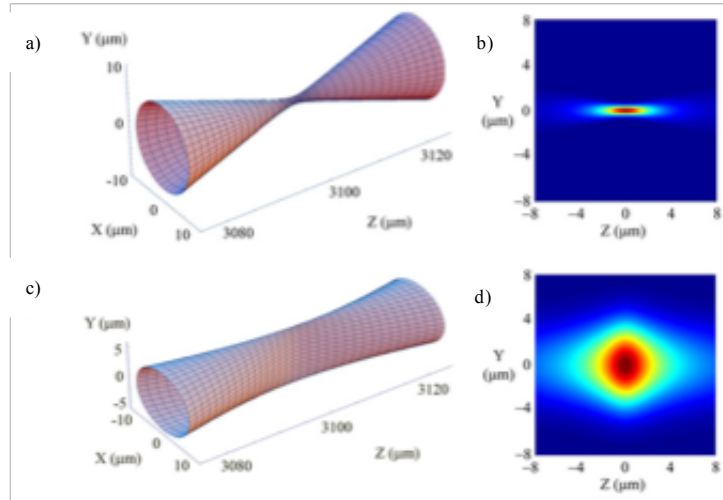


Figure 3.7: a) beam evolution near focus not using slit; b) energy distribution in YZ plane not using slit; c) beam evolution near focus using slit; d) energy distribution in YZ plane using slit where x corresponds with the direction of the beam translation and the waveguide axis [31]

During fabrication, the inscription beam is orthogonal to the fibre propagation axis and thus, the depth of the modification is dictated by the confocal parameter of the writing beam. In the absence of any beam adapting optics, a Gaussian profile pulse causes an asymmetric modification cross section (Fig.3.7, [31]). The diffraction slit is a common alternative to other beam shaping optics in femtosecond writing arrangements due to its relative simplicity. The slit narrows the beam width in one direction. Subsequently, the reduced beam waist decreases the Rayleigh range in one axis and thus causes rapid divergence after focussing from an objective lens. By controlling the divergence angle in one plane, the symmetry of the induced cross-section can be modified. Mathematically, it has been reported that to achieve a symmetric cross section, the ideal ratio of x and y beam waists, W_x and W_y , is:

$$\frac{W_x}{W_y} = \frac{NA}{n} \sqrt{\frac{\ln 2}{3}} \quad (3.7)$$

where NA is the numerical aperture of the focussing lens and n is the refractive index of the target material [31]. Equation 3.7 is only valid for $W_x > 3W_y$. When writing in an optical fibre, the slit should be orientated parallel to the fibre propagation axis. For both experiments the slit was fixed to $300 \pm 10 \mu\text{m}$.

After the slit, the writing beam was directed by a dichroic mirror through a 0.65 NA objective lens. The fibre was secured onto a 3D-printed fibre platform using two rotational fibre holders and positioned beneath the objective lens. The holder was attached to a high precision air bearing translation stage accurate to $\pm 100 \text{ nm}$ (ANT130, Aerotech). A CCD camera was positioned directly above the dichroic mirror to enable visual imaging of the writing process. An LED was positioned beneath the fibre to provide illumination for the imaging.

When a FBG was being inscribed, a light source and optical spectrum analyser (OSA, AQ6370D, Yokogawa) were connected to allow live characterisation of the FBGs transmission spectrum. Measurements of wavelength and power using the OSA were accurate to $\pm 0.01 \text{ nm}$ and $\pm 0.4 \text{ dB}$. A supercontinuum source (SC400, Fianium) was

used for the high concentration germanium fibre and an EDFA utilised as an Amplified Spontaneous Emission (ASE) source was used for the MCF. The supercontinuum source could not be used to record the transmission spectra of the MCF as the insertion loss was too large.

The point-by-point technique was employed, whereby each grating plane is inscribed individually. FBGs were inscribed in the single pulse regime. The translation stages were controlled using a position synchronised output (PSO) controller (A3200, Aerotech). The PSO was connected to a pulse picker (pockels cell) within the laser. This allowed the grating pitch to be controlled by the synchronisation of laser pulses with the positioning of the fibre. The difference between the laser frequency and the shutter frequency meant beating occurred, however computer simulations revealed this effect to be negligible on the grating pitch.

3.4.3 Computational Analysis

To analyse the recorded transmission spectra of each FBG, computational simulations generated lines of best fit to deduce the induced refractive index. From coupled mode theory, the reflectivity of an ideal, first order, uniform grating can be described by equation 3.3. The ‘‘AC’’ coupling coefficient is expressed by:

$$\kappa = \frac{\pi}{\lambda} \nu \overline{\delta n_{eff}} \quad (3.8)$$

where λ is the wavenegth, ν is the fringe visibility and $\overline{\delta n_{eff}}$ is the ‘‘dc’’ refractive index change. The general self coupling coefficient $\hat{\sigma}$, is equal to:

$$\hat{\sigma} = 2\pi n_{eff} \left(\frac{1}{\lambda} - \frac{1}{\lambda_D} \right) + \frac{2\pi}{\lambda} \nu \overline{\delta n_{eff}} - \frac{1}{2} \frac{d\phi}{dz} \quad (3.9)$$

where n_{eff} is the effective modal index, λ_D is the design wavelength and $\phi(z)$ describes the grating chirp over a distance z . For a uniform grating, the final term is equal to zero. Thus, inputting the grating period, resonance wavelength and trial value of refractive index into equations 3.3, 3.8 and 3.9, a line of best fit was generated. An iterative algorithm determined the ‘‘dc’’ refractive index change by finding the value corresponding to the minimum variance. As all FBGs fabricated were of the 3rd order, the refractive index change Δn has to be adjusted for accordingly. Assuming a periodic, step index profile the 3rd order fourier coefficient is:

$$b_3 = \frac{1}{L} \int_{-L}^L f(x) \sin(6\pi x) dx \quad (3.10)$$

And thus the refractive index change Δn is equal to:

$$\begin{aligned} \Delta n b_3 &= 2 \overline{\delta n_{eff}} \\ \Delta n &= 6\pi \overline{\delta n_{eff}} \end{aligned} \quad (3.11)$$

3.5 Multicore Bragg Gratings

3.5.1 Results

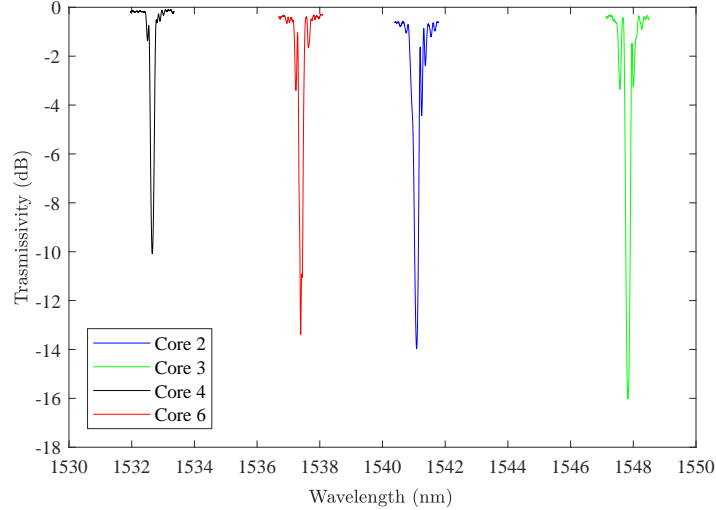


Figure 3.8: Transmission spectra recorded from cores 2, 3, 4 and 6.

Four 3rd order FBGs were inscribed into cores 2, 3, 4 and 6 of the fibre with Bragg resonances $\lambda_B = 1541.01 \pm 0.02$, 1547.82 ± 0.02 , 1532.66 ± 0.02 , and 1537.42 ± 0.02 nm, respectively (Fig.3.8). The gratings were written with a pulse energy of $2.1 \pm 0.2 \mu\text{J}$ and a laser frequency of 1 kHz. A single shot was required to fabricate each grating plane. At the focal volume, the beam had a depth of $10 \mu\text{m}$. Computational analysis was also completed on the resultant transmission spectra to measure the grating period, -3 dB bandwidth and extinction ratio (Table 3.1).

Core Number	Period (μm)	Bragg Wavelength λ_B (nm)	-3 dB Bandwidth (nm)	Extinction ratio (dB)	Refractive index modulation Δn ($\times 10^{-3}$)
2	1.598 ± 0.001	1541.01 ± 0.02	0.28 ± 0.03	13.97 ± 0.40	2.56 ± 0.06
3	1.605 ± 0.001	1547.82 ± 0.02	0.22 ± 0.03	16.02 ± 0.40	2.92 ± 0.06
4	1.589 ± 0.001	1532.66 ± 0.02	0.16 ± 0.03	10.08 ± 0.40	2.07 ± 0.02
6	1.594 ± 0.001	1537.42 ± 0.02	0.18 ± 0.03	13.40 ± 0.40	2.38 ± 0.17

Table 3.1: A summary of the computational analysis completed on the FBG transmission spectra

A 7.5% difference in transmission was observed at the Bragg resonance wavelengths between core 3 and core 4. The lower transmission can be attributed to the difference between the spot diameter in the focal volume and the core diameter. For the HE_{11} mode, an offset of $1 \mu\text{m}$ from the centre of the core can cause a 10% drop in reflectivity. The offset means there is a poorer overlap of the induced modification with the power distribution of the fundamental mode. To improve the consistency of the FBG reflectivity, beam expanding optics could be introduced to increase the spot diameter at the focal point.

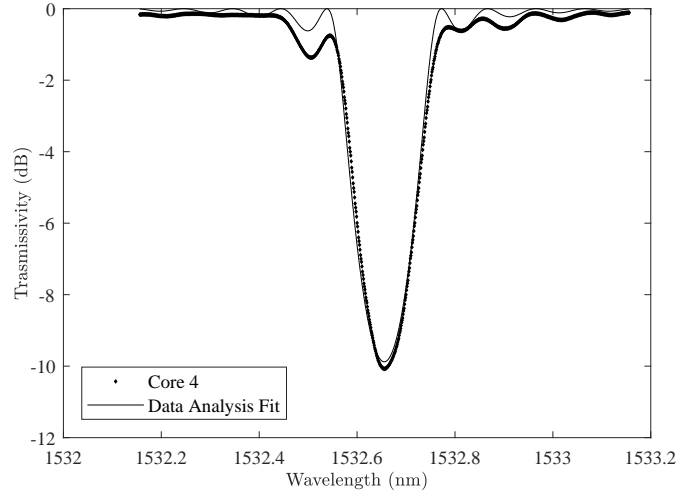


Figure 3.9: The transmission spectra of the grating inscribed within core 4 of Bragg resonance $\lambda_B = 1532.66 \pm 0.02$ nm. Computational analysis applied a line of best fit and deduced the refractive index modulation associated to the grating planes $\delta n = (2.07 \pm 0.02) \times 10^{-3}$.

For core 2, a larger than anticipated bandwidth was recorded. It is believed that systematic errors in the grating period were introduced due to distortion of the induced modification. During the inscription process, core 2 was situated furthest from the writing beam. Given its orientation, the propagation path of the writing beam was non-uniform causing an asymmetric modification to be induced. The asymmetry alters the grating periodicity and thus, causes a broadening of the bandwidth. Despite this, the result demonstrates the ability of the PbP technique to access the deepest cores, lying furthest from the surface. The variation in bandwidth could be mitigated by rotating the fibre to minimise the beam propagation path and in turn, reduce the effect of any non-uniformities.

The core 4 FBG exhibited minimal variance and therefore, behaved most like an ideal grating (Fig.3.9). On the short wavelength side of the Bragg resonance, the measured spectrum exhibits a side-lobe suppression ratio half as large as that predicted by simulations. The core 3 FBG also demonstrated a side-lobe suppression ratio approximately 1.5 times lower than expected, on the longer wavelength side of the Bragg resonance (Fig.3.10). From literature, the lower than expected side-lobe resonances are caused by random phase errors between the grating planes [5]. For the core 4 FBG, the secondary side lobes of the inscribed grating lie 0.11 nm from the Bragg wavelength and are in agreement with the simulated results to 3%. For the core 3 FBG, the secondary resonance location on the long wavelength side of the Bragg resonance is in agreement with the simulated result to less than 1%. The presence of these side lobes verify that a uniform grating was inscribed; apodization would suppress these side lobes and any chirping would show broadening of the Bragg resonance. Side lobes were present in the transmission spectra of all four gratings.

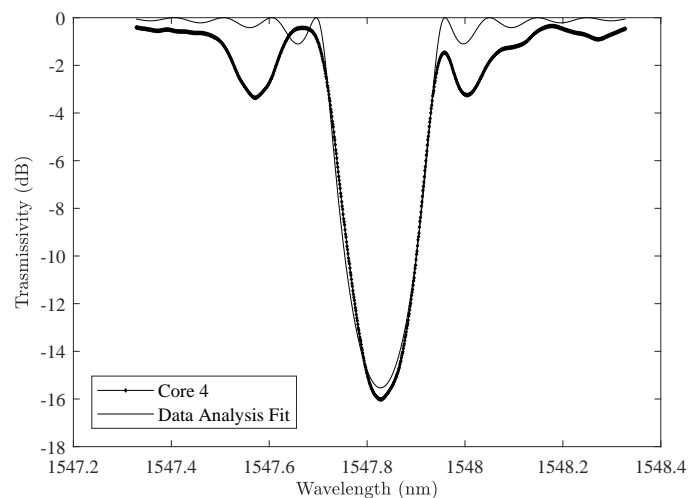


Figure 3.10: The transmission spectra of the grating inscribed within core 3 of Bragg resonance $\lambda_B = 1541.01 \pm 0.02$ nm. Computational analysis applied a line of best fit and deduced the refractive index modulation associated to the grating planes $\delta n = (2.92 \pm 0.06) \times 10^{-3}$.

3.5.2 Conclusions

Using femtosecond laser writing, four FBGs were inscribed into four separate cores of a 7-core fibre, with a 7.5 % variation in reflectivity. The PbP methodology enabled specific cores of a multicore fibre to be targeted and isolated for FBG fabrication; no observable increase in inter-core cross talk was observed. The non-uniformity in reflectivity could be minimised by increasing the laser spot size at the focal point to a diameter comparable to that of the core. Further enhancement of the experimental arrangement would facilitate the ability to inscribe within 6 cores; core 5 is inaccessible due to its proximity to the air hole, distorting its imaging. The number of cores eligible for FBG inscription is determined by the imaging capabilities and spot size of the laser. The image of the core cannot be obscured by other features within the fibre and the spot diameter must be comparable to the core diameter. The technique also presented the additional advantage of inscription through the fibre coating as it was transparent to 1030 nm radiation. If the uniformity grating reflectivity could be improved, the PbP technique applied in conjunction with a femtosecond laser, could be a viable solution for MC-FBG fabrication for SDM solutions.

3.6 High concentration Germania-doped fibre

3.6.1 Results

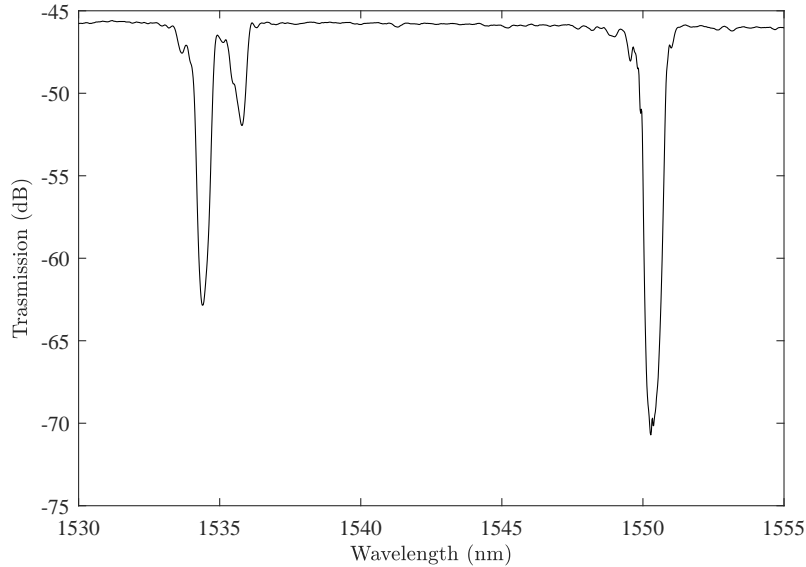


Figure 3.11: The transmission spectra of the high concentration germania-doped FBG.

A 3rd order grating with a design wavelength of 1550 nm was fabricated. From the Bragg condition, the grating pitch was calculated to be $1.548 \pm 0.001 \mu\text{m}$. The FBG was 3 mm long and was fabricated in 30 seconds. The laser frequency was set to 1 kHz and a single pulse regime was utilised. The laser had a pulse energy of 1.1 J and a $10 \mu\text{m}$ depth at the focal point. In the recorded transmission spectra, three Bragg resonances are visible at $\lambda_B = 1534.40 \pm 0.02$, 1535.78 ± 0.02 and 1550.28 ± 0.02 nm of extinction ratios 17.17 ± 0.40 , 6.26 ± 0.40 and 25.00 ± 0.40 dB, and bandwidths of 0.82 ± 0.02 , 0.93 ± 0.02 and 1.10 ± 0.02 nm respectively. The bandwidths were measured at first minima. Computational analysis deduced an average refractive index change of $(1.2 \pm 0.4) \times 10^{-2}$.

FBGs in multimode fibres exhibit multiple resonances due to self coupling between the forward and backward propagating modes, and cross coupling between the differing counter-propagating modes. For a weakly-guiding, step index fibre, if all supported modes are launched into the fibre, the number of Bragg resonances scales with the number of scalar modes n , by $\frac{1}{2}(n^2 + n)$.

Upon initial inspection, assuming a step index profile from Fig.3.5 appears to be acceptable. At 1550 nm the normalised frequency of the fibre was $\simeq 3.06$ and supports two scalar modes (LP_{01} and LP_{11}). Therefore, 3 resonances would be expected. However, in the experiment conducted, only the fundamental mode was launched. Therefore, no self-coupling between the higher order modes occurs. For an ideal uniform grating, the overlap integral between the LP_{01} and LP_{11} mode equates to zero. However, the inscribed FBG is not perfect and so higher order modes are excited from the presence of the induced dielectric perturbation. From this, only two resonances were expected:

the LP_{01} self coupling and cross coupling between the forward propagating LP_{01} and LP_{11} . The $\lambda_B = 1550.28 \pm 0.02$ nm resonance corresponds to the self-coupling of the fundamental mode, as expected. However, the additional resonances were not expected.

Computational simulations (COMSOL Multiphysics) were generated using the fibre refractive index profile (Fig.3.12, [32]). The simulations revealed the TE_{01} and TM_{01} modes were degenerate with an effective modal index of $n_{eff} = 1.4583$. In a standard step index fibre the degeneracy of these two modes is not physically permitted. This is due to the discontinuity in the refractive indices of the core and the cladding. The electric field of the the TM_{01} mode is orthogonal to the boundary, causing the mode possess a lower effective index. For the TE_{01} mode, its electric field is orientated parallel to the boundary; thus, no discontinuity is experienced. Thus, the TE_{01} experiences a higher effective modal index.

However, upon review of the germania-doped fibre refractive index profile, the core-cladding boundary is relatively weakly graded. Therefore, TM_{01} electric field does not experience a discontinuity across the core - cladding boundary. Hence, it propagates with the same effective modal index as TE_{01} . Unlike a step index fibre, the TM_{01} and TE_{01} are not degenerate with the HE_{21} as they are not radially alike. For the HE_{21} mode, the electric field lines begin from the cladding-air boundary and revert back to a point on the cladding-air boundary perpendicularly bisecting the central fibre axis. Thus, as a higher percentage of power is carried within the cladding of the fibre the effective modal index of the HE_{21} mode is lower than that of the TM_{01} and TE_{01} .

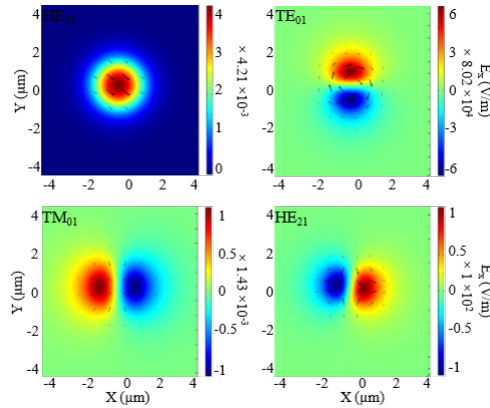


Figure 3.12: Simulated x component of the electric field for the HE_{11} , TE_{01} , TM_{01} and HE_{21} modes. The TE_{01} and TE_{01} modes were degenerate with an effective modal index of $n_{eff} = 1.4583$. The HE_{11} and HE_{21} had effective modal indices of $n_{eff} = 1.4850$ and 1.4578 , respectively.

Hence, from the simulations it was determined that the $\lambda_B = 1534.40$ nm resonance is caused by the forward propagating HE_{11} coupling to the counter-propagating degenerate TM_{01} and TE_{01} modes. The Bragg resonance at $\lambda_B = 1535.78$ nm is due to the coupling between the forward propagating HE_{11} and the counter-propagating HE_{21} mode.

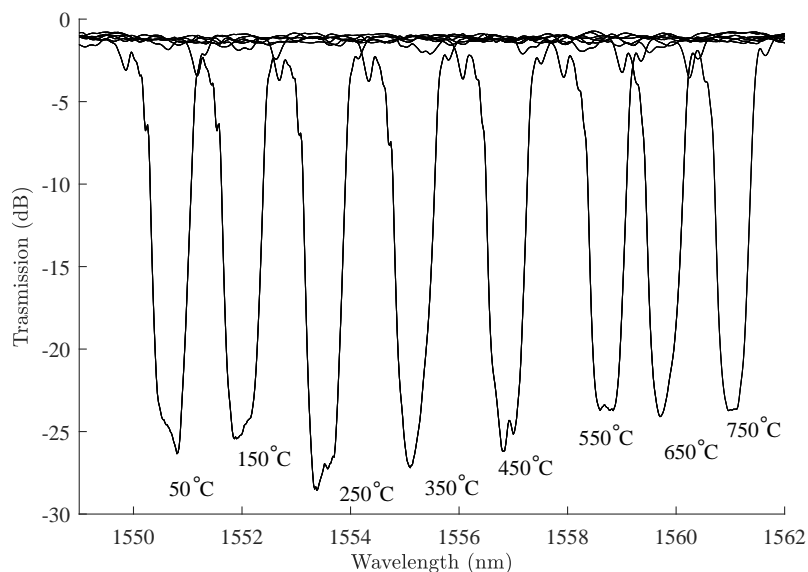


Figure 3.13: The transmission spectra of the HE_{11} self coupling resonance recorded during the thermal tests for temperatures up to 750 °C.

3.6.2 Thermal testing

After fabrication, the high concentration germania-doped FBG thermal stability was investigated. The polymer coating was removed and the FBG was placed within a 400 mm long tubular furnace. An external thermocouple validated the temperature of the furnace. The fibre was thermally tested from room temperature to 800 °C. Transmission spectra were recorded at 50 °C increments from 50 °C. Transmission spectra of the grating were recorded after isochronal periods of 30 minutes using the supercontinuum source and OSA.

Annealing of FBGs is common to improve their uniformity by removing stress and minimizing the effect of thermal history [33]. As with UV written gratings, it is likely that the change in refractive index arises from the multi-photon absorption process that cause defect formation [34]. If heated below the glass transition temperature, the defects can be annealed similarly to type I-UV gratings. Thus, the FBG was heated for 10 hours at 500 °C. After being left to cool naturally, a non-reversible -3.28 ± 0.02 nm shift in the Bragg resonance wavelength was observed (at 20 °C.) The shift corresponds to a decrease in the FBG “dc” index change of 3.1×10^{-6} . Thus, the annealing process was successful in releasing stress induced from the drawing process during the fabrication of the fibre [35].

The transmission spectra recorded during the thermal tests revealed a reversible shift in the Bragg resonance wavelength to longer wavelengths as the furnace temperature increased. Due to the asymmetric nature of the Bragg resonance trough, the central wavelength was taken as the value lying halfway between the first minima. Throughout the thermal tests, the minimum transmission varied between -23 to -29 dB, translating to fluctuations in linear reflectivity of $< 1\%$. These fluctuations can be attributed to a low signal to noise ratio caused by inefficient coupling. The bandwidth of the fundamental mode self-coupling resonance did not vary throughout the thermal tests.

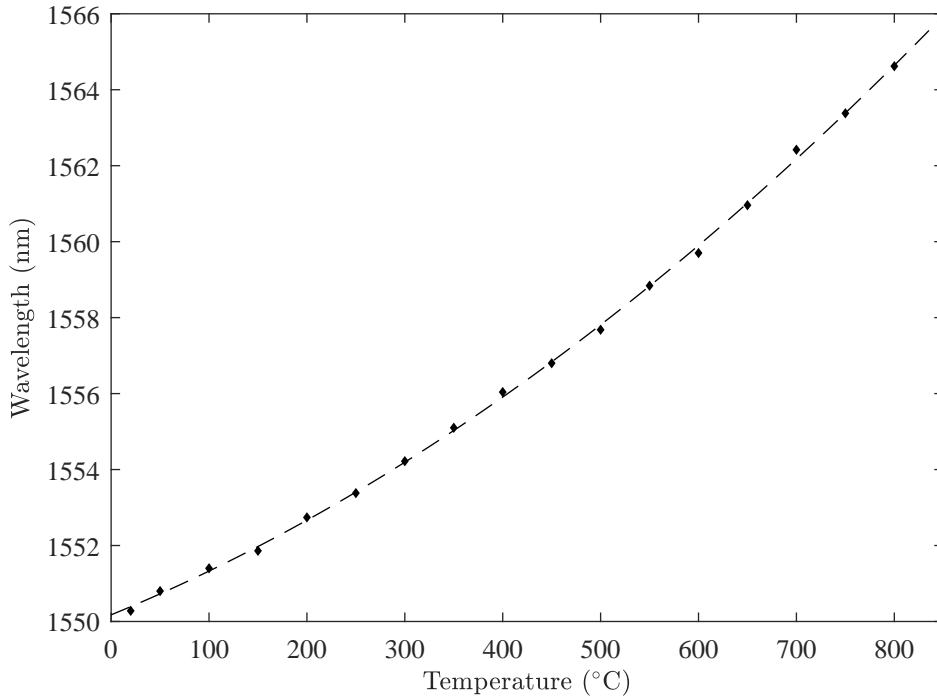


Figure 3.14: A thermal sensitivity plot of the high concentration germania fibre. A quadratic regression line (solid) was applied to the data.

A non-linear relationship was observed between temperature and the Bragg resonance wavelength. A regression line was applied to the data. The first and second order coefficients were calculated $\frac{d\lambda_B}{dT} = 11.1 \text{ pm}^\circ\text{C}^{-1}$ and $\frac{d^2\lambda_B}{dT^2} = 8.37 \times 10^{-3} \text{ pm}^2\text{C}^{-2}$, respectively. From 20 to 100 °C, the fibre had a linear thermal sensitivity $\frac{d\lambda_B}{dT} = 12.10 \pm 0.01 \text{ pm}^\circ\text{C}^{-1}$. The thermal sensitivity of the fibre increased from 700 to 800 °C to $\frac{d\lambda_B}{dT} = 20.20 \pm 0.01 \text{ pm}^\circ\text{C}^{-1}$. Non-linearity has been reported in low concentration germania-doped fibres [36]. In comparison to a 9 mol% germania-doped silica fibre, the fibre used in the experiments above is 35% more sensitive from 0 to 100 °C. From 700 to 800 °C it is 82% more sensitive.

Two material properties are responsible for the observed non-linear thermal behaviour: the thermal expansion coefficient and the thermo-optic coefficient. Germania-silica (40 mol.%) has a thermal expansion coefficient of $\alpha_{Ge-SiO_2} = 43.7 \times 10^{-7} \text{ K}^{-1}$ [37]. Fused silica has a thermal expansion coefficient $\alpha_{SiO_2} = 5.6 \times 10^{-7} \text{ K}^{-1}$ [38]. Thus, the core expands at a rate 8 times greater than its cladding causing a significant change in the stress field within the core. The thermal expansion coefficient is linear in nature and thus, it is not responsible for the non-linear behaviour observed.

The thermo-optic coefficient derives from the polarizability of a material. As a material is heated, atomic and lattice vibrations are generated. In addition, electrons can be thermally excited to higher levels. Both of these effects increase the magnitude of the dipole moments [33]. It has been reported that in fused silica, the rate of change of the thermo-optic coefficient fluctuates with increasing temperature [39]. In the experiment conducted with 40 mol.% germania-doped fibre, similar fluctuations to those reported in

literature were not observed. A minimum has been observed at 400 °C. The differences between the results above and those reported in literature are unclear, but it is thought to be due to the addition of germania to the core. Further testing is required to verify this hypothesis. Thus, the observed non-linear behaviour can be attributed to increases in the thermo-optic coefficient.

3.6.3 Conclusions

Previously, fabrication attempts of FBGs in high concentration germania have been reported [25], but their spectra were never published. This work is the first known high concentration germania FBG to be published using the femtosecond PbP inscription technique [32]. Femtosecond laser writing has demonstrated its capability in fabricating FBGs in fibres whose photosensitive profiles have not been suitable for UV-based inscription techniques. The high concentration germania fibre proved stable up to 800° for 30 minutes, with < 1 % movement in the FBG reflectivity. Its sensitivity at both low and high temperatures was greater than the low concentration (9 mol.%) germania fibre reported [40]. Hypothetically, femtosecond writing could be used to fabricate FBGs in a 100 % germania fibre. Building upon the results presented, two FBGs could be fabricated to form a cavity within a high concentration germania fibre, creating a germania-doped Raman laser and amplifier. Improvements of the current fabrication set up would be required to enable precise control of the FBG reflectivity; this is essential for the creation of an effective cavity.

Bibliography

- [1] Hill, K. O. Aperiodic distributed-parameter waveguides for integrated optics. *Applied Optics* **1974**, *13*, 1853–1856.
- [2] Giles, C. Lightwave applications of fiber Bragg gratings : fiber gratings, photosensitivity, and poling. *Journal of Lightwave Technology* **1997**, *15*, 1391–1404.
- [3] Weller-Brophy, L. A.; Hall, D. G. Analysis of waveguide gratings: application of Rouard’s method. *Journal of the Optical Society of America A* **1985**, *2*, 863–871.
- [4] Yamada, M.; Sakuda, K. Analysis of almost-periodic distributed feedback slab waveguides via a fundamental matrix approach. *Applied Optics* **1987**, *26*, 3474–3478.
- [5] Skaar, J. Synthesis of fiber Bragg gratings. *Journal of the Optical Society of America A* **2001**, *18*, 557–564.
- [6] Erdogan, T. Fiber grating spectra. *Journal of Lightwave Technology* **1997**, *15*, 1277–1294.
- [7] Bhatia, V.; Vengsarkar, A. M. Optical fiber long-period grating sensors. *Optics Letters* **1996**, *21*, 692.
- [8] Erdogan, T.; Sipe, J. Tilted fiber phase gratings. *Journal of the Optical Society of America a-Optics Image Science and Vision* **1996**, *13*, 296–313.
- [9] Erdogan, T. Cladding-mode resonances in short- and long- period fiber grating filters. *Journal of the Optical Society of America. A, Optics, image science, and vision* **1997**, *14*, 1760–1773.
- [10] Mizrahi, V.; Sipe, J. E. Optical properties of photosensitive fiber phase gratings. *Journal of Lightwave Technology* **1993**, *11*, 1513–1517.
- [11] Hill, K. O.; Meltz, G. Fiber Bragg grating technology fundamentals and overview. *Journal of Lightwave Technology* **1997**, *15*, 1263–1276.
- [12] Martinez, A.; Khrushchev, I. Y.; Bennion, I. Direct inscription of Bragg gratings in coated fibers by an infrared femtosecond laser. *Optics Letters* **2006**, *31*, 1603.
- [13] Malo, B.; Hill, K. O.; Bilodeau, F.; Johnson, D. C.; Albert, J. Point-by-point fabrication of micro-Bragg gratings in photosensitive fibre using single excimer pulse refractive index modification techniques. *Electronics Letters* **1993**, *29*, 1668–1669.
- [14] Marshall, G. D.; Williams, R. J.; Jovanovic, N.; Steel, M. J.; Withford, M. J. Point-by-point written fiber-Bragg gratings and their application in complex grating designs. *Optics Express* **2010**, *18*, 19844–19859.
- [15] Martinez, A.; Dubov, M.; Khrushchev, I.; Bennion, I. Direct writing of fibre Bragg gratings by femtosecond laser. *Electronics Letters* **2004**, *40*, 1170.
- [16] Fertein, E.; Przygodzki, C.; Delbarre, H.; Hidayat, A.; Douay, M.; Niay, P. Refractive-index changes of standard telecommunication fiber through exposure to femtosecond laser pulses at 810 nm. *Applied Optics* **2001**, *40*, 3506.
- [17] Thomas, J. U.; Jovanovic, N.; Krämer, R. G.; Marshall, G. D.; Withford, M. J.; Tünnermann, A.; Nolte, S.; Steel, M. J. Cladding mode coupling in highly localized fiber Bragg gratings II: complete vectorial analysis. *Optics Express* **2012**, *20*, 21434.

-
- [18] Thomas, J. U.; Jovanovic, N.; Krämer, R. G.; Marshall, G. D.; Withford, M. J.; Tünnermann, A.; Nolte, S.; Steel, M. J. Cladding mode coupling in highly localized fiber Bragg gratings II: complete vectorial analysis. *Optics Express* **2012**, *20*, 21434.
- [19] Richardson, D. J.; Fini, J. M.; Nelson, L. E. Space-division multiplexing in optical fibres. *Nature Photonics* **2013**, *7*, 354–362.
- [20] Lindley, E.; Min, S.-S.; Leon-Saval, S.; Cvetojevic, N.; Lawrence, J.; Ellis, S.; Bland-Hawthorn, J. Demonstration of uniform multicore fiber Bragg gratings. *Optics Express* **2014**, *22*, 31575–31581.
- [21] Wang, C.; Yan, Z.; Sun, Q.; Sun, Z.; Mou, C.; Zhang, J.; Badmos, A.; Zhang, L. Fibre Bragg gratings fabrication in four core fibres. *Micro-Structured and Specialty Optical Fibres IV* **2016**, *9886*, 1–9.
- [22] Galeener, F. L.; Mikkelsen, J. C.; Geils, R. H.; Mosby, W. J. The relative Raman cross sections of vitreous SiO₂, GeO₂, B₂O₃, and P₂O₅. *Applied Physics Letters* **1978**, *32*, 34–36.
- [23] Boskovic, A.; Chernikov, S. V.; Taylor, J. R.; Gruner-Nielsen, L.; Levring, O. A. Direct continuous-wave measurement of $n(2)$ in various types of telecommunication fiber at 1.55 micrometers. *Optics Letters* **1996**, *21*, 1966–8.
- [24] Davey, S.; Williams, D.; Ainslie, B.; W.J.M., R.; Wakefield, B. Optical gain spectrum of GeO₂-SiO₂ Raman fibre amplifiers. *IEE Proceedings J (Optoelectronics)* **1989**, *136*, 301–306(5).
- [25] Medvedkov, O. I.; Vasiliev, S. A.; Gnusin, P. I.; Dianov, E. M. Photosensitivity of optical fibers with extremely high germanium concentration. *Optical Materials Express* **2012**, *2*, 1478.
- [26] Lancry, M.; Poumellec, B.; Canning, J.; Cook, K.; Poulin, J. C.; Brisset, F. Ultrafast nanoporous silica formation driven by femtosecond laser irradiation. *Laser and Photonics Reviews* **2013**, *7*, 953–962.
- [27] Canning, J. Photosensitization and photostabilization of laser-induced index changes in optical fibers. *Optical Fiber Technology* **2000**, *6*, 275–289.
- [28] Dong, L.; Pinkstone, J.; Russell, P. S. J.; Payne, D. Ultraviolet absorption in modified chemical vapor deposition preforms. **1994**, *11*, 2106–2111.
- [29] Chan, J. W.; Huser, T.; Risbud, S.; Krol, D. M. Structural changes in fused silica after exposure to focused femtosecond laser pulses. *Optics Letters* **2001**, *26*, 1726.
- [30] Limberger, H. G.; Ban, C.; Salathé, R. P.; Slattery, S. a.; Nikogosyan, D. N. Absence of UV-induced stress in Bragg gratings recorded by high-intensity 264 nm laser pulses in a hydrogenated standard telecom fiber. *Optics Express* **2007**, *15*, 5610–5615.
- [31] Ams, M.; Marshall, G. D.; Spence, D. J.; Withford, M. J. Slit beam shaping method for femtosecond laser direct-write fabrication of symmetric waveguides in bulk glasses. *Optics Express* **2005**, *13*, 5676–5681.
- [32] Donko, A.; Nunez-Velazquez, M.; Beresna, M. Femtosecond Inscription And Thermal Testing Of Bragg Gratings In High Concentration Germania-Doped Optical Fibre. *Optics Express* **2017**, *25*, 32879–32886.

-
- [33] Tروف, W. J.; Thomas, M. E.; Harris, T. J. *Handbook Of Optics*; 1995; Chapter 33, pp 33.1 – 33.3.
- [34] Li, Y.; Liao, C. R.; Wang, D. N.; Sun, T.; Grattan, K. T. V. Study of spectral and annealing properties of fiber Bragg gratings written in H₂-free and H₂-loaded fibers by use of femtosecond laser pulses. *Optics Express* **2008**, *16*, 21239–21247.
- [35] Kim, B. H.; Park, Y.; Ahn, T.; Kim, D. Y.; Lee, B. H.; Chung, Y.; Paek, U. C.; Han, W. Residual stress relaxation in the core of optical fiber by CO₂ laser irradiation. *Optics Letters* **2001**, *26*, 1657–1659.
- [36] Meltz, G.; Morey, W. Bragg grating formation and germanosilicate fiber photosensitivity. International Workshop on Photoinduced Self-Organization Effects in Optical Fibre. 1991.
- [37] Riebling, E. F. Nonideal Mixing in Binary GeO₂-SiO₂ Glasses. *Journal of the American Ceramic Society* **1968**, *51*, 406–407.
- [38] Oishi, J.; Kimura, T. Thermal Expansion of Fused Quartz Thermal Expansion of Fused Quartz. *Meteorologia* **1969**, *5*, 50–55.
- [39] Adamovsky, G.; Lyuksyutov, S. F.; Mackey, J. R.; Floyd, B. M.; Abeywickrema, U.; Fedin, I.; Rackaitis, M. Peculiarities of thermo-optic coefficient under different temperature regimes in optical fibers containing fiber Bragg gratings. *Optics Communications* **2012**, *285*, 766–773.
- [40] Meltz, G.; Morey, W. W.; Glenn, W. H. Formation of Bragg gratings in optical fibers by a transverse holographic method. *Optics Letters* **1989**, *14*, 823.

Chapter 4

Distributed Acoustic Sensing and Enhanced Signal Fibres: Principles and Literature Review

4.1 Introduction

Fibre optic sensors can be classified according to whether they are extrinsic or intrinsic. Extrinsic sensors are where the optical fibre is used as a communication path between the light source and an external sensing head. Intrinsic sensors exploit the optical fibre itself as the sensing element.

Within the category of intrinsic fibre sensors, there exists further subdivisions: point sensors, quasi-distributed sensors and distributed sensors (Fig. 4.1). One of the most common point sensors is a Mach-Zehnder interferometer. One arm is isolated, remaining as a reference arm and the other is exposed to the environment being monitored. Parameters are determined via the fluctuations in intensity when the reference and sensing arms interfere with one another. Mach-Zehnder interferometers are commonly found in hydrophones for underwater acoustic detection.

The second category, quasi-distributed fibre sensors. This class of sensors is defined by the use of multiple point sensors along the length of a fibre, which are multiplexed by a single interrogating unit. Most commonly, fibre Bragg gratings are used. By placing them at periodic intervals, absolute measurements can be determined via changes in the Bragg resonance wavelength. Parameters such as strain and temperature effect the Bragg resonance wavelength.

The final category, distributed fibre sensing, is a well established method for monitoring parameters over long distances. The sensors do not rely on the introduction of additional elements. Distributed fibre sensors rely on detecting either Rayleigh, Brillouin or Raman scattered light to determine environmental parameters. As scattering occurs

in all directions, a proportion will be scattered back along the fibre. By analysing the backscattered light, environmental parameters can be determined.

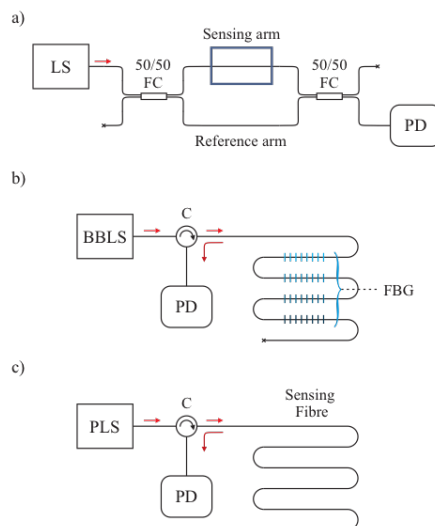


Figure 4.1: Three types of intrinsic optical fibre sensors (a) single point sensor (b) quasi-distributed sensor, and (c) distributed sensor. **LS** - Laser source; **FC** - Fibre coupler; **PD** - Photodetector; **BBLs** - Broad-band laser source; **C** - Circulator; **FBG** - Fibre Bragg grating; **PLS** Pulsed laser source [1].

Today, optical fibre sensors are an integral part of society. These devices have been attractive for commercial applications given their rugged nature, flexibility and high sensitivity. Typically, single point optical fibre sensors can be up to two orders of magnitude more expensive than electronic based elements [2]. Distributed fibre sensors have emerged in the last decade as a solution due to their exploitation of telecommunications fibre costing less than 1 pence per meter. Distributed optical fibre sensors rely on a unique mechanism utilising one set of optical elements to interrogate and spatially resolve measurable properties. This methodology allows orders of magnitudes of point sensors (typically $> 10^5$) to be replaced by a light source, fibre, and detector [3].

Since discovery, distributed fibre sensing research has focussed on measuring absolute parameters via analysis of inelastic scattering phenomena occurring in the optical fibre. Commercially, Brillouin- and Raman-based systems have emerged as the distributed sensing mechanism of choice for long distance temperature measurements [4]. For long distance strain measurements, Brillouin- and Rayleigh-based systems have been employed. This is due to their simplicity and precision. More recently, a new sector of distributed optical fibre sensor has been established with the ability to detect vibrations or acoustic waves. These measurements are made by evaluating dynamic strain. The sector has rapidly developed due to growing demand from oil and gas, geophysical and structural health applications. Early research focussed upon solely detecting dynamic perturbations but recent advances have allowed quantification of these vibrations.

The following sections describe the principles underlying these systems and their operation. After, the concept of enhanced Rayleigh scattering fibres is introduced and

analysed in reference to these dynamic strain measurement systems.

4.2 Fundamental Theory of Distributed Fibre Sensing

4.2.1 Theory of Light Scattering

Although often simplified, the fundamental phenomena of light scattering involves a complex interaction between a propagating electromagnetic field and the scattering media. Within an optical fibre, there are three main scattering processes: Rayleigh; Brillouin; and Raman scattering. As the scope of this work covers only distributed vibration sensing, only Rayleigh and Brillouin scattering will be reviewed in the following section.

Rayleigh scattering

The Rayleigh scattering process is elastic in nature. It is significant only when the radius of the scattering particle r_{sp} meets the following condition:

$$r_{sp} < \frac{1}{10}\lambda \quad (4.1)$$

where λ is the wavelength of the incident electromagnetic field. The process originates from the effect of a propagating electromagnetic wave on the medium's electron cloud. As the wave approaches, the electron cloud undergoes a periodic perturbation. Subsequently, a systematic polarization of atoms in the vicinity occurs, leading to the formation of an oscillating dipole. Subsequently, the radiation emitted by the oscillating dipole is known as Rayleigh scattering. As the dipole oscillation frequency is equal to the frequency of incident radiation, the scattered radiation possesses the same properties as the initial electromagnetic wave.

For a homogeneous medium, the result of the integral in all directions is zero, except for in the direction of propagation of the EM wave [5]. Hence, Rayleigh scattering only occurs in inhomogeneous media. In the context of an optical fibre, Rayleigh scattering is caused by inhomogeneities frozen in the fibre during its fabrication. Numerically, the coefficient of Rayleigh scattering can be expressed as:

$$\gamma_R = \frac{8\pi^3}{3\lambda^4} n(\lambda)^8 p^2 \beta_T K T_F \quad (4.2)$$

where $n(\lambda)$ is the wavelength-dependent refractive index of the optical fibre, p is the average photoelastic coefficient, β_T is the isothermal compressibility at T_F , K is Boltzmann's constant and T_F is the fictive temperature.

Brillouin scattering

Brillouin scattering derives from the $\chi^{(3)}$ non-linearity of a material. The quantized vibrational and rotational modes of atoms or molecules comprising a solid are known as phonons. These phonons can be excited thermally and subsequently propagate through

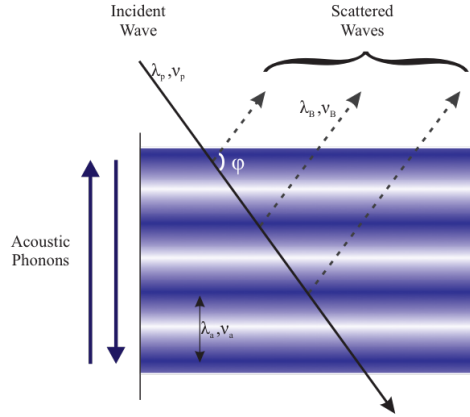


Figure 4.2: A diagram of Brillouin scattering λ_B of incident light λ_p from interacting with thermally generated acoustic wave λ_a [1].

the material as acoustic waves. In an amorphous solid, the phonons propagate in all directions over a wide range of frequencies. Acoustic phonons are defined by the in-phase nature of the oscillations of atoms or molecules. Hence, the propagating acoustic waves can be modelled as a periodic change in refractive index, propagating through a material. Within an optical fibre, if a travelling photon encounters an acoustic wave, these waves couple together and scattering of the incident electromagnetic wave can occur; this is known as Brillouin scattering. The propagating refractive index modulation is analogous to a dynamic Bragg grating. Therefore, only those acoustic phonons satisfying the Bragg condition will cause scattering:

$$\lambda_p = 2n\lambda_a \sin\left(\frac{\theta}{2}\right) \quad (4.3)$$

where λ_p is the wavelength of incident light, λ_a is the wavelength of the acoustic wave and θ is the angle between the incident and scattered light (Fig. 4.2). In the fibre, only light travelling in directions close to the propagation axis can be detected ($\theta = 90^\circ$). Additionally, given that the acoustic phonons travel with a velocity V_a and possess a frequency ν_a , Eq. 4.3 can be rewritten as:

$$\nu_a = \frac{2n}{\lambda_p} V_a \quad (4.4)$$

Eq. 4.4 expresses the frequency of the acoustic phonons in terms of the wavelength of incident light, the velocity of the acoustic wave and the fibre refractive index. As the incident light encounters a dynamic diffractive structure, the scattered light undergoes a Doppler shift. The frequency shift in the incident and scattered electromagnetic waves is equal to the frequency of the acoustic wave:

$$|\nu_p - \nu_{BS}| = |\Delta\nu| = \frac{2n}{\lambda_p} V_a \quad (4.5)$$

where ν_p is the frequency of the incident photon and ν_{BS} is the frequency of the Brillouin scattered photon in the direction parallel to the fibre axis. Whether the frequency shift $\delta\nu$, is positive or negative depends on whether the acoustic wave is co-propagating or counter propagating with the incident electromagnetic wave. The Brillouin scattering coefficient can be expressed as [6]:

$$\gamma_{BS} = \frac{8\pi^3}{3\lambda^4} n^8 p^2 KT (\rho V_a^2)^{-1} \quad (4.6)$$

where T is the absolute temperature, p is the average photoelastic coefficient, and ρ is the average density of the fibre. Thus, Eq. 4.5 demonstrates the dependency of the scattered light on the refractive index of the fibre and velocity of the acoustic wave. Both parameters are dictated by the environmental conditions (temperature and strain) surrounding the fibre. Thus, by measuring the frequency and intensity of the backscattered light strain and temperature can be measured along a fibre [7, 8].

4.2.2 Comparing Rayleigh and Brillouin Scattering

Distributed fibre sensors utilise Rayleigh or Brillouin scattering to monitor dynamic strain over a relatively large distance. Brillouin scattering offers an advantage as it can be optically stimulated to enhance its backscatter signal. Spontaneous Brillouin scattering is directly proportional to its pump intensity, at low powers. As pump power is increased, its subsequent Stoke wave response grows due to electrostriction. The combination of pump light and backscattering Stokes light generates a forward propagating grating [9]. Subsequently, the Brillouin Stokes power is enhanced. By driving the pump light beyond its threshold level, a major change in refractive index occurs, causing larger transfer of pump light into the backscattered Brillouin beam. This methodology of enhancement is known as stimulated Brillouin scattering (SBS).

The Rayleigh backscatter signal is the largest in magnitude, with the intensity of spontaneous Brillouin scattering ~ -20 weaker relative to the Rayleigh signal. The low magnitude of these signals mean Brillouin sensing systems have a lower signal to noise ratio. To achieve a signal to noise ratio adequate for distributed sensing applications, significant averaging is required (on the order $\sim 10^2$) during the analysis of the backscattered spectrum. Hence, Brillouin based distributed fibre sensors are quasi-static in nature.

Brillouin scattering is affected by both temperature and strain variation as shown the dependency of the frequency shift on refractive index in Eq.4.5. Furthermore, Eq.4.6 demonstrates dependency of its intensity on temperature and strain. By monitoring both the amplitude of the scattering and the frequency shift, strain and temperature can be simultaneously measured. The Stokes and anti-Stokes component of Brillouin scattering mirror one another under strain and temperature variations. If both components can be recorded, measurements can be made more simply as a secondary reference is available. Apart from its larger magnitude, Rayleigh scattering further differentiates itself from its counterpart by its coherent nature. The coherent back-signal is unfavourable for mapping the loss along a fibre, however, it is useful for determining dynamic disturbances.

4.3 Distributed Acoustic Sensors - Rayleigh Scattering

4.3.1 Optical Time Domain Reflectometry

OTDR is the simplest method for measuring perturbations along an optical fibre. The methodology operates on the principle of coupling light into a fibre and analysing the backscattered signal at the launch point. The resultant output is a graph of a measured property of the signal against time. Time can easily converted into distance along the fibre using the effective modal index of the fibre. The intensity of a backscattered signal,

measured at the point light is launched into the fibre, is equal to [10]:

$$I(t) = \frac{1}{2} v_g I_0 t_p S \gamma_S \exp(-2\alpha_T z) \quad (4.7)$$

where v_g is the group velocity, I_0 is the peak intensity, t_p is the launched pulse temporal width, γ_S is the relevant scattering coefficient, α_T is the total attenuation coefficient z , is the distance from the front end of the fibre and S is the fraction of capture which, for a step index fibre, is mathematically expressed as:

$$S = \frac{NA^2}{4.3n^2} \quad (4.8)$$

where NA is the numerical aperture of the fibre [10].

OTDR distributed fibre sensors can be subdivided into categories based upon the scattering mechanism that is measured. For Rayleigh OTDR, there are several ways the backscattered signal can be analysed. There is polarization OTDR (POTDR), phase OTDR (ϕ -OTDR) and coherent OTDR (COTDR). Since the Rayleigh backscatter signal is coherent, analysis of the polarization and phase in POTDR and ϕ -OTDR, respectively, can be used for detection. COTDR monitors variations in the intensity of the Rayleigh backscattered signal. For all POTDR, COTDR and ϕ -OTDR perturbations have been detected [11] but only ϕ -OTDR has managed to quantify the perturbations.

4.3.2 ϕ -Optical Time Domain Reflectometry

Fundamentally, ϕ -OTDR measures the phase of Rayleigh backscattered light from the entire length of sensing fibre. If the fibre is divided into equal sections, the phase difference between the light back scattered from two ends of a given section is linearly proportional to the length of the section. Hence, by measuring the phase variation in the Rayleigh backscattered light from the start and end of each section, the strain imparted on that region can be quantified.

The first distributed vibration sensor was proposed by Dakin and Lamb using a dual-pulse methodology (Fig. 4.3a) [12]. Two probes with a relatively small shift in frequency, f_1 and f_2 are launched into a sensing fibre, separated by a time ΔT . The separation in the time domain means light backscattered from point x_1 mixes with light backscattered from x_2 . The spatial separation between x_1 and x_2 is $\Delta x = \Delta T \cdot c/2n$, where c is the speed of light in a vacuum and n is the effective refractive index of the mode travelling in the fibre. Thus, the signal measured at the photodetector is a superposition of two traces of beat frequency $\Delta f = |f_1 - f_2|$. The phase of the beat signal at a section is linearly related to the strain imparted upon the fibre. For Dakin and Lamb's set up to effectively measure vibrations, precise control over phase was required. In 2014, Alekseev et al. demonstrated that vibrations could be measured via control of the relative phase of a dual pulse probe signal [13]. From this, 230 Hz perturbations were detected over 2 km with a spatial resolution of 5 m.

Alternatively to the dual-pulse regime, a methodology based upon an imbalanced Mach-Zehnder interferometer (MZI) was proposed by Posey et al. (Fig. 4.3b) [14]. The backscattered light from a single probe pulse is divided in two and launched into an MZI where the imbalance in the two arms, ΔL , provides a temporal shift $\Delta T = \Delta L \cdot n/c$ between the two traces. Following this, the two traces are recombined at a 3x3 coupler with a phase difference of $\frac{2}{3}\pi$ between each output. The differential phase information

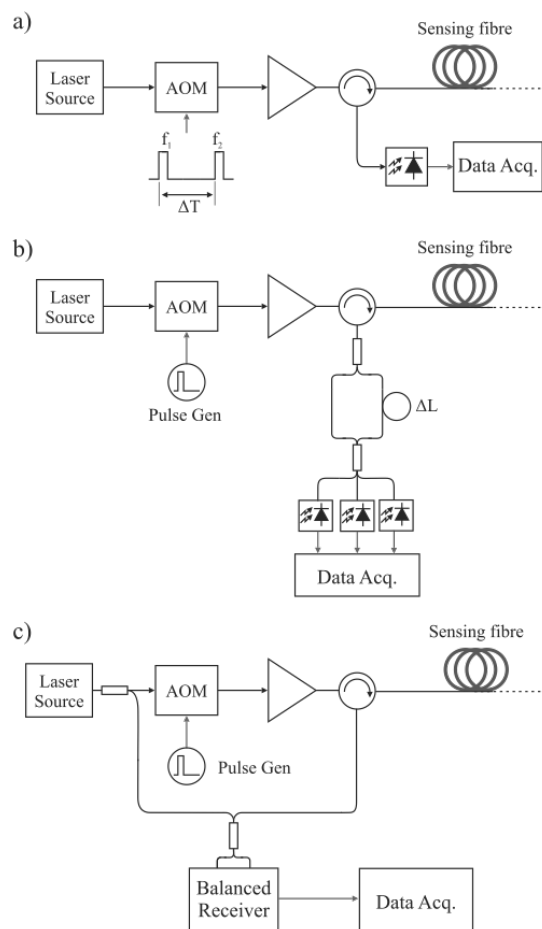


Figure 4.3: Schematic diagrams of the experimental arrangements for ϕ -OTDR measurements: a) Dual-pulse regime (b) Spatial or time derivative methodology (c) Electrical domain measurement. AOM - Acoustic Optic Modulator [1].

at a section of fibre, identified as a red dot in the train of traces in Fig. 4.4a, can be evaluated via gating backscattered signals from the region of interest, and separated using a phase-demodulator. Using this methodology, a 2 kHz perturbation was measured at the midpoint of a 400 m long fibre.

Masoudi et al. and Farhadiroushan et al. built upon this work to independently realise distributed acoustic vibration sensing systems[15, 16, 17]. In their technique, the measured backscattered traces can be differentiated in two ways: as a function of time - temporal derivative or slow axis derivative as demonstrated by Masoudi et al.; or as a function of space - spatial derivative or fast axis derivative as demonstrated by Farhadiroushan (Fig. 4.4b). Masoudi et al. quantify the vibrations using a computer algorithm to measure the temporal derivative. Using this, a strain range of $2 \mu\epsilon$ and frequency range of 4 kHz was measured over a 1 km length of sensing fibre. A spatial resolution of 1 m was demonstrated.

The other methodology to measure acoustic waves using ϕ -OTDR is based upon evaluation of the electronic domain. Hertog and Kader converted the optical data to

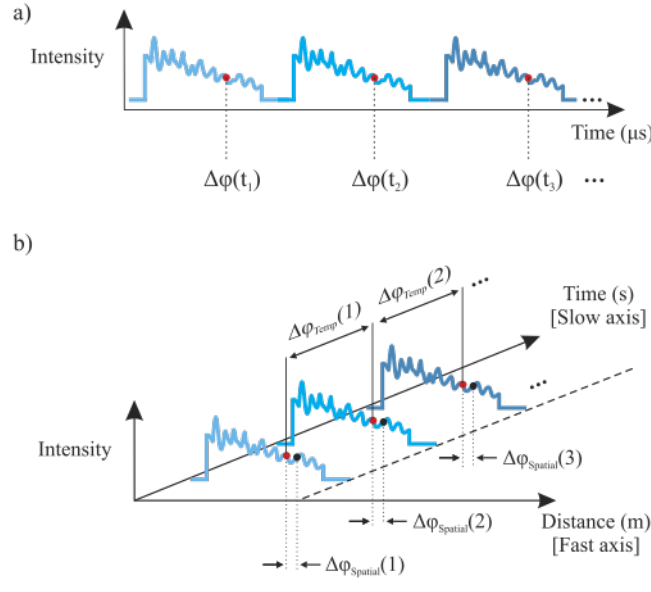


Figure 4.4: A diagram demonstrating the sensing principle of an interferometric ϕ -OTDR sensor using a) signal gating measurement technique and b) distributed measurement technique [18].

an electronic domain, before measuring the phase difference [19]. To do so, an acoustic optic modulator (AOM) produce a frequency shift, δf relative to the source. A balanced photodetector is used to mix Rayleigh backscattered light with the pump. A beat signal is produced containing amplitude and phase information from the fibre under interrogation. The phase is extracted using a phase detection circuit. Tu et. al measured vibrations up to 80 Hz along 25 km of fibre [20]. The measurement had a strain range of $400 n\epsilon$ and a spatial resolution of 10 m.

ϕ -OTDR has its limitations. Primarily, it is disadvantaged over its Brillouin counterpart as only relative strains can be assessed. This is due to its exploitation of the relative phase. The basis of this further limits the linearity of its responses [21]. In these techniques, strain is measured based upon the phase relation between two ends of a sensing section. Hence, the intrinsic phase at the two ends of a section are integral to the linearity of the response. The Rayleigh backscatter signal naturally occurs from the inhomogeneities frozen within the fibre at the point of fabrication. If the inhomogeneity distribution of the two ends are immune to strain, the two ends would have a linear relationship with phase. If the vibration affects the distribution of inhomogeneities at the two ends, a non-linear response is generated which translates into noise within the measurement.

The other major limitation for ϕ -OTDR is signal fading. The signal generated from Rayleigh scattering along the sensing fibre is a sum of all the backscattered photons, with arbitrary phases, from the stochastic distribution of scattering centres contained within the region of interest. As such, ϕ -OTDR systems can experience significant variations in the power of scattered light. These may approach the noise floor and can result in the signal becoming undetectable.

4.3.3 Optical Frequency Domain Reflectometry

In OFDR, a continuous wave tunable laser, with a narrow line width (on the order of \sim kHz), is coupled into a sensing fibre, whilst its frequency is scanned over a set range (Fig. 4.5). By scanning through the frequencies, it is possible to determine the frequency of the backscattered signal along the complete length of the optical fibre [22]. The backscattered light is mixed with the light source and subsequently, a group of beat frequencies is produced. The magnitude of beat frequencies correspond to fibre length: smaller frequencies related to the front end of the fibre; larger beat frequencies provide data from the far-end of the fibre (Fig. 4.5.) The relationship between the beat frequency Ω , and distance along the fibre, z can be mathematically expressed as:

$$\Omega = \frac{2z}{v_g} \frac{d\omega}{dt} \quad (4.9)$$

where v_g is the group velocity of the fibre and $\frac{d\omega}{dt}$ is the rate at which the optical frequency of the laser source is swept. Froggatt et al. proposed a more sophisticated technique to demonstrate the first dynamic strain measurement using OFDR [23]. Their system exploited the reliance of the Rayleigh backscattered light on wave number as well as the fluctuations in permittivity along the sensing fibre. Mathematically the backscattered intensity ϕ can be expressed as:

$$\phi(\beta) = \frac{E_0\beta}{2i} \int \frac{\Delta\epsilon(z)}{\epsilon} \exp(i2\beta z) dz \quad (4.10)$$

where E_0 is the amplitude of the incident electromagnetic wave, β is the wave number, $\Delta\epsilon_z$ is the variation of permittivity with distance z and ϵ is the mean permittivity of the fibre. Eq.4.10 informs us that the complex component of backscattered light at a specified wave number equates to the spatial Fourier transform of variations in the fibre permittivity, as a function of distance. Thus, from the intensity of the backscattered signal, the strain imparted on the sensing fibre can be determined from the cross correlation of traces.

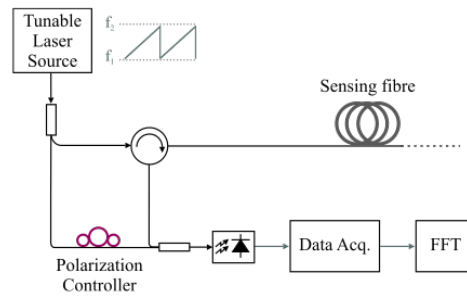


Figure 4.5: A schematic of the experimental set up to make a optical frequency domain reflectometry measurement. FFT - Fast Fourier transform [18].

When measuring dynamic strain, OFDR has the advantage over ϕ -OTDR systems as it has the potential to make quantifiable measurements. Furthermore, OFDR systems possess high spatial resolution. Zhou et al. demonstrated this, making measurements at 10 cm intervals [24]. However, in their demonstration they were restricted to a sensing range of 17 m and frequency range of 32 Hz. Furthermore, OFDR has a limited strain range, typically on the order of $\sim \mu\epsilon$. The cross correlation process relies heavily on

a uniform distribution of inhomogeneities. Any change in distribution translates into noise of the OFDR measurement.

In dynamic strain measurements, OFDR systems cannot be described as distributed fibre sensors as they may only record a measurement from a single location at any given time [25]. The limited strain range and inability to simultaneously monitor the entire sensing fibre at once has restricted the adoption of the OFDR measurement technique in distributed fibre sensing applications.

4.4 Distributed Acoustic Sensors - Brillouin Based

4.4.1 Brillouin Optical Time Domain Reflectometry

Brillouin OTDR (BOTDR) is similar to the Rayleigh based OTDR in section 4.3.1, except it relies on monitoring the frequency shift and intensity of the spontaneous Brillouin backscatter (Fig. 4.6). From this signal, strain and temperature measurements can be made at points along a fibre. The low magnitude of the spontaneous Brillouin scattering signal limits the range of a BOTDR sensor. The intensity of Brillouin backscattered light I_B at the front-end of the fibre is given by:

$$I_B = \frac{1}{2} v_g I_0 t_p S \gamma_B \exp(-2\gamma x) \quad (4.11)$$

where γ_B is the Brillouin scattering coefficient; v_g is the group velocity; I_0 is the peak intensity of the input pulse; t_p is the pulse width; S is the capture fraction; γ is the attenuation coefficient; and x is the distance from the front-end of the fibre. There are

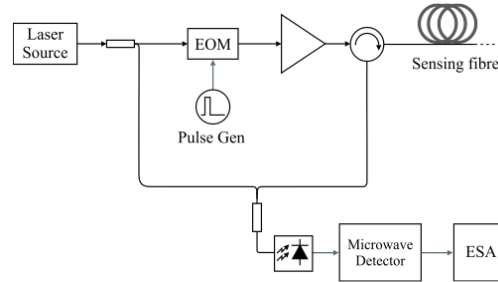


Figure 4.6: A schematic of an experimental set up to make Brillouin optical time domain reflectometry measurements. EOM - Electro optic modulator; ESA - Electronic Spectrum Analyser [18].

two major limitations for BOTDR. First, as mentioned previously, the Brillouin signal is extremely weak meaning vast averaging is required. Secondly, measuring the Brillouin gain spectrum with a microwave detector is time consuming. These limitations restrict the BOTDR's dynamic strain range. Wang et al. performed a measurement over 4 km of fibre, measuring a detectable frequency of 11 Hz [26]. Their results had a spatial resolution of 10 m and a strain range up to 100 $\mu\epsilon$.

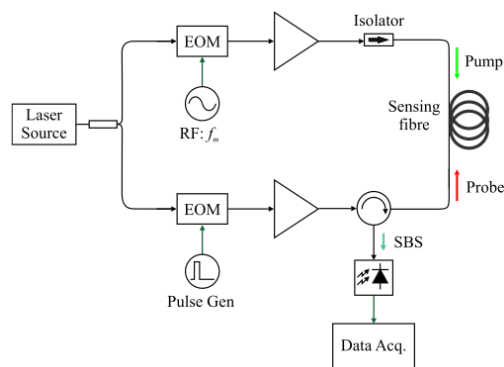


Figure 4.7: A schematic of an experimental set up to make Brillouin optical time domain analysis measurements. EOM - electro optic modulator; SBS - stimulated Brillouin scattering [18].

4.4.2 Brillouin Optical Time Domain Analysis

To exceed this, a technique known as Brillouin optical time-domain analysis (BOTDA) was developed. In BOTDA stimulated Brillouin scattering (SBS) is induced which increases the intensity of the Brillouin backscattered signal [27]. In turn, this improves the signal to noise ratio. To do so, an optical pulse is launched into one end of a fibre and a continuous pump signal is launched into the other. The frequency difference between the two sources is equal to the Brillouin frequency shift. When the two electromagnetic waves superpose one another, stimulated Brillouin scattering occurs at points which meet the Bragg condition. Thus, by scanning the frequency of either the continuous pump signal or the optical pulse signal, the strain and temperature along the fibre can be interrogated (Fig. 4.7) [28]. Brown et al first demonstrated this technique [29]. Using a sampling rate of 2 kHz a strain resolution of $200 \mu\epsilon$ was achieved with a spatial resolution of 10 m over a 120 m sample. Measurements were relatively slow as the frequency difference Δf , between the pump and interrogating signal had to be stepped to map the entire Brillouin gain spectrum. Thus, it was not suitable for dynamic strain measurements.

Improvements of frequency range were made using an adapted methodology known as Slope-Assisted BOTDA (SA-BOTDA). Bernini et al. made dynamic strain measurements over a 30 m long fibre [30]. This was achieved by introducing a preliminary Brillouin frequency scan of the fibre to understand the frequency shift behaviour along the entirety of the sensing fibre. After this slow mapping phase, a fast phase was executed. During tests, the frequency difference between the probe and the continuous-wave pump are fixed such that the Brillouin gain spectrum has its quadrature point at the Brillouin frequency shift of the fibre. As such, changes in the Brillouin frequency shift lead to changes in the optical signal recorded at the photodetector. The variation in optical power is due to the Brillouin gain spectrum acting as a frequency filter. Via this approach, dynamic strains could be measured as the short length of fibre allowed a high interrogation rate. Bernini et al. measured vibrations over a 200 Hz bandwidth, with a strain range of $95 \mu\epsilon$ and a spatial resolution of 3 m. One drawback to this approach is that if a Brillouin frequency shift occurs greater than half the linewidth of the gain spectrum, it cannot be detected by the system.

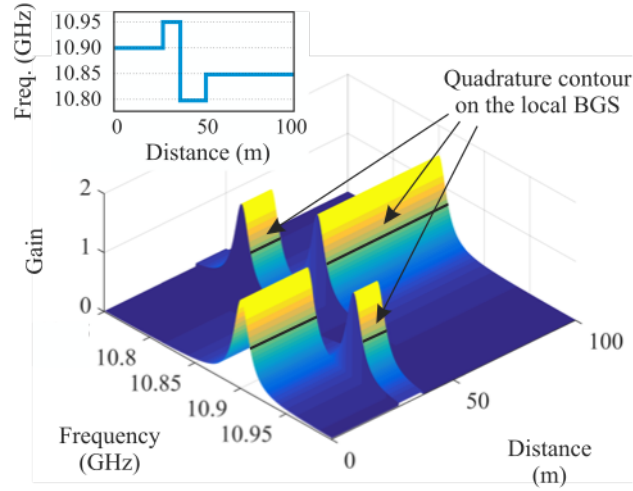


Figure 4.8: A 3D plot of an exemplar Brillouin gain spectrum mapped along a 100 m sensing fibre as a function of Brillouin frequency shift. The quadrature point at the slope of the local gain spectra have been labelled. In the top left, the insert shows the values of the quadrature points over the distance of the fibre [18].

Peled et al. showed after the initial mapping of the Brillouin frequency shift of the fibre, if a fast interrogation is applied, a larger bandwidth can be achieved with SABOTDA [31]. During this fast phase, rather than sitting with its quadrature point of Brillouin frequency shift of the fibre, the frequency difference between pump and probe are locked such that the quadrature point is at the slope of the Brillouin gain spectrum (Fig. 4.8.) Utilising this methodology, dynamic strains of frequency 400 Hz and a range of $600 \mu\epsilon$ were measured over an 85 m long fibre.

More recently a spatial resolution of 1 m and an effective sampling rate of approximately 2 kHz was achieved, along a 160 m fibre by Urricelqui et al. [32]. In this methodology, dynamic strain was detected via the changes in phase of the Brillouin backscattered light and hence, is known as Brillouin Phase Shifted OTDA (BPS-OTDA). The probe wave is phased modulated such that two side bands are created. The phase-modulation frequency is maintained in a manner whereby the pump signal only mixes with the probe signal's upper side-band. The phase of side band is dependent on the frequency shift, not the Brillouin gain spectrum. Dynamic strain measurements are evaluated from the phase of the upper side-band in conjunction with the modulation frequency and amplitude. From this, using a sampling rate of 1.6 kHz, a 160 m long fibre was interrogated with a resolution of 1 m.

BOTDA offers great benefit when single event detection along the fibre is adequate. However, there are several disadvantages of BOTDA sensing systems. First is the balance between frequency and sensing range. BOTDA is a relatively slow process due to the scanning of the entire length of sensing fibre at numerous frequency intervals. Therefore, the sensing frequency is of the order of tens of Hertz. Practically, the sensing fibre must be accessed from both ends, restricting single-access applications. Furthermore, only large strains can be sensed. If the magnitude of strain does not correspond to a frequency shift greater than the Brillouin linewidth of the unstrained fibre, the Brillouin gain spectrum at a point of interest, is affected by the strain distribution along the fibre. It has been reported that this is due to transfer of power between

the counter propagating waves from the front face of the fibre to the measurement point [33]. Finally, slow but continuous variation in temperature and strain of the sensing fibre can alter the Brillouin gain spectrum and subsequently, for SA-BOTDA, the quadrature point on the gain spectrum. Thus continued recalibration of the gain spectrum is required for SA-BOTDA and BPS-OTDA.

4.4.3 Optical Correlation Domain Analysis

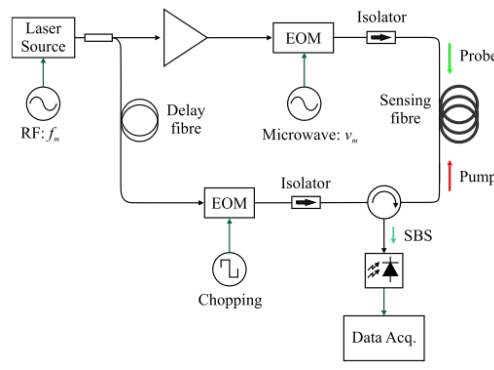


Figure 4.9: A schematic of a typical Brillouin optical correlation domain analysis set up [18].

Brillouin Optical Correlation Domain Analysis (BOCDA) utilises two counter propagating continuous waves whose wavelengths are being modulated. At a single point along the fibre, Brillouin scattering occurs. The point at which the scattering occurs can be altered in two ways: via either the frequency difference between the two sources or via the wavelength modulation frequency (Fig. 4.9.) Hence, by controlling the correlation between the two continuous sources, the strain and temperature along an optical fibre can be determined [34].

One of the first BOCDA studies measuring dynamic strain by Hotate et al. used a high frequency sweep rate to attain high spatial resolution sensor. The system was capable of recording dynamic strains of $3 \mu\epsilon$. However, the sensing range was limited to ~ 3 m due to the high frequency sweeping rate. The technique was further enhanced by Song et al., achieving a sampling rate of 20 Hz and accuracy in strain measurements of $50 \mu\epsilon$ over a distance of 100 m [35]. However, the technique is disadvantaged as it is time consuming. In addition, BOCDA distributed vibration sensors are limited by the trade off between sensing range and spatial resolution; the sensing range is typically ~ 200 times the resolution. Thus, the system is not ideal for measuring dynamic strain.

4.5 Enhanced Signal Fibres

Over the past decade, the distributed acoustic sensing (DAS) industry built systems based upon single mode telecommunication fibres as the sensing element. Mass production of germanium-doped silica fibres for data transfer has driven their price down to 11 pence per meter, making them financially attractive to interrogator manufacturers and end users. These single mode fibres typically have an attenuation of less than 0.2 dB per km, so that large amounts of data can be sent over vast distances without the need of introducing repeaters.

The attenuation for telecommunications is the asset for Rayleigh-based sensing systems. Inhomogeneities frozen in the fibre during its fabrication cause scattering. As outlined in the previous section, DAS systems exploit this isotropic Rayleigh back scatter to make dynamic strain measurements. Rayleigh scattering is the favoured mechanism as it takes place in all waveguides, occurs at all wavelengths, is continuous along the length of the fibre and the waveguides require no additional processing.

The problem that these systems face is their extremely-poor signal to noise ratio. Typical scattering causes a ~ 70 dB signal from the front end of the optical fibre; only worsening with distance. The same mechanism allowing DAS systems to make measurements is also responsible for the signal attenuation. The Rayleigh scattering coefficient is derived by performing a solid angle integration over the Rayleigh scattering Eq. $R(\lambda, \theta, h)$:

$$\gamma_s = \int_0^{2\pi} \int_0^\pi R(\lambda, \theta, h) \sin \theta \, d\theta \, d\phi \quad (4.12)$$

Eq.4.12 shows how Rayleigh scattering is indiscriminate in direction. Hence, in sensing applications, the inhomogeneities reflecting light back to the detector also cause scattering in all other directions, equally. Only light scattered below the critical angle of the fibre is collected by the detector, as described by Eq. 4.8. Thus, for a standard single mode telecommunication fibre, only $\sim 10^{-3}$ of the scattered light is captured to make a measurement. As such, research efforts to improve the signal to noise ratio can be classified in two categories: those modifying the infrastructure and data processing of interrogator units [36, 37, 38, 39]; or by modifying the optical fibre sensor itself [40, 41, 42, 43, 44]. Given the focal point of this research is upon novel sensing elements, the second category of solutions is covered.

One solution would be to improve as the numerical aperture of the fibre by increasing with concentration of dopants. Thus, this would lead to a rise in the capture fraction, as described in Eq.4.8. However, as Eq.4.12 shows, attenuation is proportional to the signal to noise ratio. It has been shown that increasing the core NA from 0.13 to 0.21 increased backscattering by 3 dB but increased attenuation from 0.3 to 1 dB per km [41].

Thus, there has been a pursuit of a sensing element solution that could enhance the signal to noise ratio whilst preserving both the low attenuation of single mode telecommunication fibres and their low cost per meter. The following two sections in this chapter provide a review of solutions to enhance the signal to noise ratio for distributed Rayleigh based sensing systems.

4.5.1 Fibre Bragg Grating Solutions

Fibre Bragg gratings have been employed for decades to reflect forward propagating light for sensing purposes[45, 46, 47]. Thus, when looking to enhance the signal to noise ratio for distributed Rayleigh based sensing systems, utilising grating technology seems suitable.

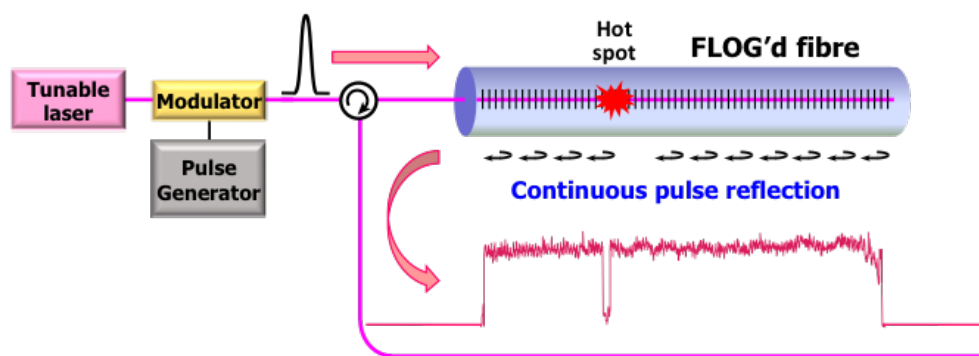


Figure 4.10: A schematic of a FLOG distributed fibre sensor. The basic elements are a frequency tunable laser source, pulse shaping modulator and a circulator. The diagram shows how if a strain or temperature change occurs along the FLOG, a drop in signal will be observed in the back-reflected trace [48].

In a theoretical paper, Thevanez et al highlighted this possibility of using grating technology for distributed acoustic and temperature sensing, with the concept of a Faint Long Grating (FLOG) [48]. The hypothesised concept would combine the advantages of both Rayleigh and Brillouin systems providing: no energy to generate the spectrally dependent reflection; a sensitivity to changes in refractive index; no additional attenuation of the forward propagating pump light; and the ability to make absolute measurements. Physically, a FLOG is an ultra-weak Bragg grating printed upon the entire length of an optical fibre. To interrogate a FLOG a tunable laser, modulator and pulse generator are required (Fig. 4.10.) The arrangement is similar to that of BOTDA and coherent Rayleigh OTDR systems.

For this to be possible, a consistent phase relation between planes is essential, with a refractive index contrast of magnitude small enough to maintain a low reflectivity. If utilised in an OTDR based manner, the effective length of the grating can be considered as the portion of the fibre covered by the probe pulse. Thus, the spatial resolution of the OTDR measurement is the effective grating length at any time. Using the Fourier transform limits of the probe pulse, limitations of reflectivity being greater than the fluctuations due to inhomogeneities but low enough not to cause significant pulse depletion, it was hypothesised that a 100 km grating would have a 33 dB enhancement over the natural Rayleigh backscatter. This is based upon the grating having a linear reflectivity of 10^{-5} [48]. This translates into a grating refractive index contrast smaller than the random fluctuations in refractive index deriving from the fibre's fabrication. This is extremely challenging. In this work, experimental attempts were made to produce a FLOG, but only a 10 cm long grating could be generated with a reflectivity of 35 %; far too high to realise the concept of FLOGs.

Fabricating Bragg gratings greater than 10 cm long has posed a tremendous engineering challenge for many years. Kashyap's group have been leaders in this field for two

decades proposing several methods to fabricate gratings over 10 cm long [49, 50, 51]. In 1995, Kashyap et al produced a 1.3 m long chirped by using a phase mask to fabricate many gratings and subsequently, stitching them together [49]. The grating had a bandwidth of 10 nm and a reflectivity of 30 dB, but the stitching process was far from ideal.

Shortly after publication, a number of techniques were reported to remove the dependency of the phase mask and to allow the fabrication of arbitrary grating profiles [52, 42, 43, 44]. These UV writing based methodologies focussed upon translating a phase mask relative to optical fibres such to alter an interferometric pattern, and hence the Bragg wavelength over the length of the fibre. Bragg gratings with 20 dB reflectivity were successfully fabricated but the resultant reflection spectra were relatively poor.

Loranger and Kashyap highlighted that the problem with fabricating ultra long fibre Bragg gratings is due to the varying refractive index along the length of fibre [53]. Even the highest quality telecommunication fibre shows refractive index fluctuations 1×10^{-5} over 3 cm. The Bragg equation is dependent on the effective index of the mode propagating through fibre. Thus, without accommodating for the variations in the refractive index over the grating length, phase errors will occur that deteriorate with length. Their work measured the refractive index variation along 80 centimetres of fibre to a precision of 3×10^{-6} refractive index units. This is achieved by writing a weak probe grating over the 1 m region of interest. Then using a commercial OFDR system, the weak grating was scanned and, the Bragg wavelength variation along the length of the region of interest is measured as a function of position.

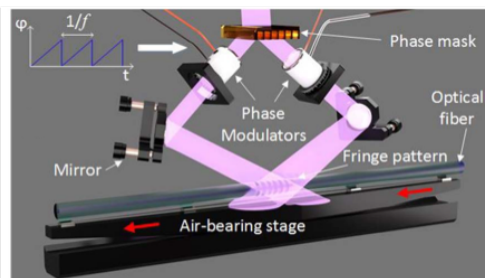


Figure 4.11: A schematic of a Talbot interferometer fibre Bragg grating writing set up. The system is a continuous direct writing methodology, interfering the diffractive orders from a phase mask to create a fringe pattern within the optical fibre. The fibre moves at velocity v , whilst the interference pattern is moved using a phase modulator. The modulator is driven by a saw-tooth function of frequency f . [51].

Using this mapping tool, Loranger and Kashyap showed how near perfect 1 meter long gratings could be fabricated by phase correcting for these index variations [51]. First, three weak probe gratings, 1 nm apart from one another spectrally and outside the target Bragg wavelength, are written into the fibre using a Talbot interferometer writing set up (Fig. 4.11.) Using OFDR, the frequency shift along the fibre is mapped for each of the 3 gratings. Using an average of the phase derivative profiles, a correction profile based upon UV writing power and writing speed can be created. This technique of mapping and phase correcting is extremely effective but subsequently time consuming. Furthermore, all gratings here were fabricated with reflectivity strengths over 20 dB; thus, not suitable for creating a FLOG-like solution. The other limitation of this technique was the restriction of grating length to the mechanical range of the air bearing stage.

To overcome the phase error challenge when fabricating a continuous fibre grating, an intermediate solution has been developed - ultra weak Bragg grating arrays [54, 55, 56, 57]. This solution involves writing relatively weak Bragg gratings at discrete intervals along the length of the fibre. In most cases UV fabrication methods are used meaning the coating either has to be stripped and re-coated (Fig. 4.12), or gratings have to be produced during fibre fabrication on the draw tower, before the coatings are applied [58, 59, 60, 61, 62]. These UV based set ups are extremely complicated and are a significant engineering feat. During fibre fabrication, a UV laser and phase mask must be precisely aligned to a fibre being drawn from a furnace. It becomes very difficult to adjust to any errors occurring in real-time and spectral deviations are common.

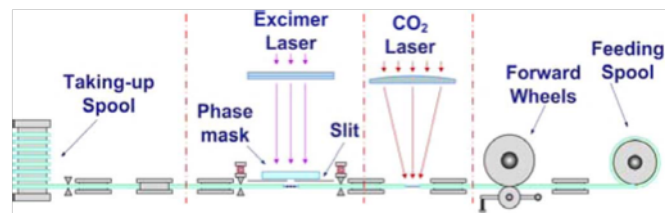


Figure 4.12: A schematic of a UV-based weak FBG array fabrication set up. For post processing, automated stripping and re-coating of the optical coating is required. The stripping is performed with a CO_2 laser. It is integral this is done with high precision as not to leave any particulates on the surface of the fibre as this could be detrimental to the quality of grating [60].

Ultra weak grating arrays have been demonstrated in conjunction with a ϕ -OTDR system to measure dynamic strain after 5 km of standard sensing fibre [56]. Using an imbalanced Mach-Zehnder interferometer The array was able to measure strains up to $6.2 \text{ } \mu\text{e}$ with a 2 meter spatial resolution. Grating arrays are commercially available but have limitations. When measurements have been made in a lab environment, vibrations were imparted in-between gratings [56, 63]. This is due to the need for spectral matching if an interferometric approach is used. If a strain was imparted directly on the grating, the Bragg wavelength would shift, translating into a measurement error in phase. Furthermore, ensuring spectral matching during fabrication can also be tricky given the impact of varying environmental factors on the Bragg wavelength. Furthermore, controlling the loss of these gratings is extremely difficult as they are written typically, with a single laser shot. This limits their length for distributed acoustic sensing applications. These arrays are also subject to two types of cross-talk, disrupting their signal: spectral shadowing causing distortion of downstream gratings by upstream ones; and multiple-reflection crosstalk where a false signal undergoing numerous reflections between upstream gratings arrives at the detector at the same time as the signal arriving from downstream gratings [60]. This has to be corrected for using data signal processing techniques.

In 2017, Westbrook et al. demonstrated the first continuous 1 km long grating [41]. The grating was fabricated using a phase mask and continuous UV-based reel to reel inscription system (Fig. 4.13.) The phase mask profile created a 15 mm long chirped grating spanning 10 nm. These were spatially overlapped with a 5 mm spacing to generate a continuous scatter signal over an arbitrary length. A UV-transparent coated single mode fibre was used to avoid the need to strip the coating. The fibre demonstrated an enhancement of 10 dB above the natural occurring Rayleigh scattering across a 10 nm bandwidth. The loss of the fibre after inscription was 0.4 dB per km, meaning processing had only induced a 0.1 dB per km loss. These results were the first

demonstration of the concept of FLOGs. However, the fibre coating had to be treated prior to inscription to enable UV inscription through the coating.

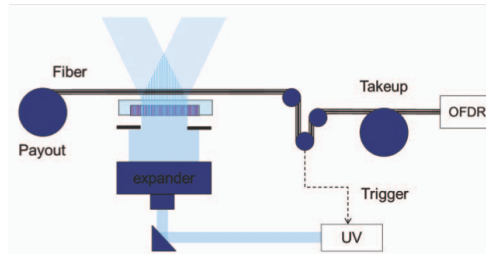


Figure 4.13: A schematic of a UV-phase mask, continuous grating inscription set up. A reel-to-reel methodology is used to print overlapping, chirped gratings to cover a 10 nm bandwidth [41].

Later in 2018, Handerek et al. demonstrated an improvement upon this with a 16 dB enhancement above the natural Rayleigh backscatter, whilst maintaining a 0.4 dB per kilometre attenuation [40]. The fibre's enhancement was demonstrated both 1 km and 41 km range, after 40 km of G.652 standard fibre. At 41 km a 33.4 dB increase in sensitivity was recorded. The fabrication of the continuous grating fibre was not disclosed, but is presumed to be similar to that reported by Westbrook et al. The same fibre was later demonstrated in a distributed acoustic measurement at 117 km without the use of inline amplification [64]. 100 km of ultra-low loss fibre (~ 0.15 dB per km attenuation) was combined with 16 km of standard single mode fibre and 1 km of the continuous grating fibre. A loud speaker was driven at 100 Hz and detected with a spatial resolution of 10 m at an interrogation frequency of 1 kHz. The measurement detected a loud acoustic event, defined as 6 dB above the average self noise level. For weaker events, such as footsteps for a deeply buried fibre would require lower self-noise levels. This was an extremely powerful measurement, demonstrating the advantages of an enhanced backscatter fibre in pushing the limits of distributed acoustic sensing measurements.

4.5.2 Inscribed Scattering Centres

Another approach to improving the signal to noise ratio in sensing applications has focussed upon processing optical fibres with a laser such to enhance its scattering properties. A UV-based approach has been proposed by Loranger et al [65]. In their work, an off-the shelf single mode telecommunication fibre with a low germanium doped core, was irradiated with a UV beam. The irradiation has been shown to create a high density of defects that cause scattering [66]. In hydrogen loaded fibres, absorption of UV in high concentration germanium fibres causes the formation of colour centres [67]. However, the exact cause to the enhanced Rayleigh scattering is not known. Loranger et al. concluded the colour centres formed were responsible for scattering due to their associated refractive index increase. When evaluated using a commercial OFDR machine, a ten-fold signal enhancement was measured. The limitation to this technique is that scattering is enhanced in all directions. Hence, this methodology is not suitable for long distance sensing applications.

All fore-mentioned techniques have focussed upon using UV laser writing techniques, exploiting the photosensitive nature of optical fibres to enhance the signal to noise ratio.

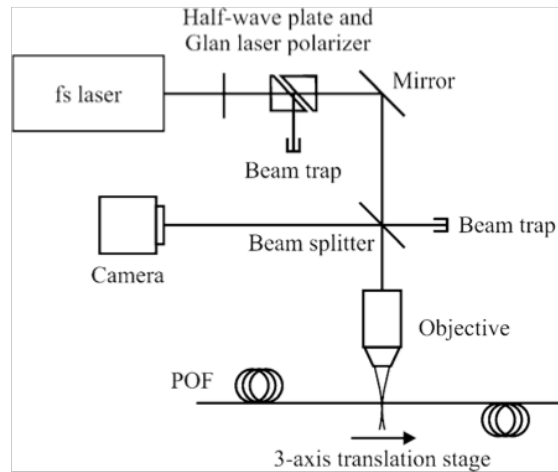


Figure 4.14: A schematic of the experimental set up to fabricate femtosecond voids in polymer optical fibres [68].

In 2013, Liehr et al demonstrated how femtosecond laser writing techniques could offer new solutions to this problem [69, 68, 70]. Liehr et al. first demonstrated the power of femtosecond writing in restructuring polymer optical fibres for shape and temperature sensing applications [69, 68]. A similar set up to that used to fabricate fibre Bragg gratings was used (Fig. 4.14.)

By exceeding the damage threshold, void structures were inscribed in a large core PMMA optical fibre causing enhancements of up to 3 dB compared to unmodified regions in the fibre. Fig. 4.15 shows 3 structures, each inscribed with a single $5 \mu\text{J}$ pulse in GK-40 fibre at $100 \mu\text{m}$, $200 \mu\text{m}$ and $300 \mu\text{m}$ focal depths. Cavities of dimension greater than $1 \mu\text{m}$ were thought to form in the direction along the fibre axis. This means a combination of Mie scattering and Fresnel reflection between the void and PMMA core, are thought to be the mechanisms responsible for the enhanced signal.

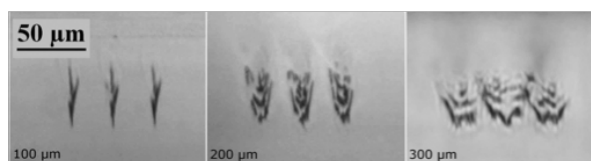


Figure 4.15: Microscope images of femtosecond modifications in GK-40 fibre at focal depths of $100 \mu\text{m}$, $200 \mu\text{m}$ and $300 \mu\text{m}$. Each structure was inscribed with a single $5 \mu\text{J}$ laser pulse focussed through a 0.6 NA lens [68].

Later Liehr et al. used this technique to fabricate enhanced scattering structures in commercial single mode telecommunication fibres [70]. Incoherent OTDR and incoherent OFDR measurements were performed on the fibre. One fibre contained 12 scattering centres, 1 m apart from another. Centres were inscribed by focussing an 800 nm laser pulse through a 0.6 NA lens. A single pulse of energy $0.4 \mu\text{J}$ was used to produce each void. Using incoherent OFDR, enhancements of 10 dB were observed compared to unmodified regions (Fig. 4.16). A second sample was produced with 4 scattering centres, separated by 3 m. These reflectors were created with a higher pulse energy of $5 \mu\text{J}$ and showed an enhancement of 15 dB above the Rayleigh backscatter level.

The second sample was used to measure dynamic strains at a repetition rate of 20 Hz. Length changes of 2.5 mm were detected. The strain sensitivity and range was not fully defined in this work. This work was limited as no performance comparison was offered in respect to standard single mode fibre to assess the true benefit of this technique.

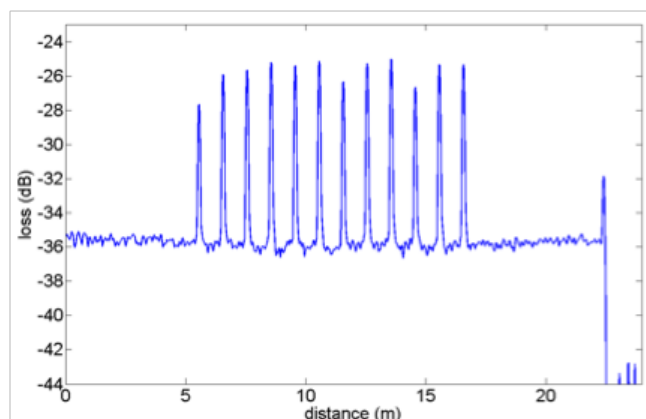


Figure 4.16: Incoherent-OFDR trace of the 12 scattering voids inscribed in the single mode fibre. [68].

Hicke et al. completed a more in-depth analysis whilst using femtosecond inscribed scattering dots in a simultaneous temperature gradient and vibration sensing measurement [71]. Similar to Liehr et al, scattering voids were inscribed using a single shot with a spot size less than $1 \mu\text{m}$. In a coherent-OTDR measurement, scatterers inscribed with 400 nJ pulse energy created enhancements of over 30 dB during an OFDR measurement. The paper also described how reflectivity of the scatterers is correlated with pulse energy and distance from the core. Lower energy pulses rendered lower signals. The further the void was from the centre of the core, the lower the signal recorded during the OFDR measurement.

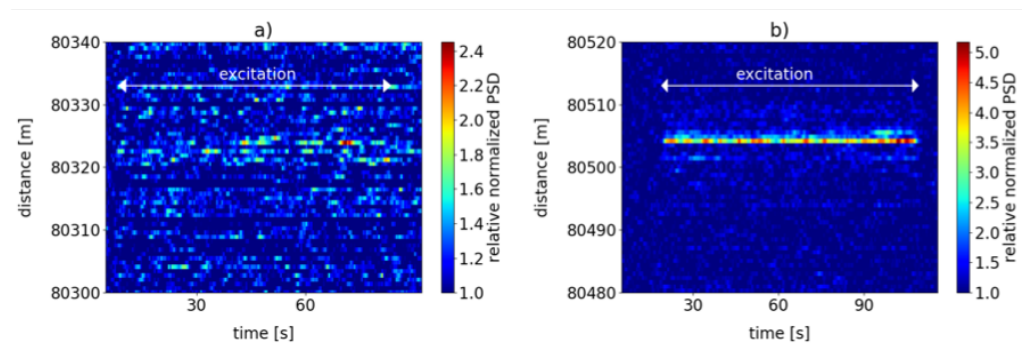


Figure 4.17: Normalised power spectral density at vibration frequency of 25 Hz at a distance of 80 km for: a) a standard single mode fibre and b) a modified single mode fibre with scattering voids inscribed [71]. The power spectral density has been normalised with respect to that from the Rayleigh backscatter.

Hicke et al. performed an extensive distributed vibration measurements on the enhanced fibre and offered comparisons in performance to standard single mode fibre. Standard single mode fibre can sense frequencies as low as 5 Hz. With the enhanced scatterers, frequencies as low as 0.6 Hz were detected. Furthermore, signal fading was mitigated

against due to the consistent power spectral density of the enhanced scattering points. This measurement was made detecting 80 Hz vibrations after 55 km of lead in fibre. Finally, to demonstrate the sensing range of the enhanced fibre, 25 Hz vibrations were measured at 80 km. Here, the lead in fibre comprised of 50 km of ultra low loss fibre and 30 km of standard single mode fibre. When using standard single mode fibre at these lengths, the signal was close to the noise level of the system. When using the scattering voids, the vibration was clearly identifiable (Fig. 4.17.) No quantitative improvement in performance when measuring the vibrations at 80 km was provided.

The work of Hicke et al. highlighted the power of the femtosecond scattering voids, however did not provide extensive analysis of its practicalities when scaled over large distances. Despite no attenuation effect being observed after less than 20 scatters, voids are susceptible to scattering in all directions. This was highlighted by Liehr et al when coupling red light into PMMA fibres and observing scattering under the microscope [68]. The observation questions the suitability of scattering voids for long distance, signal enhancement. Furthermore, controlling reflectivity of these scatterers can be difficult, as shown with distances as small as 4 micron causing over 10 dB in variation during OFDR measurements. Thus, high levels of engineering accuracy and precision are required for high quality, consistent reflectors to be fabricated.

4.6 Conclusions

In this chapter, the fundamental principles of Rayleigh and Brillouin scattering were introduced. After, a brief introduction into strain sensing systems based upon these two mechanisms were reviewed. For dynamic strain measurements, Rayleigh-based systems are of great commercial interest due to their ability to interrogate kilometres of sensing fibre in a single laser scan. Their limitations derive from their poor signal to noise ratio originating from the weak Rayleigh scattering. The second half of the chapter reviewed the most recent attempts to improve the signal of Rayleigh-based systems using novel sensing elements. The idea of using femtosecond micro-machined voids to enhance the signal was reviewed. The issue with this approach is the inability to control of the profile of the micro void. Hence, an opportunity to use the smooth refractive index regime to machine precise, low loss enhanced scattering reflectors was identified. The following chapter details the first experimental investigation into this concept.

Bibliography

- [1] Masoudi, A. Design and Application of a Distributed Optical Fibre Dynamic Strain Sensor. Ph.D. thesis, University of Southampton, 2015.
- [2] Krüger, S., Gessner, W., Eds. *Advanced Microsystems for Automotive Applications 2000*; Springer Berlin Heidelberg: Berlin, Heidelberg, 2000.
- [3] Alahbabi, M. N.; Cho, Y. T.; Newson, T. P. Long-range distributed temperature and strain optical fibre sensor based on the coherent detection of spontaneous Brillouin scattering with in-line Raman amplification. *Measurement Science and Technology* **2006**, *17*, 1082–1090.
- [4] Bolognini, G.; Hartog, A. Raman-based fibre sensors: Trends and applications. *Optical Fiber Technology* **2013**, *19*, 678–688.
- [5] Fabelinskii, I. L. *Molecular Scattering of Light*, 1st ed.; Springer US, 1968; p 662.
- [6] Schroeder, J.; Mohr, R.; Macedo, P. B.; Montrose, C. J. Rayleigh and Brillouin scattering in K₂O-SiO₂ glasses. *Journal of the American Ceramic Society* **1973**, *56*, 510–514.
- [7] Maughan, S. M.; Kee, H. H.; Newson, T. P. Simultaneous distributed fibre temperature and strain sensor using microwave coherent detection of spontaneous Brillouin backscatter. *Measurement Science and Technology* **2001**, *12*, 834.
- [8] Alahbabi, M. N.; Lawrence, N. P.; Cho, Y. T.; Newson, T. P. High spatial resolution microwave detection system for Brillouin-based distributed temperature and strain sensors. *Measurement Science and Technology* **2004**, *15*, 1539–1543.
- [9] Kobayakov, A.; Sauer, M.; Chowdhury, D. Stimulated Brillouin scattering in optical fibers. *Advances in Optics and Photonics* **2010**, *2*, 1.
- [10] Hartog, A.; Gold, M. On the theory of backscattering in single mode optical fibers. *Journal of Lightwave Technology* **1984**, *L*, 76–82.
- [11] Shatalin, S. V.; Treschikov, V. N.; Rogers, A. J. Interferometric optical time-domain reflectometry for distributed optical-fiber sensing. *Applied Optics* **1998**, *37*, 5600.
- [12] Dakin, J. P.; Lamb, C. A sensing method employing a fibre optic sensor system. 1990.
- [13] Alekseev, A. E.; Vdovenko, V. S.; Gorshkov, B. G.; Potapov, V. T.; Simikin, D. E. A phase-sensitive optical time-domain reflectometer with dual-pulse phase modulated probe signal. *Laser Physics* **2014**, *24*, 0–5.
- [14] Posey, R.; Johnson, G. A.; Vohra, S. T. Strain sensing based on coherent Rayleigh scattering in an optical fibre. *Electronics Letters* **2000**, *36*, 1688–1689.
- [15] Masoudi, A.; Belal, M.; Newson, T. P. A distributed optical fibre dynamic strain sensor based on phase-OTDR. *Measurement Science and Technology* **2013**, *24*.
- [16] Masoudi, A.; Belal, M.; Newson, T. P. Distributed optical fibre audible frequency sensor. *23rd International Conference on Optical Fibre Sensors* **2014**, *9157*, 91573T.

-
- [17] Farhadiroushan, M.; Parker, T. R.; Shatalin, S. Method and Apparatus for Optical Sensing. 2010.
- [18] Masoudi, A.; Newson, T. P. Contributed Review: Distributed optical fibre dynamic strain sensing. *Review of Scientific Instruments* **2016**, *87*.
- [19] Hartog, A.; Kader, K. Distributed Fiber Optic Sensor System With Improved Linearity. 2012.
- [20] Tu, G.; Zhang, X.; Zhang, Y.; Zhu, F.; Xia, L.; Nakarmi, B. The development of an Φ -OTDR system for quantitative vibration measurement. *IEEE Photonics Technology Letters* **2015**, *27*, 1349–1352.
- [21] Hartog, A.; Kotov, O.; Liokumovich, L. The Optics of Distributed Vibration Sensing. The materials of proceedings of the Second EAGE Workshop on Permanent Reservoir Monitoring. 2013; pp 2–5.
- [22] Eickhoff, W.; Ulrich, R. Optical frequency domain reflectometry in single mode fiber. *Applied Physics Letters* **1981**, *39*, 693.
- [23] Froggatt, M.; Moore, J. High-spatial-resolution distributed strain measurement in optical fiber with Rayleigh scatter. *Applied Optics* **1998**, *37*, 1735.
- [24] Zhou, D.-P.; Qin, Z.; Li, W.; Chen, L.; Bao, X. Distributed vibration sensing with time-resolved optical frequency-domain reflectometry. *Optics Express* **2012**, *20*, 13138.
- [25] Ding, Z.; Yao, X. S.; Liu, T.; Du, Y.; Liu, K.; Han, Q.; Meng, Z.; Chen, H. Long-range vibration sensor based on correlation analysis of optical frequency-domain reflectometry signals. *Optics Express* **2012**, *20*, 28319.
- [26] Wang, F.; Zhang, X.; Wang, X.; Chen, H. Distributed fiber strain and vibration sensor based on Brillouin optical time-domain reflectometry and polarization optical time-domain reflectometry. *Optics Letters* **2013**, *38*, 2437.
- [27] Horiguchi, T.; Shimizu, K.; Kurashima, T.; Tateda, M.; Koyamada, Y. Development of a distributed sensing technique using Brillouin scattering. *Journal of Lightwave Technology* **1995**, *13*, 1296–1302.
- [28] Kurashima, T.; Horiguchi, T.; Tateda, M. Distributed-temperature sensing using stimulated Brillouin scattering in optical silica fibers. *Optics Letters* **1990**, *15*, 1038.
- [29] Sibbett, W.; Lagatsky, A. A.; Brown, C. T. A. The development and application of femtosecond laser systems. *Optics Express* **2012**, *20*, 6989.
- [30] Bernini, R.; Minardo, A.; Zeni, L. Dynamic strain measurement in optical fibers by stimulated Brillouin scattering. *Optics Letters* **2009**, *34*, 2613–2615.
- [31] Peled, Y.; Motil, A.; Yaron, L.; Tur, M. Slope-assisted fast distributed sensing in optical fibers with arbitrary Brillouin profile. *Optics Express* **2011**, *19*, 19845.
- [32] Urricelqui, J.; Zornoza, A.; Sagues, M.; Loayssa, A. Dynamic BOTDA measurements based on Brillouin phase-shift and RF demodulation. *Optics Express* **2012**, *20*, 26942.
- [33] Geinitz, E.; Jetschke, S.; Röpke, U.; Schröter, S.; Willsch, R.; Bartelt, H. The influence of pulse amplification on distributed fibre-optic Brillouin sensing and a method to compensate for systematic errors. *Measurement Science and Technology* **1999**, *10*, 112–116.

-
- [34] Hotate, K.; Tanaka, M. Distributed fiber Brillouin strain sensing with 1-cm spatial resolution by correlation-based continuous-wave technique. *IEEE Photonics Technology Letters* **2002**, *14*, 179–181.
- [35] Song, K. Y.; Kishi, M.; He, Z.; Hotate, K. High-repetition-rate distributed Brillouin sensor based on optical correlation-domain analysis with differential frequency modulation. *Optics Letters* **2011**, *36*, 2062.
- [36] Cao, C.; Wang, F.; Pan, Y.; Zhang, X.; Chen, X.; Chen, Q.; Lu, J. Suppression of Signal Fading With Multi-Wavelength Laser in Polarization OTDR. *IEEE Photonics Technology Letters* **2017**, *29*, 1824–1827.
- [37] van Putten, L. D.; Masoudi, A.; Brambilla, G. 100-km-sensing-range single-ended distributed vibration sensor based on remotely pumped Erbium-doped fiber amplifier. *Optics Letters* **2019**, *44*, 5925.
- [38] Wang, C.; Wang, C.; Shang, Y.; Liu, X.; Peng, G. Distributed acoustic mapping based on interferometry of phase optical time-domain reflectometry. *Optics Communications* **2015**, *346*, 172–177.
- [39] Muanenda, Y.; Faralli, S.; Oton, C. J.; Di Pasquale, F. Dynamic phase extraction in a modulated double-pulse ϕ -OTDR sensor using a stable homodyne demodulation in direct detection. *Optics Express* **2018**, *26*, 687.
- [40] Handerek, V. A.; Karimi, M.; Nkansah, A.; Yau, A.; Westbrook, P. S.; Feder, K. S.; Ortiz, R. M.; Kremp, T.; Monberg, E. M.; Wu, H.; Simoff, D. A. Improved Optical Power Budget in Distributed Acoustic Sensing Using Enhanced Scattering Optical Fibre. **2018**, *26th International Conference on Optical Fiber Sensors*, TuC5.
- [41] Westbrook, P. S.; Feder, K. S.; Kremp, T.; Taunay, T. F.; Monberg, E.; Kelliher, J.; Ortiz, R.; Bradley, K.; Abedin, K. S.; Au, D.; Puc, G. Integrated optical fiber shape sensor modules based on twisted multicore fiber grating arrays. *Optical Fibers and Sensors for Medical Diagnostics and Treatment Applications XIV* **2014**, 8938, 89380H.
- [42] Cole, M. J.; Loh, W. H.; Laming, R. I.; Zervas, M. N.; Barcelos, S. Moving fibre/phase mask-scanning beam technique for enhanced flexibility in producing fibre gratings with uniform phase mask. *Electronics Letters* **1995**, *31*, 1488–1490.
- [43] Petermann, I.; Sahlgren, B.; Helmfrid, S.; Friberg, A. T.; Fonjallaz, P.-Y. Fabrication of advanced fiber Bragg gratings by use of sequential writing with a continuous-wave ultraviolet laser source. *Applied Optics* **2002**, *41*, 1051.
- [44] Chung, K. M.; Dong, L.; Lu, C.; Tam, H. Y. Novel fiber Bragg grating fabrication system for long gratings with independent apodization and with local phase and wavelength control. *Optics express* **2011**, *19*, 12664–12672.
- [45] Hill, K. O. Aperiodic distributed-parameter waveguides for integrated optics. *Applied Optics* **1974**, *13*, 1853–1856.
- [46] Erdogan, T.; Sipe, J. Tilted fiber phase gratings. *Journal of the Optical Society of America a-Optics Image Science and Vision* **1996**, *13*, 296–313.
- [47] Canning, J. Photosensitization and photostabilization of laser-induced index changes in optical fibers. *Optical Fiber Technology* **2000**, *6*, 275–289.

-
- [48] Thévenaz, L.; Chin, S.; Sancho, J.; Sales, S. Novel technique for distributed fibre sensing based on faint long gratings (FLOGs). *23rd International Conference on Optical Fibre Sensors Proceedings of SPIE* **2014**, 9157, 91576W–1–4.
- [49] Kashyap, R.; Ellis, A.; Malyon, D.; Froeklich, H.-G.; Swanton, A.; Armes, D. I. 1.3m long super-step-chirped fibre Bragg grating with a continuous delay of 13.5ns and bandwidth 10nm for broadband dispersion compensation. *22nd European Conference on Optical Communication - ECOC'96, Oslo* **1996**, 7–10.
- [50] Kashyap, R.; Swanton, A.; Smith, R. P. Infinite length fibre gratings using circular amplitude and phase masks. **1999**, 35, BB3.
- [51] Loranger, S.; Lambin-Iezzi, V.; Kashyap, R. Reproducible ultra-long FBGs in phase corrected non-uniform fibers. *Optica* **2017**, 4, 1143.
- [52] Asseh, A.; Storøy, H.; Sahlgren, B. E.; Sandgren, S.; Stubbe, R. A. A writing technique for long fiber Bragg gratings with complex reflectivity profiles. *Journal of Lightwave Technology* **1997**, 15, 1419–1423.
- [53] Loranger, S.; Kashyap, R. Are optical fibers really uniform? Measurement of refractive index on a centimeter scale. *Optics Letters* **2017**, 42, 1832.
- [54] Wang, Y.; Gong, J.; Wang, D. Y.; Dong, B.; Bi, W.; Wang, A. A quasi-distributed sensing network with time-division-multiplexed fiber Bragg gratings. *IEEE Photonics Technology Letters* **2011**, 23, 70–72.
- [55] Wang, X.; Li, W.; Chen, L.; Bao, X. Thermal and mechanical properties of tapered single mode fiber measured by OFDR and its application for high-sensitivity force measurement. *Optics Express* **2012**, 20, 14779.
- [56] Zhu, F.; Zhang, Y.; Xia, L.; Wu, X.; Zhang, X. Improved Φ -OTDR sensing system for high-precision dynamic strain measurement based on ultra-weak fiber Bragg grating array. *Journal of Lightwave Technology* **2015**, 33, 4775–4780.
- [57] Zhang, X.; Sun, Z.; Shan, Y.; Li, Y.; Wang, F.; Zeng, J.; Zhang, Y. A High Performance Distributed Optical Fiber Sensor Based on Φ -OTDR for Dynamic Strain Measurement. *IEEE Photonics Journal* **2017**, 9, 1–12.
- [58] Askins, C. G.; Putnam, M. A.; Williams, G. M.; Friebele, E. J. Stepped-wavelength optical-fiber Bragg grating arrays fabricated in line on a draw tower. *Optics Letters* **1994**, 19, 147.
- [59] Lefebvre, P.; Vincelette, A.; Beaulieu, C.; Ficocelli, P. Automated manufacturing of fiber Bragg grating arrays. *Optics InfoBase Conference Papers* **2006**, 4–7.
- [60] Wang, Y.; Gong, J.; Dong, B.; Wang, D. Y.; Shillig, T. J.; Wang, A. A Large Serial Time-Division Multiplexed Fiber Bragg Grating Sensor Network. *Journal of Lightwave Technology* **2012**, 30, 2751–2756.
- [61] Bai, W.; Yu, H.; Jiang, D.; Yang, M. All Fiber Grating (AFG): a new platform for fiber optic sensing technologies. *24th International Conference on Optical Fibre Sensors* **2015**, 9634, 96342A.
- [62] Guo, H.; Liu, F.; Yuan, Y.; Yu, H.; Yang, M. Ultra-weak FBG and its refractive index distribution in the drawing optical fiber. *Optics Express* **2015**, 23, 4829.

-
- [63] Muanenda, Y.; Faralli, S.; Oton, C. J.; Cheng, C.; Yang, M.; Di Pasquale, F. Dynamic phase extraction in high-SNR DAS based on UWFBGs without phase unwrapping using scalable homodyne demodulation in direct detection. *Optics Express* **2019**, *27*, 10644.
- [64] Cedilnik, G.; Lees, G.; Schmidt, P. E.; Herstrom, S.; Geisler, T. Pushing the Reach of Fiber Distributed Acoustic Sensing to 125 km Without the Use of Amplification. *IEEE Sensors Letters* **2019**, *3*, 1–4.
- [65] Loranger, S.; Gagné, M.; Lambin-Iezzi, V.; Kashyap, R. Rayleigh scatter based order of magnitude increase in distributed temperature and strain sensing by simple UV exposure of optical fibre. *Scientific Reports* **2015**, *5*, 1–7.
- [66] Johlen, D.; Knappe, F.; Renner, H.; Brinkmeyer, E. UV-induced absorption, scattering and transition losses in UV side-written fibers. OFC/IOOC 1999 - Optical Fiber Communication Conference and the International Conference on Integrated Optics and Optical Fiber Communication. 1999; pp 50–52.
- [67] Poumellec, B. About writing mechanism of UV induced refractive index change in H₂ loaded Ge doped SiO₂. **2003**,
- [68] Liehr, S.; Burgmeier, J.; Krebber, K.; Schade, W. Femtosecond laser structuring of polymer optical fibers for backscatter sensing. *Journal of Lightwave Technology* **2013**, *31*, 1418–1425.
- [69] Liehr, S.; Burgmeier, J.; Krebber, K.; Schade, W. Fiber optic bend and temperature sensing in femtosecond laser-structured POF. *OFS2012 22nd International Conference on Optical Fiber Sensors* **2012**, *8421*, 84213I–84213I–4.
- [70] Liehr, S.; Burgmeier, J. Quasi-distributed measurement on femtosecond laser-induced scattering voids using incoherent OFDR and OTDR. *Fifth European Workshop on Optical Fibre Sensors* **2013**, 87943N.
- [71] Hicke, K.; Eisermann, R.; Chruscicki, S. Enhanced distributed fiber optic vibration sensing and simultaneous temperature gradient sensing using traditional C-OTDR and structured fiber with scattering dots. *Sensors (Switzerland)* **2019**, *19*, 9–11.

Chapter 5

Ultra-Low loss Enhanced Signal Fibre

5.1 Introduction

Predominantly, commercial coherent Rayleigh based distributed vibration sensing systems utilise single mode telecommunication fibres as the sensing element. They're favoured due to their low cost per meter and relative adequacy to make measurements. Measurements are made utilising the backscatter caused by the refractive index fluctuations frozen in the fibre during its fabrication. These systems are notorious for their poor signal to noise ratio. In the previous chapter, an in depth review of Rayleigh scattering and the problems faced by coherent-Rayleigh distributed vibration sensing systems was covered. A range of solutions based upon grating technology have been presented but are limited due to their fabrication complexity and attenuation [1, 2, 3, 4, 5, 6, 7, 8]. These novel solutions are critically reviewed in the previous chapter.

The introduction of enhanced scattering regions using UV writing and femtosecond micro-machining techniques has gained momentum recently. Loranger et al demonstrated UV written regions but significant attenuation was induced to the fibre, removing its practicality for long distance sensing [9]. Liehr et al. first proposed the use of femtosecond scattering voids to enhance the signal to noise ratio in polymer fibres [10, 11]. Later, this was demonstrated in single mode fibres and exploited for a distributed vibration sensing measurement [12, 13]. The problem with using scattering voids is the inability to control their shape due to the explosive nature during formation. Furthermore, the void scatters light in all directions as demonstrated when a fault finder is passed through the fibre.

In this chapter, rather than using void structures, we propose inducing smooth refractive index changes within standard single mode optical fibre. Using lower fluences of laser radiation, smooth, controlled structures can be drawn into the core of the fibre [14]. Using this writing regime, precise planes could be written providing a significant signal enhancement, whilst minimising the light scattered out of the fibre. The following section contains the principle behind femtosecond scattering regions and the theory behind their improved performance in the context of ϕ -OTDR measurements. After,

details of the initial experiments proving this concept are outlined.

5.2 Principle of Femtosecond Scatterers

Previously, femtosecond void scatterers have been demonstrated as a promising solution to the issues faced by Rayleigh-based sensing systems [12, 13]. Their attractiveness is due to their simple fabrication and extremely effective results. Utilising femtosecond scatterers possess all the benefits of the femtosecond PbP FBG technique: it does not require precise alignment of beams that is necessary for interferometric fabrication approaches, nor an intricate, electron-beam machined phase mask; inscription can be performed post fibre fabrication, through the coating; and non-photosensitive fibres can be machined without the need for prior treatment. Furthermore, scattering regions provided added benefits over FBGs. FBG arrays can be extremely complex to fabricate as spectral consistency is required for them to operate effectively in an interferometric-based sensing system [8, 15]. In contrast to FBGs, femtosecond inscribed scatterers function as broadband reflectors. This is because the enhanced signal is caused by a Fresnel reflection from the induced refractive index change. Femtosecond micro-machining offers a more effective route for achieving this index change due to the fundamental principles underpinning them; with UV writing, a smooth, graded index is induced meaning a stark refractive index contrast is not easy to fabricate. The lack of spectral dependence limits their use for temperature measurements - temperature can be measured by the spectral shift of the Bragg resonance wavelength. However, this limited dependence proves an asset for harsh-environment distributed sensing applications, where temperature fluctuations can affect dynamic strain measurements.

The effectiveness of femtosecond scatterers can be demonstrated theoretically by adapting the fundamental equations underpinning interferometric coherent-Rayleigh DAS systems. In OTDR measurements, a coherent probe pulse of is launched into a fibre and Rayleigh scattering attenuates the signal as it propagates. The Rayleigh scattering is caused by the inhomogeneities frozen in the fibre during its fabrication. The back-reflection caused by scatterers covered by the pulse at one time have a defined phase relation due to the coherent nature of the probe pulse. The interference of many waves from the distribution of scatterers within the pulse, leads to a speckle-like pattern forming when measured [16, 17, 18]. The phase differences between scatterers within a pulse are directly proportional to environmental parameters. This leads to fluctuations in the intensity in the time and spatial domain, respectively, causing a notorious signal fading issue [19, 20, 18]. The stochastic scatterer distribution leads to a non-linear transform function. Hence, the non-linearity means only relative signals can be detected; absolute measurements are not possible. The recorded intensity distribution is the sum of many backscatter signals from M stochastically distributed scattering centres located within half the spatial size of the interrogating pulse [17, 21]. The intensity distribution, as a function of distance along a single mode fibre, can be described mathematically as [16, 18, 22, 13]:

$$I(z) \propto I_0 \sum_{m=1}^M r_m^2 + 2 \sum_{i=1}^{M-1} \sum_{j=i+1}^M r_i r_j \cos(\phi_i - \phi_j) \quad (5.1)$$

where I_0 is the intensity of the input pulse; r_i and r_j are the reflectivities of scattering centres i and j , respectively; and $(\phi_i - \phi_j)$ is the phase difference between each pair of backscatter signals i and j respectively. The first term in eq. 5.1 relates to the incoherent

backscatter. As such it is not affected by external stimuli and can be ignored. The second term relates to the coherent backscatter. Its cosine behaviour, as a function of the phases which is dependent on external parameters, causes high non-linearity. If femtosecond

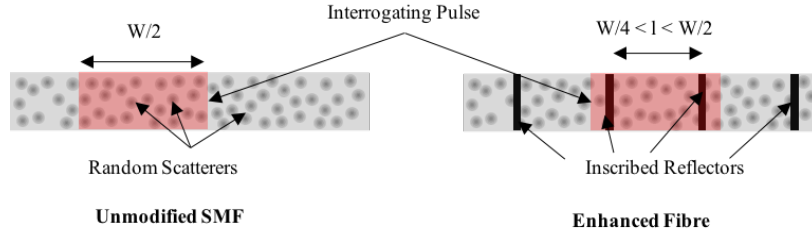


Figure 5.1: A schematic diagram of an interrogating pulse propagating through an unmodified fibre (left) and a fibre with inscribed femtosecond planes (right.) For the enhanced fibre, the spacing of reflecting planes is set to $W/4 < l < W/2$.

inscribed scatterers are introduced into the fibre, the intensity distribution is altered. Consider if the periodicity of reflectors is set to l , and is l is chosen to be greater than $W/4$ but less than $W/2$, where W is the length of the interrogating pulse in the spatial domain (Fig. 5.1) [23, 24, 15]. The two reflectors have phases ϕ'_1, ϕ'_2 , and reflectivities $r'_1, r'_2 \gg r_{i,j}$. The refractive index change induced by femtosecond micro-machining can be as large as $\sim 10^2$ compared to fluctuations of 10^{-5} from the inhomogeneities frozen in the fibre at conception. As the reflectivity of each inscribed scatterer is far greater than the naturally occurring scatterers, it overrides the transfer function. This is because the interference is dominated by the superposition of the backscatter waves from the two reflectors. Thus eq. 5.1 can be simplified to [24, 15, 25]:

$$I(z) \propto I_0((r'_1)^2 + (r'_2)^2) + 2I_0 r'_1 r'_2 \cos(\phi_1 - \phi_2) \quad (5.2)$$

Hence, it can be seen from Eq. 5.2 that the output at the detector is simplified to the superposition of two signals from the two reflectors. The optical path between the reflectors is extremely sensitive to environmental changes. Rather than many scatterers contributing to the interference pattern, the output has been simplified akin to a two beam interferometer following cosine behaviour when moving from one phase change to another. Eq. 5.2 shows far less dependence on thermal noise compared to 5.1. Thermal noise would alter the distribution of the scatterers in an unknown manner, translating into noise during dynamic strain measurements. With the reflectors, their distribution and reflectivities are more definitive, hence showing lower susceptibility to thermal noise. Furthermore, the definitive distribution of reflectors should allow a larger strain range. In unmodified single mode fibre, larger strains can alter the distribution of scatters with respect to the previous measurement. For dynamic strain measurements whereby constant scattering distributions are required to enable direct comparison of consecutive OTDR traces, changes in distribution translate into noise during the measurement. With the femtosecond enhanced fibre, the reflector distribution is fixed and therefore, should show a larger strain range.

5.3 Experimental methodology

5.3.1 Fabrication of Reflectors

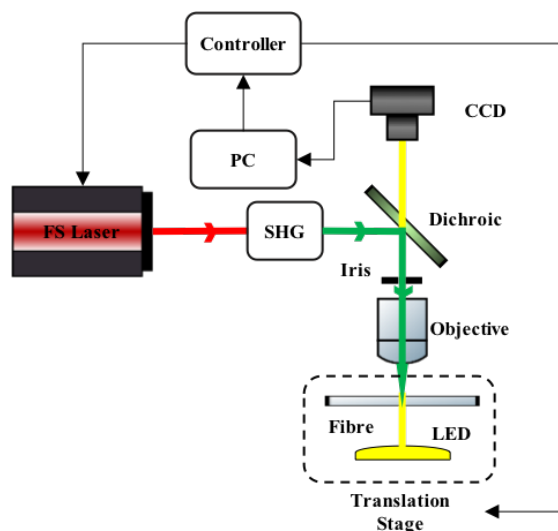


Figure 5.2: A schematic of the femtosecond writing set up used to inscribe the reflectors. *SHG* - second harmonic generation.

A typical femtosecond laser writing set up to fabricate Bragg gratings was used (Fig. 5.2.) A 1030 nm solid state Yb:KGW (ytterbium-doped potassium gadolinium tungstate) laser system (Pharos, Light Conversion Ltd) was used for fabrication. The beam was frequency doubled to 515 nm. The laser frequency was set to 1 kHz and each pulse had an energy of $4 \pm 0.1 \mu\text{J}$. A 0.4 NA objective lens was used in conjunction with an iris. At the focal point the beam had a depth of $9 \pm 1 \mu\text{m}$. To compensate for the spherical nature of the optical fibre, glycerol was used as an oil immersion liquid. A microscope cover slide was placed on top of the glycerol and optical fibre.

The reflectors were intended to be a rectangular structure of smooth refractive index that covered the entire core. To create this structure, the focal point of the laser was translated over a $25 \mu\text{m}$ depth. The width of each reflector was set to $62.5 \mu\text{m}$, half the diameter of the cladding. The fibre was manually unwound from a bobbin and placed under the microscope objective. Reflectors were intended to be placed 2 meters apart.

5.3.2 Optical time domain reflectometry

A simple OTDR set up was assembled (Fig.5.3). A 1550 nm distributed feedback laser diode was directly modulated using a pulse generator. The pulse generator modulated the laser to emit $1.0 \pm 0.1 \text{ ns}$ pulses, with a peak power of 1 mW every $10 \mu\text{s}$. Using an erbium-doped amplifier (EDFA), the signal was amplified by 30 dB to achieve a peak pulse power of 1 W. The enhanced reflector fibre was spliced onto the end of a 100 m spool of standard single mode telecommunications fibre (SMF-28e, Corning). The source and length of fibre was connected to a circulator. In the third port of the circulator an InGaAs photodetector (1811-FC, Newport) was connected to measure the

backscattered signal from the enhanced reflector fibre. An oscilloscope was connected to the photodetector to record the backscatter signal over time.

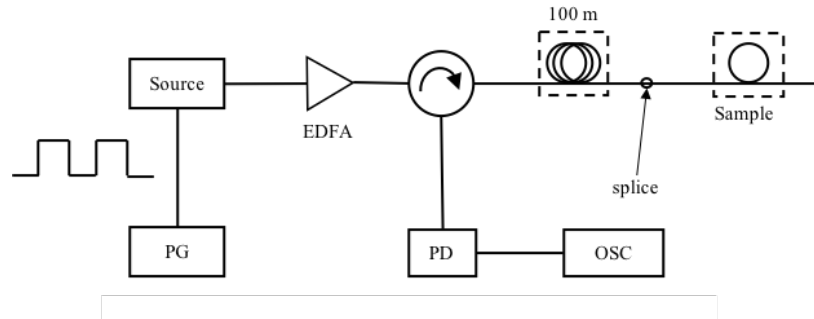


Figure 5.3: A schematic of the OTDR set up. *PG* - pulse generator; *PD* - photodetector; and *Osc* - oscilloscope.

5.3.3 Optical side scattering radiometry

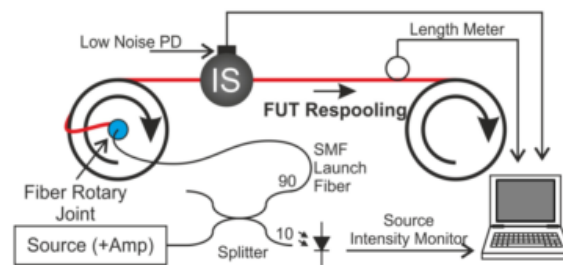


Figure 5.4: A schematic diagram of the OSSR arrangement [26]. *IS* - integrating sphere; *FUT* - fibre under test and *PD* - photodetector. The experiment was conducted with the assistance of Dr. Sandoghchi.

For a standard telecommunication fibre (SMF-28e, Corning) the attenuation is of the order of 0.2 dBkm^{-1} . As the enhanced reflector fibre has been altered in such a way to enhance the back scattered signal, the attenuation caused by the fabrication process must be assessed to determine its suitability. To measure the loss of these structures, optical side scattering radiometry (OSSR) was used. The technique offers a localised measurement of attenuation of an optical fibre that is more sensitive and accurate than its OFDR and OTDR counterparts [26].

A standard OSSR set up was used for the measurement (Fig.5.4.) A 1550 nm fibre laser (S1FC1550, Thorlabs) emitted a continuous 1 mW wave to interrogate the fibre under test. A 10 metre sample of the enhanced reflector fibre was wound onto a 1 m circumference fibre spool. The spool was placed onto one side of a fibre rewinding machine. During the measurement, the sample is wound onto a second spool using the rewinding machine. The sample traverses a 4-port, ~ 5 cm diameter integrating sphere with Spectralon coating (Newport calibrated IS, 819C-IG-2-CAL). The integrating sphere was secured onto the rewinding machine. The detector could handle powers of 100 nW - 2.5 W. The device was previously calibrated against other commercial low noise detectors. After calibration, the detector was sensitive to ~ 100 pW. The spatial

resolution of the measurement was ~ 5 cm, dictated by the diameter of the integrating sphere. The integrating sphere collects the scattered light from the fibre and measures it using a low noise detector.

The input and output ports from the detector were covered with 30 cm long black tubes to minimise the effect of background light on the measurement. A length meter attached the rewinding machine kept track of the amount of fibre that had been wound onto the new spool. Light from the fibre laser was coupled into the sample via a standard fibre connector at a bespoke fibre rotary joint. The joint allows the coupled region to rotate freely without obstructing the rewinding of the sample. To ensure fluctuations in the source power do not effect the attenuation measurement, a 90-10 coupler and off the shelf photodetector was used to monitor the output of the source. The system is managed by a PC which records the loss measurement against position of the fibre, as well as the fluctuations in source power.

5.4 Results and Discussion

5.4.1 Optical Time Domain Reflectometry

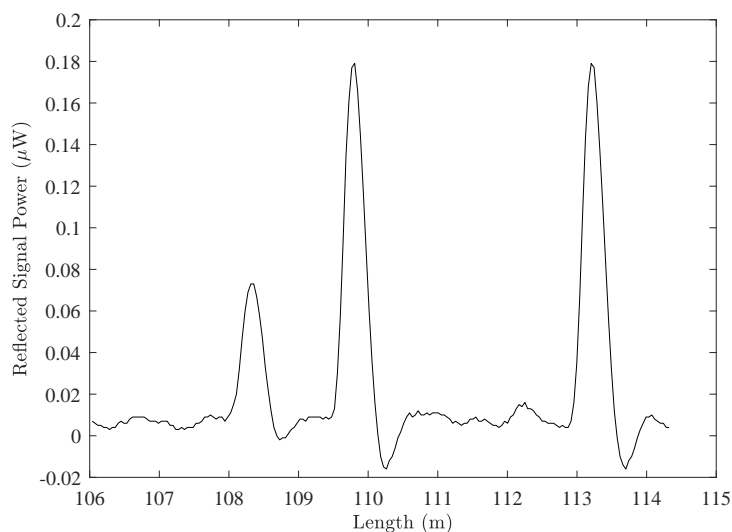


Figure 5.5: The captured OTDR power spectrum from the reflector fibre.

The main sample was designed to have four reflectors, but only three reflectors are visible in the recorded trace (Fig.5.5.) These caused increases in the back scattered signal of 73 ± 16 , 179 ± 16 and 179 ± 16 nW at positions of 108.31 ± 0.18 , 109.81 ± 0.17 and 113.20 ± 0.17 m along the fibre. Given a 1 W pulse was coupled into the sample, the 3 signals correspond to a reflectivity of 7.30×10^{-6} , 1.79×10^{-5} and 1.79×10^{-5} %. A fourth reflection was anticipated between 111 and 112 m but no increase in signal was measured. Based upon the structures causing a Fresnel back reflection, the change in refractive index of the second and third points is estimated to be on the order of $\sim 10^{-5}$. The first point was estimated to have a refractive index change on the order of $\sim 10^{-6}$.

Furthermore, the back reflected signal magnitude was achieved without the use of an amplifier on the return of the signal. Typically, a second EDFA is included in the OTDR set up, as the Rayleigh backscatter from the fibre inhomogeneities is extremely weak. Due to the accurate inscription of the reflectors, the enhanced reflector fibre does not require a second EDFA. The distance axis can be converted trivially into time using the speed of light. In the time domain, the full-width-at-half-maximum (FWHM) of each peak should correspond to the pulse length. The average FWHM was measured to be 1.14 ± 0.03 ns. The average FWHM result lies within one standard deviation of the input pulse duration. It can be seen that after the each peak a negative value of power was recorded. The fluctuation is due to the battery photodetector used. The voltage of the battery is independent of the voltage of the oscilloscope. A negative reading is registered when no light illuminates the detector as the current flows in the opposing direction.

5.4.2 Optical Side Scattering Radiometry

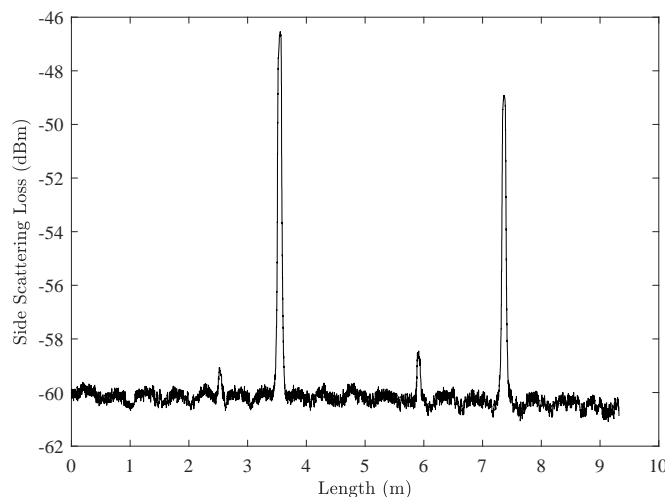


Figure 5.6: The recorded side scattered loss from the OSSR measurement for the enhanced reflector fibre.

The enhanced fibre reflector was pulled through the integrating sphere at a speed of 2 mm min^{-1} . Four reflectors were designed for this sample. The OSSR measurement revealed four increases in the side scattered loss, to levels significantly above the unmodified regions. The losses were measured to be -59.07 , -46.53 , -58.45 and -48.92 dBm at positions of 2.52, 3.56, 5.91 and 7.37 m, respectively. The unmodified regions of the fibre exhibited loss of -60 dBm, which was in-line with the fibre content data sheet corresponding to 0.2 dB km^{-1} . The largest side scattered loss originated from the second reflector located at 3.56 m and corresponds to a loss of $2.22 \times 10^{-3} \%$. If 1 of these points was placed every metre, the total fibre attenuation would become 0.30 dB km^{-1} . The source output power was stable to $<0.05 \text{ dB}$ throughout the measurement.

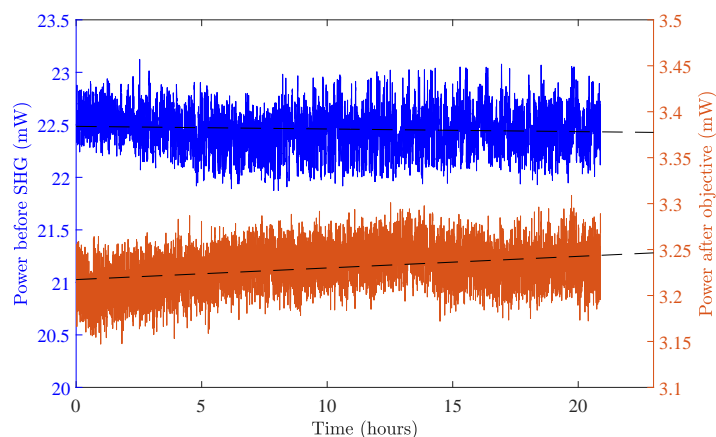


Figure 5.7: The recorded power of the femtosecond laser: after second harmonic generation (blue); and after the microscope objective (orange). Lines of best fit for each data set has been plotted (black).

5.4.3 Reflectivity Variation

Although the same parameters were used for the fabrication of all reflectors, differences in the magnitude of the backscattered signal were recorded. The first reflector is approximately 2.5 times weaker than the following two recorded reflections. Secondary investigations were conducted to establish the cause of this variation. First, the power of the femtosecond laser was monitored over two separate 22 hour periods. The purpose of this experiment was to ensure fluctuations in the laser power were not causing the variations in the reflectivity of inscribed structures. This was completed at two points along the beam propagation path: after the second harmonic generation crystal; and after the microscope objective. A photodiode (Thorlabs, S120 VC) was used to measure beam power. Power was recorded every second over the period (Fig. 5.7.) Lines of best fit have been plotted on the power trace in black. The measurement after the second harmonic generation crystal revealed consistency in power over 22 hours. The line of best fit showed a negligible change in power of $-2.5 \mu\text{W}$ per hour. The power recorded after the microscope objective showed a drift of $1.3 \mu\text{W}$ per hour. The first 14 hours showed a gradual increase, but after, the power stabilised. It is thought this was due to the laser reaching thermal equilibrium after first being switched on. This did not occur with the measurement after the second harmonic generator as the laser had been operating for a number of days before the measurement was made. The changes in power observed are not thought to be large enough to cause significant changes in the refractive index of the inscribed points; nor do the changes happen on the timescales that the variations in reflectivity of points were observed.

In addition to the femtosecond laser, investigations were conducted into the refractive index matching oil that was used. Tests were conducted to ensure the femtosecond laser radiation was not causing any changes to the optical properties of glycerol over time. To assess this, glycerol ($\geq 99.9\%$ purity) was placed on a cover slide, enough to cover it entirely. Then, the laser was focussed into the bulk of the cover slide, $100 \mu\text{m}$ below the surface. This is to replicate the conditions of when the laser is focussed into an optical fibre. Here, an optical fibre was not used as removing the fibre from the slide disturbs

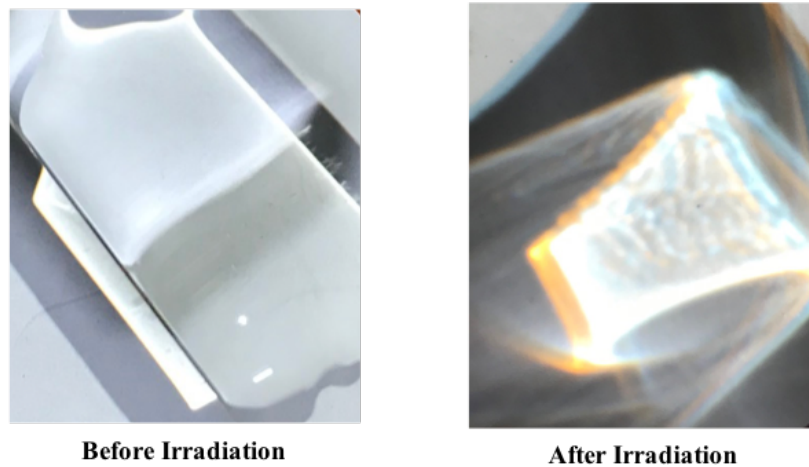


Figure 5.8: Photographs of glycerol: before irradiation (left) and after irradiation (right). A white LED was shone through the cover slide to highlight any optical changes.

the glycerol. Thus, if a fibre was used it could not be ensured that its removal would not affect the measurement. The laser was fired continuously for 5 minutes. The same laser settings for reflector inscription were used for this test. Before and after, a white LED was shone through the glycerol (Fig. 5.8.) It can be seen that before femtosecond laser radiation, the glycerol is optically transparent with the white light transmitting without disturbance. After 5 minutes of irradiation, when light is passed through the glycerol, a ripple effect was observed. These ripples show refractive index changes have been introduced into the glycerol. The refractive index changes have the potential to scatter light and subsequently, cause aberration effects when the femtosecond radiation is being focussed. Thus, these changes are thought to contribute to the reflector variation observed in the sample. It was also noted that when refractive index oil was placed over the fibre and the cover slide was placed on top, there was no control of the amount of glycerol between the slide and the fibre. Along with the absorption properties altering the glycerol, it was thought that the varying amount of oil may also be contributing to the variations in reflectivity.

5.5 Conclusions

The OTDR and OSSR results revealed the enhanced reflector fibre increased the signal to noise ratio 18 fold, whilst the fabrication process only increased the fibre attenuation by $\sim 2\%$ per kilometre (based upon the assumption a reflector was implemented every meter). Unlike other OTDR measurements, these results were achieved without the use of an amplifier on the backscattered signal. Extrapolating the results attained above to a 35 km sample (one reflector every meter), the signal from the furthest reflector would be 15 nW - 1.5 times greater than the noise level. Therefore, the 1 metre resolution can still be maintained without the need for averaging or an additional amplifier for the incoming signal. The result suggests commercial distributed fibre sensing systems could be simplified and improved if the enhanced reflector fibre can be fabricated for long distances (> 1 km). The removal of an EDFA could reduce the cost of a Rayleigh-based distributed fibre sensing system. Although to be implemented on a commercial scale,

improvements in the homogeneity of the reflectors must be made. The secondary tests showed the femtosecond laser was not contributing to these fluctuations.

To improve the consistency of the reflectivity enhancements, improvements to the experimental set up should be made. The glycerol had been found to contribute to the reflectivity variations due to changes in its optical properties over time. For future tests, a new refractive matching oil should be used. To ensure reflector inscription is not missed, the experimental arrangement should accommodate an OTDR feedback mechanism. This would allow for the monitoring of reflectivity in real time, allowing inconsistencies to be compensated for. Furthermore, as the optical fibre is extremely sensitive to changes in strain, the tension within the fibre should be controlled during inscription. This is also key for when winding the fibre back on; any inconsistencies in winding will lead to irregular strains exerted in the fibre, preventing direct comparison of previously inscribed reflectors.

Bibliography

- [1] Westbrook, P. S.; Feder, K. S.; Kremp, T.; Taunay, T. F.; Monberg, E.; Kelliher, J.; Ortiz, R.; Bradley, K.; Abedin, K. S.; Au, D.; Puc, G. Integrated optical fiber shape sensor modules based on twisted multicore fiber grating arrays. *Optical Fibers and Sensors for Medical Diagnostics and Treatment Applications XIV* **2014**, 8938, 89380H.
- [2] Handerek, V. A.; Karimi, M.; Nkansah, A.; Yau, A.; Westbrook, P. S.; Feder, K. S.; Ortiz, R. M.; Kremp, T.; Monberg, E. M.; Wu, H.; Simoff, D. A. Improved Optical Power Budget in Distributed Acoustic Sensing Using Enhanced Scattering Optical Fibre. **2018**, *26th International Conference on Optical Fiber Sensors*, TuC5.
- [3] Chung, K. M.; Dong, L.; Lu, C.; Tam, H. Y. Novel fiber Bragg grating fabrication system for long gratings with independent apodization and with local phase and wavelength control. *Optics express* **2011**, *19*, 12664–12672.
- [4] Askins, C. G.; Putnam, M. A.; Williams, G. M.; Friebele, E. J. Stepped-wavelength optical-fiber Bragg grating arrays fabricated in line on a draw tower. *Optics Letters* **1994**, *19*, 147.
- [5] Lefebvre, P.; Vincelette, A.; Beaulieu, C.; Ficocelli, P. Automated manufacturing of fiber Bragg grating arrays. *Optics InfoBase Conference Papers* **2006**, 4–7.
- [6] Wang, Y.; Gong, J.; Dong, B.; Wang, D. Y.; Shillig, T. J.; Wang, A. A Large Serial Time-Division Multiplexed Fiber Bragg Grating Sensor Network. *Journal of Lightwave Technology* **2012**, *30*, 2751–2756.
- [7] Bai, W.; Yu, H.; Jiang, D.; Yang, M. All Fiber Grating (AFG): a new platform for fiber optic sensing technologies. *24th International Conference on Optical Fibre Sensors* **2015**, 9634, 96342A.
- [8] Guo, H.; Liu, F.; Yuan, Y.; Yu, H.; Yang, M. Ultra-weak FBG and its refractive index distribution in the drawing optical fiber. *Optics Express* **2015**, *23*, 4829.
- [9] Loranger, S.; Gagné, M.; Lambin-Iezzi, V.; Kashyap, R. Rayleigh scatter based order of magnitude increase in distributed temperature and strain sensing by simple UV exposure of optical fibre. *Scientific Reports* **2015**, *5*, 1–7.
- [10] Liehr, S.; Burgmeier, J.; Krebber, K.; Schade, W. Fiber optic bend and temperature sensing in femtosecond laser-structured POF. *OFS2012 22nd International Conference on Optical Fiber Sensors* **2012**, 8421, 84213I–84213I–4.
- [11] Liehr, S.; Burgmeier, J.; Krebber, K.; Schade, W. Femtosecond laser structuring of polymer optical fibers for backscatter sensing. *Journal of Lightwave Technology* **2013**, *31*, 1418–1425.
- [12] Liehr, S.; Burgmeier, J. Quasi-distributed measurement on femtosecond laser-induced scattering voids using incoherent OFDR and OTDR. *Fifth European Workshop on Optical Fibre Sensors* **2013**, 87943N.
- [13] Hicke, K.; Eisermann, R.; Chruscicki, S. Enhanced distributed fiber optic vibration sensing and simultaneous temperature gradient sensing using traditional C-OTDR and structured fiber with scattering dots. *Sensors (Switzerland)* **2019**, *19*, 9–11.

-
- [14] Beresna, M.; Gecevicius, M.; Kazansky, P. G. Ultrafast laser direct writing and nanostructuring in transparent materials. *Advances in Optics and Photonics* **2014**, *6*, 293–339.
- [15] Tang, J.; Li, L.; Guo, H.; Yu, H.; Wen, H.; Yang, M. Distributed acoustic sensing system based on continuous wide-band ultra-weak fiber Bragg grating array. *25th International Conference on Optical Fiber Sensors* **2017**, *10323*, 1032304.
- [16] Shatalin, S. V.; Treschikov, V. N.; Rogers, A. J. Interferometric optical time-domain reflectometry for distributed optical-fiber sensing. *Applied Optics* **1998**, *37*, 5600.
- [17] Liokumovich, L. B.; Ushakov, N. A.; Kotov, O. I.; Bisyarin, M. A.; Hartog, A. H. Fundamentals of Optical Fiber Sensing Schemes Based on Coherent Optical Time Domain Reflectometry: Signal Model under Static Fiber Conditions. *Journal of Lightwave Technology* **2015**, *33*, 3660–3671.
- [18] Rohwetter, P.; Eisermann, R.; Krebber, K. Random quadrature demodulation for direct detection single-pulse rayleigh C-OTDR. *Journal of Lightwave Technology* **2016**, *34*, 4437–4444.
- [19] Healey, P. Fading in heterodyne OTDR. *Electronics Letters* **1984**, *20*, 30.
- [20] Ames, G. H.; Donat, W. R. Fading statistics in Rayleigh interferometric fiber sensors. *23rd International Conference on Optical Fibre Sensors* **2014**, *9157*, 915767.
- [21] Koyamada, Y.; Imahama, M.; Kubota, K.; Hogari, K. Fiber-optic distributed strain and temperature sensing with very high measurand resolution over long range using coherent OTDR. *Journal of Lightwave Technology* **2009**, *27*, 1142–1146.
- [22] Koyamada, Y.; Eda, Y.; Hirose, S.; Nakamura, S.; Hogari, K. Novel Fiber-Optic Distributed Strain and Temperature Sensor with Very High Resolution. *IEICE Transactions on Communications* **2006**, *E89-B*, 1722–1725.
- [23] Wang, C.; Wang, C.; Shang, Y.; Liu, X.; Peng, G. Distributed acoustic mapping based on interferometry of phase optical time-domain reflectometry. *Optics Communications* **2015**, *346*, 172–177.
- [24] Zhu, F.; Zhang, Y.; Xia, L.; Wu, X.; Zhang, X. Improved Φ -OTDR sensing system for high-precision dynamic strain measurement based on ultra-weak fiber bragg grating array. *Journal of Lightwave Technology* **2015**, *33*, 4775–4780.
- [25] Zhang, X.; Guo, Z.; Shan, Y.; Sun, Z.; Fu, S.; Zhang, Y. Enhanced Φ - OTDR system for quantitative strain measurement based on ultra-weak fiber Bragg grating array. *Optical Engineering* **2016**, *55*, 054103.
- [26] Sandoghchi, S. R.; Petrovich, M.; Gray, D. R.; Chen, Y.; Wheeler, N. V.; Bradley, T. D.; Wong, N. H.; Jason, G. T.; Hayes, J.; Fokoua, E. N.; Alonso, M. B.; Mousavi, S. M.; Richardson, D. J.; Poletti, F. Optical side scattering radiometry for high resolution, wide dynamic range longitudinal assessment of optical fibers. *Optics Express* **2015**, *23*, 27960–27974.

Chapter 6

An Automated Reel-to-reel Fabrication System

6.1 Introduction

The concept of utilising ultrafast laser micro-machining to create points of enhanced reflection has been demonstrated in the previous chapter. By exploiting the smooth refractive index regime of femtosecond laser writing, precise scatterers can be written into the fibre. These rectangular interfaces comprising of a step change in refractive index cause a Fresnel reflection of the forward propagating interrogator pulse. These regions maximise the light returned to the detector whilst minimising the light out-scattered from the fibre. The initial proof of concept is extremely powerful for providing a viable solution for improving the signal to noise ratio for coherent Rayleigh ϕ -OTDR measurements.

To investigate the fibre's practical capability for distributed acoustic sensing, a fabrication system is required to produce arrays of hundreds of reflectors. The process to fabricate each reflector is the same each time. As found in the previous section, theory dictates that the fibre reflectivity is extremely sensitive to the force imparted on it. Hicke et al. showed that positioning of the reflector respective to the centre of the core is also essential; deviations of just 4 μm were found to effect void reflectivity by up to 10 dB [1]. Thus, a system precisely controlling the forces acting on the fibre and its positioning during reflector inscription is required. When compared with other works producing Bragg grating arrays or continuous gratings, two options are available: a fabrication system on a fibre draw tower; or a reel-to-reel inscription system [2, 3, 4, 5] The following chapter outlines the details of an automated fabrication system that was developed and the concepts underpinning its operation.

The fabrication system was assembled with the support of Masters students from the Eindhoven University of Technology: Sjoerd Tunnissen;, Frank Bouwmans; and Jian Kok. Sjoerd assisted with the assembly of the mechanical elements of the system. Frank created the 3D computer designs of the roller holders and the fibre optic rotary joint holder. Jian implemented the learning control algorithms of the Arduino, designed the distance measurement part and programmed the receiving bobbin translation stage.

6.2 Process Overview

The objective of the fabrication system is to produce optical fibre containing micro-machined enhanced reflection points. The separation between enhanced reflection points should be periodic in nature and their reflectivity will be equal. To achieve this, the set up can be divided into three independent fabrication processes: winding; positioning and inscription (Fig. 6.1.) The automated system was programmed in MATLAB. Before the fabrication can begin the hardware must be initialised and the software algorithms must be calibrated with the assistance of a human user.

The first part of the system is similar to commercially available fibre rewinding machines. Here, the system has been designed to incrementally unwind optical fibre from commercial-standard bobbins. As fibre is unwound from a feeding bobbin, on the opposing side fibre is being wound onto a feeding bobbin. After unwinding, the fibre must be positioned under a microscope objective for inscription. Once positioned to within 1 micron on each axis, the reflector can be fabricated. To ensure the quality of each individual the reflection points an in-situ optical time domain reflectometry (OTDR) set up was constructed. In terms of positioning, the optical fibre must be placed to an accuracy of 1 micron, in all 3 axes. Such accuracy is essential to maintain a consistent reflectivity of each enhanced scattering region.

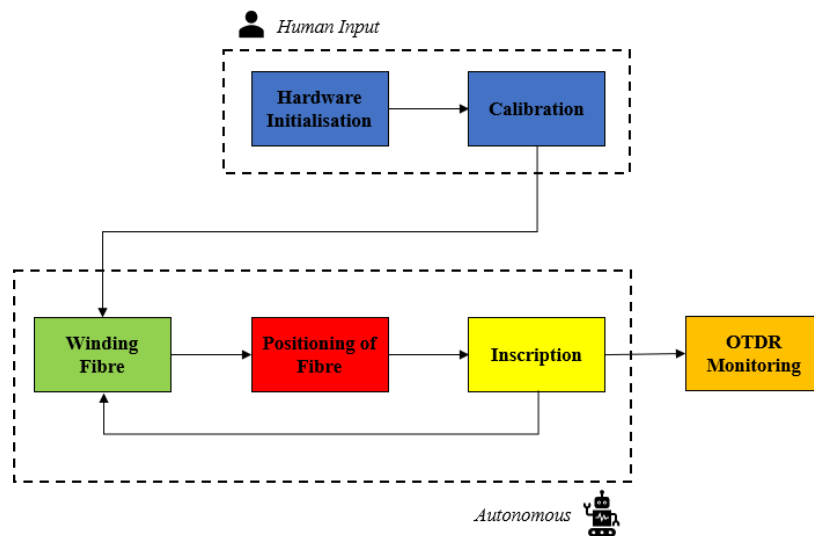


Figure 6.1: A flow diagram of the fabrication process of the enhanced reflector fibre. First, the hardware is initialised and calibrated with the assistance of a human. After the fabrication process can begin: first with the unwinding of fibre, followed by placement under a microscope objective, and finally with inscription. To ensure reflectors were being inscribed in the core, real time optical time domain reflectometry is completed.

6.3 Fibre winding

A reel-to-reel fibre rewinding machine was assembled. The system comprises of unwinding of a feeding bobbin containing fibre for processing, and a receiving bobbin which collects

the process fibre. During the winding, the fibre goes through three parts of the reel-to-reel rig: a tension compensation system; a length measurement device; and the laser. The following section details the mechanical design of the elements in these parts of the system. After, the software architecture controlling these mechanical components is detailed.

6.3.1 Mechanical Design

Winding Motors

The fibre winding is powered by two stepper motors (RS Pro) possessing a 4.31 Nm holding torque. One motor is used for each of the two bobbins: the feeding bobbin which unwinds unprocessed fibre; and the receiving bobbin which winds up the enhanced reflector fibre after modification. The stepper motors are coupled to an axel with a flexible shaft coupler. Upon this axel, the bobbins are secured. The motor and axel are joined by a flexible shaft coupler for both arrangements. Flexible shaft couplers are used as they accommodate angular misalignment between the axel and the motor shaft. Support structures are introduced as the mass of the bobbin is too large to be supported by the stepper motor alone. The axel is run through a spherical plain bearing which is fixed in-line with the axel. Spherical plain bearings permit angular rotation about two orthogonal directions. Again, this compensates for any angular misalignment between the axel and motor shaft. Compensating for misalignments with the flexible shaft coupler and spherical plain bearing are critical for preserving the lifetime of the system. If not, these misalignments cause additional resistive stresses and strains on the motor shaft, increasing its wear and hence, decreasing its lifespan. There are two

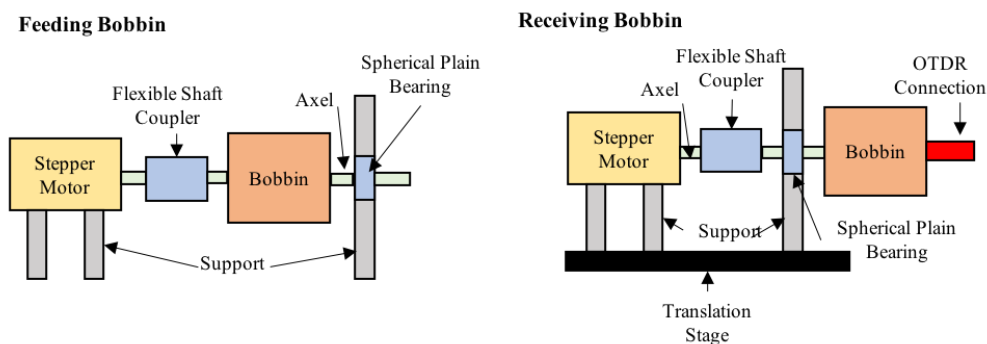


Figure 6.2: A schematic diagram of the feeding bobbin (left) and the receiving bobbin (right). The receiving bobbin support occurs after the flexible shaft coupler due to the presence of the connection joint to the OTDR feedback system. The receiving bobbin arrangement is also placed on a single axis translation stage to ensure the fibre is wound evenly.

differences between the feeding and receiving bobbin. Firstly, the position of the support holding the spherical plain bearing is after the flexible shaft coupler on the receiving bobbin. Ideally, it would mirror the feeding bobbin arrangement as it is optimal to have a point of support on either side of the bobbin. However, this is not possible on the receiving bobbin due to the OTDR connection. More details on this can be found in section 6.6. The second difference is the receiving bobbin is placed upon a single axis translation stage (Zaber, X-LRT0500BL-C) with a 0.5 m range of motion. The stage translates along the axel axis, perpendicularly to the fibre. This is to allow sequential

winding of the fibre. The translation stage is stepped the distance of one fibre width for each rotation of the bobbin. Neat winding is essential for the manufacture of consistent reflectors. This is to ensure consistent forces are imparted on the fibre when wound onto a bobbin to allow direct comparison in performance of the inscribed reflectors.

Tension Compensation System

When winding the fibre, tension variation can occur due to the asynchronicity of stepper motors. These variations mean the fibre is susceptible to rapid changes in strain and subsequent breaking. As well as to prevent breaking, maintaining a constant tension is of paramount importance for a plethora of other reasons. Firstly, it ensures minimal slip between the pulleys and fibre. Secondly, constant tension is essential to create a smooth and consistent wrap on the receiving bobbin. Finally, in-between winding of the fibre, tension should remain as consistent as possible to ensure reflector performance variations are minimised. Deviations in the fibre tension impacts the the reflectivity observed. Maintaining a consistent tension between reflectors allows comparison of performance. Without it, it is unknown whether variation in reflector performance is due to differences in strain on the fibre or variations from the inscription.

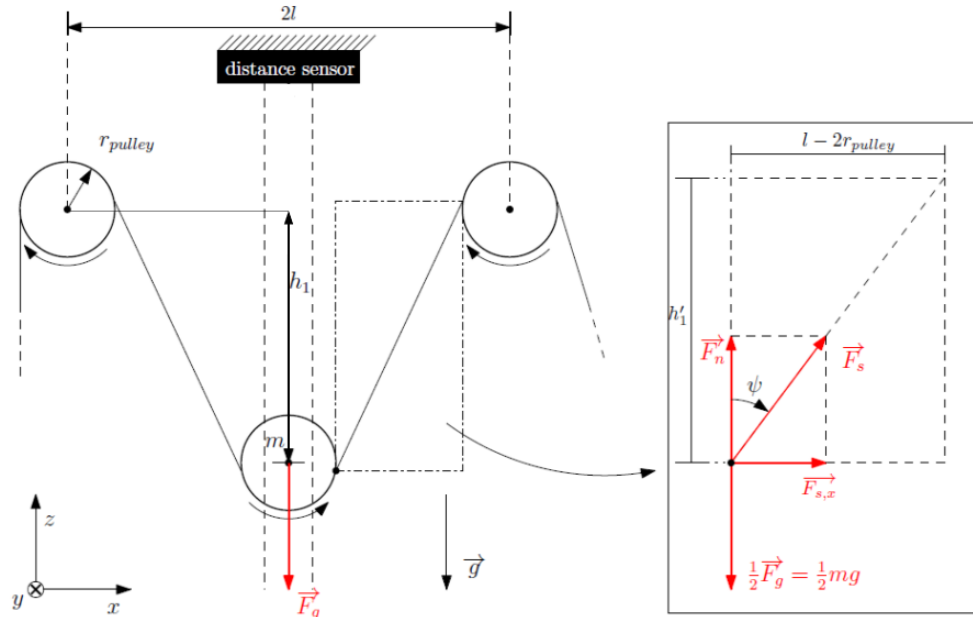


Figure 6.3: A force diagram of the tension compensation system where: $2l$ is the distance between the centre of mass of the two stationary pulleys; r_{pulley} is the radius of the pulleys; h_1 is the height from the centre of mass of the pulley located on the carriage, to the plane in line with the stationary pulleys; \vec{F}_n is the normal force acting upon the moveable pulley; \vec{F}_s is the axial tension in the fibre; $\vec{F}_{s,x}$ is the x-component of the axial tension in the fibre; and g is the acceleration due to gravity; m is the mass of the moveable pulley, carriage and reflection plate.

To achieve this, a tension compensation system has been implemented to manage the forces imparted on the fibre (Fig. 6.3.) The compensation system comprises of a low friction bearing rail and carriage. Upon the carriage, a 3D printed reflection plate and pulley was attached (Fig. 6.4.) To maintain a constant tension, the position of

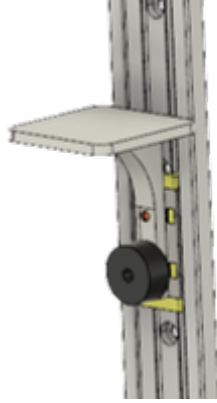


Figure 6.4: A 3D CAD drawing of the tension compensation pulley. The system comprises of a low friction bearing rail and carriage, with a 3D printed white reflection plate and pulley attached. The carriage had a combined mass of 87g.

the carriage must be monitored. Thus, an infrared distance sensor (SHARP) is used to monitor the position of the carriage. The sensor has a precision of ± 0.5 mm. The white reflection plate on the carriage provided the object surface for the sensor to make a measurement. The sensor was placed 100 mm from the reflection plate at its maximum position, as this is the sensor's minimum range.

The maximum mass of the carriage is dictated by the tensile strength of the optical fibre used. Corning SMF-28e was used predominantly in our experiments, which is proof tested at 0.69 GPa. From this, the maximum force that the fibre had been tested up to was 8.46 N. Therefore, it was sought not to exceed this limit. Hence, the limit of the carriage can be calculated from the angle ψ , defined as that between the normal force \vec{F}_n , and the axial tension \vec{F}_s such that:

$$\begin{aligned}\vec{F}_s &= \frac{\vec{F}_g}{2 \cos \psi} \\ &= \frac{mg}{2 \cos \psi} \\ \cos \psi &= \frac{mg}{2\vec{F}_s}\end{aligned}\tag{6.1}$$

Eq. 6.1 shows that to permit collaboration with industrial partners, the pre-loaded tension was aligned with other commercially available winding machines. Thus, the maximum axial tension, \vec{F}_s was capped at 0.59 N. Therefore the maximum angle ψ can be calculated from 6.1 shows that the tension varies with angle ψ . To minimise the effect, the pulleys either side of the rail were placed as close to one another as possible. Subsequently, a height limit $h'_1 \geq 33$ mm can be defined.

Measuring Fibre Length

When fabricating the enhanced reflector fibre, consistent spacing of enhanced back reflection is of paramount importance. To determine the distance of fibre that has

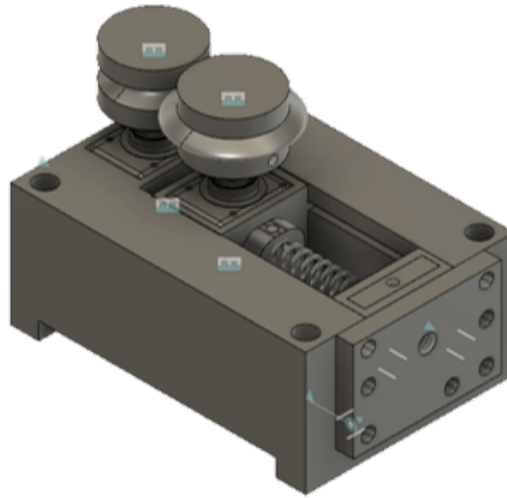


Figure 6.5: A 3D CAD drawing of the distance measurement component.

been wound, a rotary encoder (Bourns) was employed. The encoder was positioned after the tension compensation system. The encoder used 5 V digital communications and had a resolution of 256 pulses per revolution. The encoders are designed to be coupled to a grooved wheel.

There are many sources of inaccuracy when determining the length of fibre that has been wound. There are two sources that lead to an inflation of the distance recorded: the inertia of the encoder wheel after winding has stopped; and off axis rotation of the encoder wheel. There are three sources of inaccuracy leading to an under-measurement of distance: latency of the microcontroller causing missed counts; the resolution of the encoder; and slipping of the fibre over the rotary encoder. The resolution of the encoder is inherent and cannot be avoided. As our rotary wheel was 25.8 mm in diameter, this meant the encoder had a resolution of ~ 0.3 mm. This resolution was far higher than what was necessary.

The other causes of inaccurate distance measurement could be minimised with effective component design. Thus, a bespoke distance measurement component was created (Fig. 6.5.) The part had two encoders coupled to two wheels. The two wheels were designed so one guided the fibre through the groove of the other. The distance between the two wheels was adjustable using a screw and a spring. This meant the friction acting upon the fibre could be partially adjusted by altering the spacing between the two wheels. This minimised the slipping that could occur between the fibre and the wheel.

Minimal slipping was verified by measuring the encoder counts in real time through the winding of 1 meter of fibre (Fig. 6.6.) The motor was programmed to wind two revolutions (1600 steps), which was approximately 1 meter (given a 0.5 m circumference bobbin.) The encoder had a circumference of 81 mm, thus, a total of 3159 encoder counts was expected to be recorded.

In total 3197 encoder counts were recorded translating to 1.01 m being wound. Motor step was then converted into time given the speed profile applied to the motor. If slipping was observed through the trajectory, flat line responses of encoder count in time would

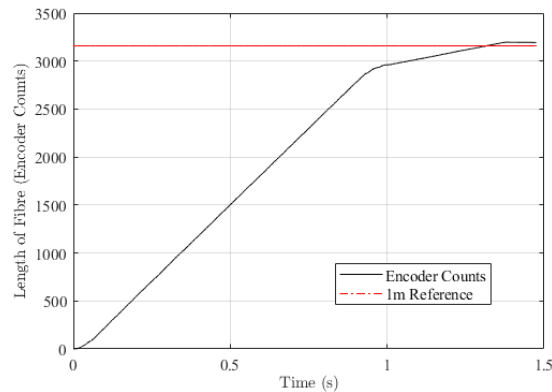


Figure 6.6: A graph of the encoder counts recorded when 1600 steps is sent to the stepper motor.

be observed - a step would be made of the motor, but no increase in encoder count would be observed. From 0 to 0.01 seconds slipping of the fibre was observed. The speed profile began and ended at 0.4 revolutions per second. This was to avoid two natural resonance frequencies of the motor at lower speeds. Furthermore, this termination of the stepper motor at 0.4 revolutions per second means a length larger than 1 meter would be wound as the inertia of the bobbin means further steps whilst the motion decelerates to zero.

Traversing the Laser

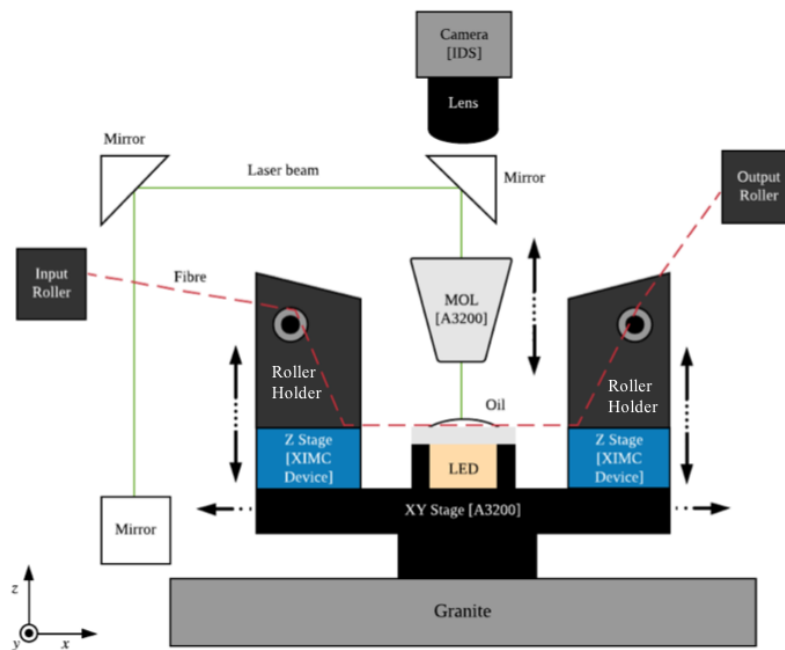


Figure 6.7: A diagram of the mechanical design within the laser safety enclosure to position fibre beneath the microscope objective.

After leaving the tension compensation system, the fibre is guided into a laser safety

enclosure, for positioning under the microscope objective (Fig. 6.7.) For inscription, the fibre had to be guided beneath an objective lens located above an XY-stage (Aerotech). The input roller and output roller guided the fibre on its entrance into, and out of, the safety enclosure, respectively. Two roller holders on top of the Z-stages were responsible for guiding the fibre onto a fibre platform. A collimated LED was situated beneath the fibre platform to provide illumination. were attached on two z -axis stages (Stand-8MVT0-13), either side of the fibre platform. The Z-stages were placed on an XY-stage, along with the fibre platform. The XY-stage was secured to a granite block to provide stability and dampen the system from surrounding environmental noise.

Ideally, when designing the system, all parts of the system would be aligned in the xz -plane. However, this was not possible due to laboratory constraints. When comparing the xz -plane of the fibre leaving the tension compensation system and the XY-stage, a deviation, Δy can be observed (Fig. 6.8.) In the experiments, $\Delta y = 120mm$. Thus, to allow the fibre to alter its y position, the fibre must be fixed at the x and z positions when entering the laser safety enclosure and also, at the entry to the XY stage. The input/output roller and roller holders were designed to accommodate the shift in the xz -plane. A similar shift in xz -planes was also observed from the XY-stage and leaving the laser safety enclosure. To avoid repetition, only the shift from the xz -plane to XY-stage is discussed. The principles are similarly applicable to the transition from the XY-stage to exiting the laser safety enclosure.

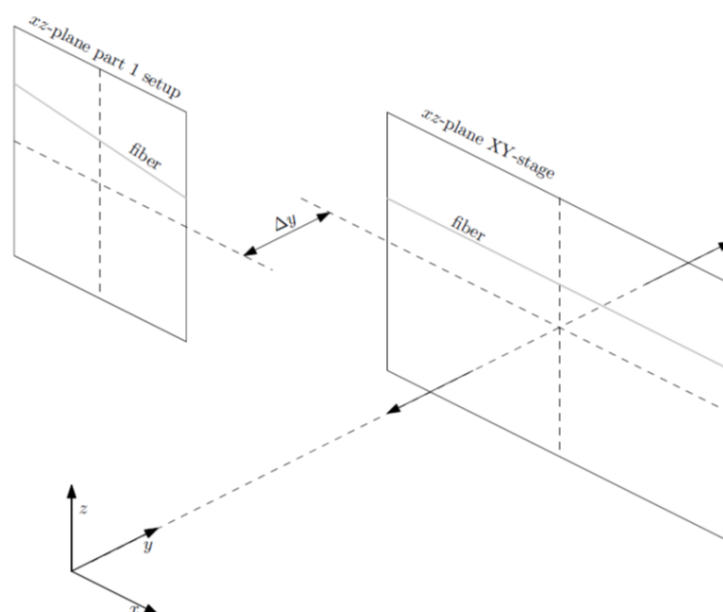


Figure 6.8: A diagram illustrating the xz -plane difference between the first and second part of the winding system.

The input and output roller were bespoke parts that were 3D-printed. The holders were designed using 3D-CAD software (Fig. 6.9.) Each holder contains four rotating cylinders. The rotating cylinders comprised of a central axel, cylindrical shell, two ball bearings and a spring. The cylinder shells were 100 mm in length and had an outer diameter of 20 mm. The axel was 117 mm in length. The spring allowed the cylinder to be compressed in its axial direction to allow for push fit installation. The cylinders were secured using an end cap that was screwed into the box.



Figure 6.9: A 3D CAD drawing of the input roller box.

To allow the fibre to change its y position towards the XY-stage, the input/output rollers were designed to enable the fibre to turn around a rotating cylinder with its axial axis orientated on the z -axis. Two cylinders were positioned with their axes on the z direction; the box was orientated such that these two rollers were close to the XY-stage. The two rollers were separated in the y axis by 20 mm, equal to the diameter of the cylindrical shell.

This was specifically designed to ensure the fibre remained in contact with both rollers at all times; if only one roller was present, any rapid changes in tension could cause the fibre to jump and subsequently, cause it to lose contact with the cylinders. In turn, this would exert unwanted forces onto the fibre itself that could harm the coating structural integrity.

The tension compensation system and input roller were located at different z -axis co-ordinates. To prevent the fibre slipping in the z -axis, two rotating cylinders were also positioned with their axial axis orientated on the y -axis. The cylinders axes were distanced 20 mm apart in the y axis; as mentioned before, this was to ensure the fibre remained in contact with both cylinders if sudden forces were imparted on the fibre. If these cylinders were not present, the fibre would have a gradient in the z -axis leading to a decoupling between the horizontal and vertical tension components. Subsequently, slipping of the fibre would occur which could be detrimental to the fibre structural integrity (Fig.6.10.)

The Z-stages have a range of 13 mm. Their function is to raise the fibre from the fibre platform before the fibre is wound. As an oil-immersion objective lens is employed, index matching oil covered the fibre. Thus, the z -stages raised the fibre out of the oil, preventing unmodified regions from interacting with it. This increases the utilization of the oil tenfold, before further oil deposition is required. After winding is completed, the stages are lowered to place the fibre back onto the platform. The stages also allowed precise, repeatable positioning of the fibre upon the platform. The stages had a $1\ \mu\text{m}$ accuracy. This was key to maintaining a consistent axial tension within the optical fibre to ensure minimal variation in the reflectivity.

The roller holders were bespoke 3D printed parts designed using 3D-CAD software (Fig. 6.11.) The component holds 3 bespoke rotating, low-friction cylinders, whose

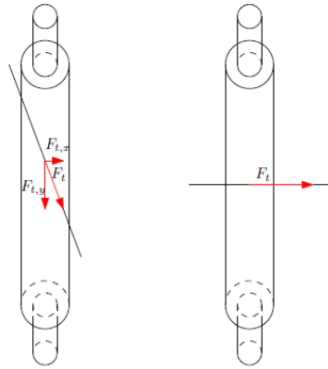


Figure 6.10: A schematic force diagram of the fibre passing over the y -axis cylinder: on the left, without z axis cylinders; and on the right, with z -axis cylinders. Without the z axis cylinders the axial tension F_t decouples into an x and y component, $F_{t,x}$ and $F_{t,y}$, respectively. This decoupling leads to the fibre slipping down the cylinder, as the cylinder rotates around the y -axis

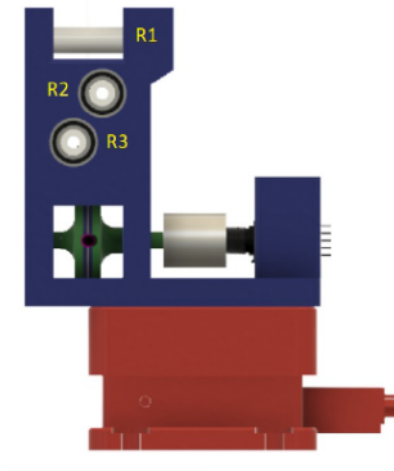


Figure 6.11: A 3D CAD drawing of the roller holders located on the z -stages. $R1$, $R2$ and $R3$ are three custom made low friction, rotating cylinders.

function were to guide the fibre from and to, the *roller boxes*. The cylinders were 50 mm in length and had an outer diameter Cylinder R1 axial axis is orientated in the y -axis. Its function was to allow the fibre to be guided onto a pulley located at a lower z position. Cylinders R2 and R3 were orientated with their axial axis parallel to the x -axis. These cylinders aligned the fibre's y -position with that of the pulley wheel's. The groove of the pulley wheel was 200 μm in width. Each pulley wheel is coupled to a rotary encoder to allow distance measurements to verified if necessary. These encoders are not used to control the fibre length.

6.3.2 Software Design

Microcontroller

The fibre winding mechanism was managed using a microcontroller (Arduino Mega 2560 Rev 3.) The board uses an ATmega2560 chip, which has a 16 MHz clock. Therefore, a single instruction has a 62.5 ns execution time. The board contains 100 pins ordered in ports, and is capable of both digital and analogue communication. The benefit of using Arduino is its widely available off-the-shelf libraries allowing rapid prototyping. As the system went through many stages of development, the Arduino's flexibility allowed various methodologies to be easily tested. In addition to standard off-the-shelf libraries, the Arduino also permits direct command of the ATmega2560 chip. This allowed the ability for manipulation of fundamental functions. For example, the **DigitalWrite()** function which changes the digital signal from a pin, takes 16 ms to execute. By utilising direct port manipulation, this could be rewritten to execute in two clock cycles (125 ns.) Rewriting fundamental functions of the Arduino to reduce latency was key in achieving smooth, accurate winding. A copy of the code implemented on the Arduino can be found in the Appendix. The Arduino was responsible for managing four elements: the motors coupled to the feeding and receiving bobbin respectively; the distance sensor; and the rotary encoder.

Stepper Motor Velocity Profile

The microcontroller uses a single core CPU and therefore can only execute one line at a time - parallel processing is not possible. The microcontroller has to simultaneously drive the two motors whilst monitoring the encoder counts in interrupt mode. The encoder count is then fed back in real-time during actuating them. Thus, to reduce latency in the programming, the two motors are given the same trajectory profiles. The motors are driven from the same port on the microcontroller to ensure they are synchronised.

When the stepper motor speed is below 0.4 revolutions per second, natural frequencies of the motor cause undesired resonances, draining energy from the motion. Thus, the optimum starting velocity to avoid these frequencies was found to be 0.4 revolutions per second. The motors could be run at 12 revolutions per second however, breaking of the fibre was observed at 2.8 revolutions. Therefore, the maximum speed of the motors was capped at 2 revolutions per second. The stepper motors actuate a step upon the high to low transition of the digital signal driving it. Therefore, the delay between digital pulses translates to a speed. An approximation of the delay in microseconds to reduce computing time is derived and can be summarised by [6]:

$$c_0 = 0.676 \cdot f \sqrt{\frac{2\alpha}{\omega'}} \quad (6.2)$$

$$c_i = c_{i-1} - \frac{2 \cdot c_{i-1}}{4 \cdot i + 1} \quad (6.3)$$

$$c_i = c_{i-1} + \frac{2 \cdot c_{i-1}}{4 \cdot (m - i) + 1} \quad (6.4)$$

where i is the step number, m is the step number where the decelerating period ends, c_0 is the delay in the microcontroller clock cycles, f is the timer frequency in Hz, α is the step angle in rads, and ω' is the angular acceleration in rads s^{-2} . As the motor is

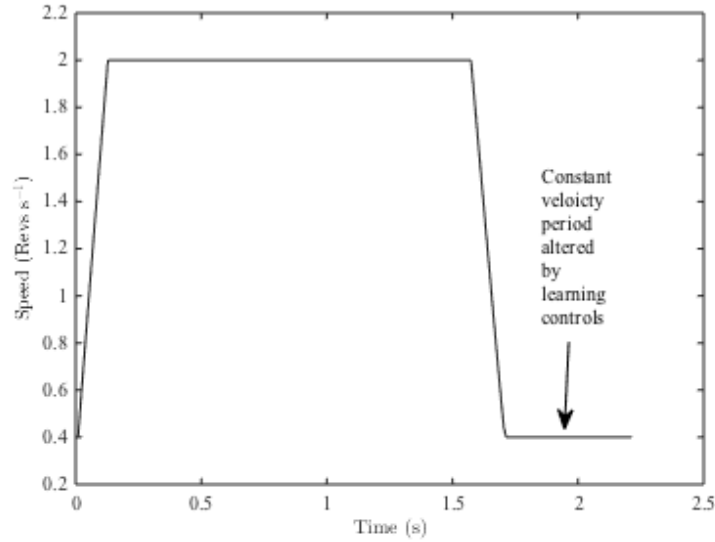


Figure 6.12: The velocity profile of the stepper motors coupled to the feeding and receiving bobbins. The final constant velocity period is variable in duration, altered by learning control algorithms.

controlled in a half stepping $\alpha = \frac{2\pi}{400}$ radians; $f = 16$ MHz and $\omega' = 21 \cdot 2\pi$ rads s^{-2} . Eq. 6.2 is the first delay time inputted into the stepper motor; Eq.6.3 is the subsequent delay times for the acceleration period; and Eq. 6.4 is the delay for the deceleration period. The resultant velocity profile of the stepper motors is trapezoidal in nature with linear acceleration and deceleration (Fig. 6.12.) On the velocity profile, the delays of the digital pulses have been converted into a speed of revolutions per second, and the steps have been converted into a time. The length of the constant velocity period at the end of the profile is altered by a terminal iterative learning control (TILC). The necessity for this is explained in the following section.

Learning Controls

When a sample of enhanced backscatter fibre is fabricated, a bobbin with fibre is loaded onto the feeding motor and an empty bobbin is loaded onto the receiving motor. As the fibre is wound onto the receiving bobbin, its diameter increases and the diameter of the feeding bobbin reduces. Both motors are given the same angular trajectory, but due to differences in bobbin diameter, this results into relatively small differences in the amount of fibre being unwound from the feeding side, and wound up on the receiving side. Imbalances in the amount of fibre will be reflected in the height of the carriage of the tension compensation system. If the feeding bobbin unwinds more fibre than the receiving bobbin winds up, the carriage will finish lower than when it started. Conversely, if the feeding bobbin unwinds less fibre than the receiving bobbin winds up, the carriage will finish at a higher position than when it started.

As was shown earlier, in 6.3.1, the position of the carriage during the inscription will effect the tension loaded into the fibre. Thus, after winding, the carriage position is returned to the same position by forwarding or reversing the feeding bobbin. To ensure

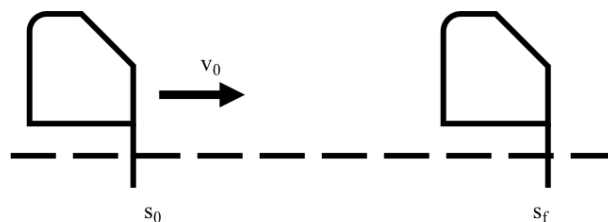


Figure 6.13: A schematic of the station stop control problem. A train is travelling at a constant velocity v_0 , at position s_0 and needs to stop at a station, located at position s_f .

the desired distance is wound onto the receiving bobbin, the stepper motor trajectory must be adjusted. To do this, learning control algorithms were implemented. Iterative learning controls (ILC) are especially effective for highly repetitive tasks such as that of our winding machine. ILC operates on the basis of monitoring a reference signal on a finite time interval.

The problem posed by the winding system is analogous to the station stop control problem [7]. In this scenario, a train is travelling at a constant velocity v_0 , at position s_0 and needs to stop at a station, located at position s_f (Fig. 6.13.) If braking is triggered too early, the train will fall short of the desired final distance. If triggered too late, the train will finish beyond the desired distance. In the problem, there is assumed to be varying dynamics meaning the distance at which braking is triggered is not the same each time. In the case of the fibre rewinding system, the changing bobbin diameter (as well as other minimal fluctuations that are difficult to approximate) causes varying dynamics, altering this distance. The winding machine can be approached in the same manner as the station control problem as the stepper motors are triggered to stop at a speed of 0.4 revs s^{-1}

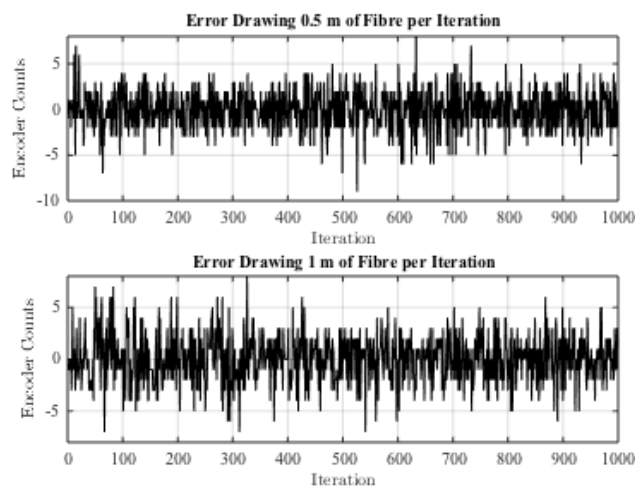


Figure 6.14: Graph of the encoder error for 1000 iterations drawing 0.5 m per iteration (top); and 1 m per iteration (bottom).

To solve this issue, a terminal iterative learning control (TILC) solution was implemented. In this case, the input signal for the next iteration is updated based upon the reference signal recorded from the previous iteration. The input signal for the next

iteration is known as the feedforward signal and can be expressed mathematically as [7]:

$$FF_{i+1} = FF_i + \beta f(\Delta s_i) \quad (6.5)$$

Where FF_i is the input signal from the previous iteration, β is the learning gain and Δs_i is the error in the final result. β is defined as $0 \leq \beta \leq 1$ for the function to converge monotonically. As can be seen in Eq. 6.5), the feedforward signal for the next iteration is a function of the error in final position. The error can be expressed as [7]:

$$\Delta s = s_f - s_i \quad (6.6)$$

where s_f is the desired final distance and s_i is the measured position from the rotary encoder. In the solution implemented in our winding system, the input signal was the stepper motor velocity profile and the learning control algorithm altered the length of constant velocity (Fig. 6.12.)

The learning control algorithms were verified in two tests of 1000 iterations: firstly drawing 0.5 m per iteration; and secondly, 1 m per iteration. The error of each iteration can be seen in Fig. 6.14. In both tests, a feeding bobbin with approximately 20 km of fibre, and an empty receiving bobbin, was used. The receiving bobbin can store 200 m of fibre before increasing in diameter. Therefore, increases should be seen after every 200 m of fibre wound. The learning control algorithms performed as expected over 1000 iterations showing convergence to, and oscillation around zero encoder error counts. Oscillations around zero are expected due to noise caused by measurement error and stochastic environmental fluctuations.

The error distribution was summarised in a box plot (Fig. 6.15.) The interquartile range (IQR) is shown by the blue box. In the 0.5 m per iteration test, the IQR is 4 encoder counts, centred with the median at 0. In the 1 m per iteration test, the IQR is 2 encoder counts, centred with the median at 0. The $\pm 2.7\sigma$ range runs from 9 to -7 counts for the 0.5 m per iteration test and 4 to -4 counts for the 1 m per iteration test. The symmetrical nature of the box plots demonstrate there is no skew in the data and thus, the learning algorithm is converging the error to zero over the 1000 iterations as desired.

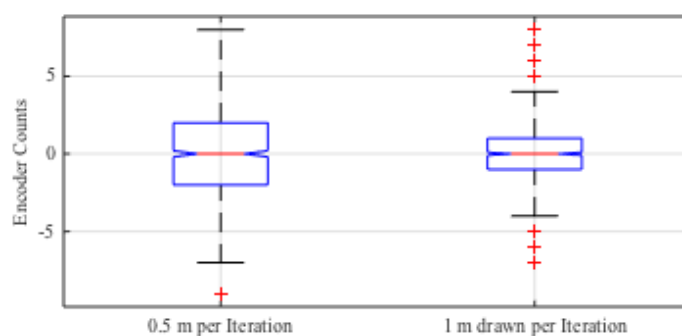


Figure 6.15: A box-plot showing the distribution of errors recorded for the 1000 iteration winding tests of: 0.5 m per iteration (left) and 1 m per iteration (right.) The whiskers of the plots are set at $\pm 2.7\sigma$ and outliers are marked with red crosses.

6.4 Fibre Positioning

After the desired amount of fibre is wound, it must be placed appropriately under the microscope objective for inscription. When fabricating reflectors in the previous chapter, the fibre was positioned manually under the inscription objective using a CMOS (IDS, Sony CMOS Camera). For fabrication of long sample lengths, having an individual do this repetitively is extremely inefficient. To manually position the fibre under the camera would take approximately 60 seconds. Therefore, to fabricate 1000 points manually, would take over 16 hours. The presence of the CMOS enabled computer vision techniques to be employed. Computer vision refers to any computational models which attempt to replicate the human vision system and therefore, can be used for the automation of tasks. The following section discusses the theory and logic behind the computer vision algorithms that are used for positioning the fibre appropriately for inscription.

6.4.1 The Fibre

The computer algorithms are designed for a standard single mode telecommunications fibre (Corning SMF-28e+, Fig. 6.16.) The fibre has two coatings, both made of acrylate. The outer layer improves the mechanical strength of the fibre. The outer diameter of the fibre is $242 \pm 5 \mu\text{m}$. The inner layer protects the fibre from chemical degradation. The area between the coating and core is the cladding of the fibre. This has an outer diameter of $125 \pm 0.7 \mu\text{m}$. The central circle depicts the core. This is $8.2 \pm 0.2 \mu\text{m}$ in diameter. The fibre has a step index profile; the core has a refractive index difference of $\sim 10^{-3}$ compared to the cladding. At 1550 nm, the fibre has an attenuation of 0.2 dB per kilometre and an average mode field diameter of $10.4 \mu\text{m}$.

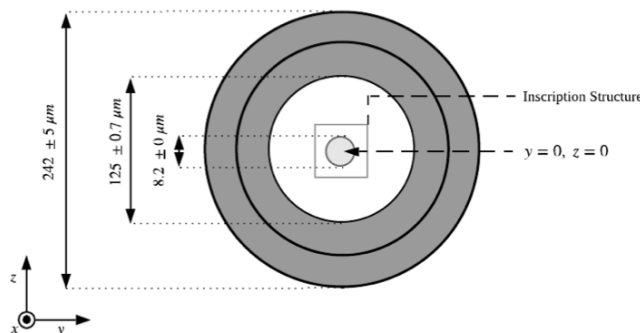


Figure 6.16: A diagram of the cross section of the single mode telecommunications fibre used. The fibre is made up of an outer coating (largest grey circle), an inner coating (inner grey circle), cladding (outer white circle) and core (central circle.) The intended inscribed structure is displayed as a black box surrounding the core.

6.4.2 Camera Configuration

The camera was connected to MATLAB using the IDS .NET framework and was configured through an initialisation script. Optical fibre images were captured and

analysed (Fig. 6.17.) The figure is annotated with the features of the optical fibre. The refractive index difference is on the order of 10^{-3} between core and cladding. Hence, its contrast is extremely small. As such, its boundary lines have been emphasised with red lines. The image shows that each boundary between layers of the fibre appear as black lines. These were key features of the fibre image that could be exploited using edge detection algorithms. When configuring the parameters of the camera, an attempt accentuate the fibre features was made through a trial and error approach.

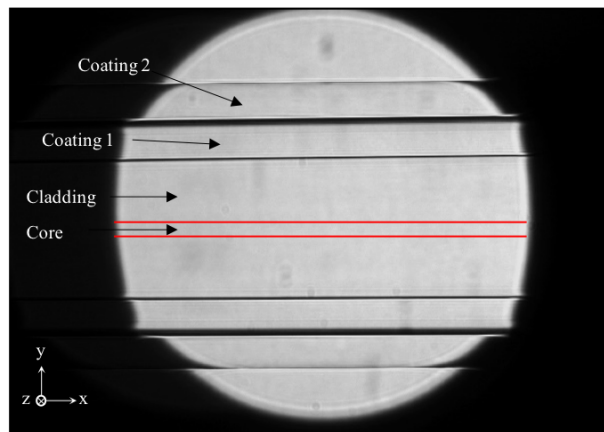


Figure 6.17: An annotated CMOS image of the single mode telecommunications fibre (Corning SMF-28e.) The fibre has two coatings: the outer (coating 2) for mechanical reinforcement; and the inner (coating) to protect against chemical degradation. The core has been emphasised due to its low contrast.

The camera used had the ability to deliver either an RGB-colour image or a greyscale image. As colour detail did not add any value and delayed processing, the camera captured monochromatic images only. The black background surrounding the image is caused by the edge of the microscope objective aperture; it is smaller than the CMOS sensor. As the entire sensor was not utilised, image cropping was used to isolate the region of interest. Furthermore, field curvature effects at the edge of the objective aperture were apparent, distorting the image. This is a common effect in microscopy as the objective images a flat plane onto a Petzval surface [8]. As you move further from the centre, this effect worsens. Thus the image was further cropped to remove these distorted regions (Fig. 6.18.) The final image was 650×1850 pixels. The height was maximised as much as possible to avoid the fibre moving out of view between each iteration.

The cropping was implemented using the hardware. Thus, the camera only delivered the CMOS sensor response from the user-defined, region of interest. Another option would have been cropping the image using MATLAB. This was not chosen as hardware cropping increased the frame-rate of the camera 3-fold and further, reduced the digital image processing steps required.

6.4.3 The Positioning Process

For reflector inscription, the centre of the core must be placed under the focal point of the laser. To achieve this, the simplest logic seemed to centre the fibre so that ($y = 0, z=0$) is in the middle of the camera image and subsequently, move the fibre so

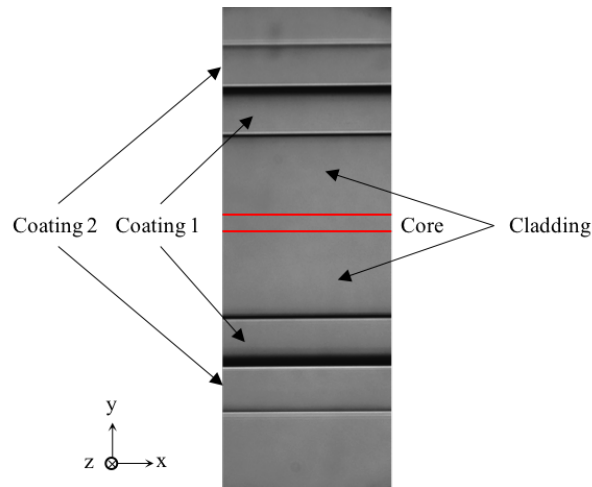


Figure 6.18: The image image of the single mode telecommunications fibre (Corning SMF-28e.)

that ($y = 0, z=0$) is then under the focal point of the laser. Attempts were made to manually align the camera such that the laser focal point was at the centre of the CMOS image. This was extremely difficult to achieve perfectly and thus, a fixed offset in the y direction must be applied. Therefore, the fibre positioning can now be broken up into three processes: positioning the fibre at $y = 0$ ("Y-positioning"); positioning at $z = 0$ ("Z-focussing"); and then applying the offset.

6.4.4 Y-Positioning: Computer Vision Techniques

The following subsection describes the computer vision techniques used in the Y-positioning algorithms. The best way to identify a fibre was using its the boundaries between the various layers of the fibre. These appeared as lines on the camera image as shown previously in Fig. 6.17. To identify these boundaries, edge detection algorithms were employed.

Median Filtering

Before edge detection processing could be applied the image underwent median filtering. Median filtering is a non-linear signal processing technique, especially effective to remove granular noise in an image. The filter is applied to each pixel individually and compared to surrounding pixels. The comparison area is defined by the user as a 2-dimensional array of x -by- y elements. The pixel is then redefined as the median value of this area.

Fig. 6.19 pictorially demonstrates how a 3-by-3 sized median filter redefines the value of a pixel in a matrix. The pixel that is being processed is shaded red and the comparison area is outlined in red. After the filter has been applied, the new value (the median of the 9 values considered) is used as the new pixel value. When the next pixel is defined, the old pixel value is used for comparison. For the Y-positioning algorithm, a 50-by-2 (x,y) matrix was applied.

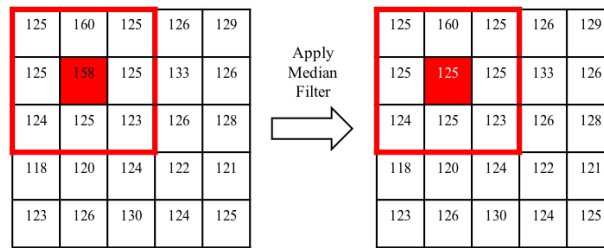


Figure 6.19: A diagram illustrating how a 3-by-3 median filter is applied to a matrix. On the left is the original matrix, before the median filter is applied. The red highlighted cell shows the pixel that is being processed. The red outlined area shows the 3-by-3 comparison area. On the right is the result after applying the median filter. The white value is the new pixel value - the median of the 9 values that were compared.

Sobel Operator

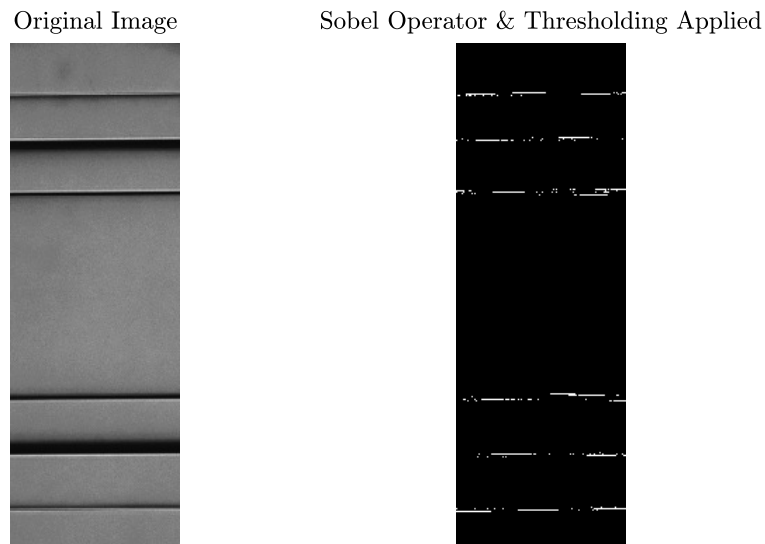


Figure 6.20: A CMOS image of SMF-28e optical fibre (left) and the subsequent binary image (right) after application of the MATLAB Sobel operator and threshold filtering.

After the median filter, a Sobel operator was applied to the greyscale image. The Sobel filter is a discrete differentiation operator, computing an approximation of the gradient of the greyscale image in an effort to accentuate edges. The filter is broken down into an x and y integer matrices which are convolved with the original image. The benefit of using such filter is its relative simplicity meaning it is computationally inexpensive to perform. The operation can be expressed mathematically as:

$$\mathbf{G}_x = \begin{bmatrix} +1 & 0 & -1 \\ +2 & 0 & -2 \\ +1 & 0 & -1 \end{bmatrix} * \mathbf{A} \quad (6.7)$$

$$\mathbf{G}_y = \begin{bmatrix} +1 & +2 & -1 \\ 0 & 0 & 0 \\ -1 & -2 & -1 \end{bmatrix} * \mathbf{A} \quad (6.8)$$

where \mathbf{G}_x and \mathbf{G}_y are the horizontal and vertical derivative approximation of the Sobel operator, respectively; \mathbf{A} is the greyscale intensity image; and $*$ is the 2D matrix convolution operation. Typically, the vertical and horizontal derivatives are combined such that:

$$\mathbf{G} = \sqrt{\mathbf{G}_x^2 + \mathbf{G}_y^2} \quad (6.9)$$

to give \mathbf{G} , the overall derivative intensity approximation of the image. In our case, the fibre shows edges solely parallel to the x -axis. Therefore, to reduce computation time even further, only the vertical gradient Sobel operator from Eq. 6.8 was applied. The Sobel operator was applied using the Image Processing toolbox. The output of the `edge()` function was a binary image. The binary image was calculated by adding an extra threshold layer to the Sobel operator - if the resultant gradient was above a user defined threshold, the pixel was set to a value of 1; else a value of 0 was used.

Hough Transform

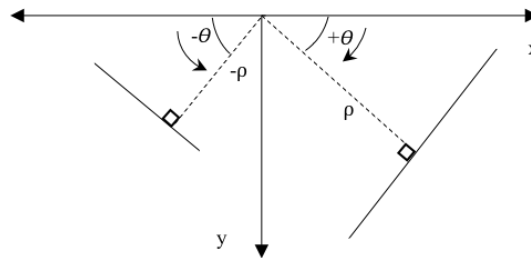


Figure 6.21: A diagram defining the parameters of the Hesse normal transform for a line formed from a series of Cartesian co-ordinates. ρ is the length of a normal from the origin to this line; θ is the orientation of ρ with respect to the x axis. Within MATLAB, the Hough transform algorithm defines negative theta as the orientation of ρ to the negative x axis, increasing in absolute value in a counter-clockwise direction till the y -axis.

A Hough Transform was performed on the resultant binary image from the Sobel operator. The Hough Transform is a common line detection methodology widely employed in the field of computer vision [9]. The aim of the Hough Transform is to identify lines within the binary image. Each high value of the binary image can be located by its Cartesian co-ordinates (x,y) . For a set of Cartesian co-ordinates there exists numerous straight lines that can be constructed from them. Analytically, these possible line segments can be expressed in a number of forms. A convenient way for describing these possible lines is using the Hesse normal form:

$$\rho = x \cos \theta + y \sin \theta \quad (6.10)$$

where ρ is the length of a normal from the origin to this line; θ is the orientation of ρ with respect to the x axis; and x and y are the Cartesian co-ordinates of the points (Fig. 6.21.) For any point on the solid line depicted, ρ and θ are constant.

In the context of computer vision and identifying edges, the Cartesian co-ordinates of the points that make an edge are known - these are high values in our binary image - but

the (ρ, θ) values are unknown. Thus, if possible (ρ, θ) values defined by the Cartesian co-ordinates of the binary image are plotted, it can be found that the Cartesian co-ordinates map to sinusoids in what is known as the Hough parameter space Fig. 6.22. Points which form a line are evident as they intersect a common (ρ, θ) point.

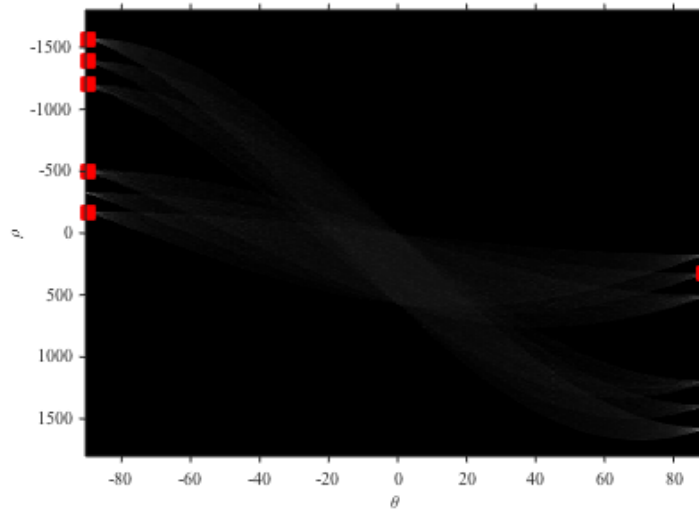


Figure 6.22: The resultant Hough parameter space from the transform performed on the binary image in Fig. 6.20. The maximum points of intersection have been marked with squares.

The graph in Fig. 6.22. space is the result of the Hough transform performed on the binary image in Fig. 6.20. The points of common intersection have been highlighted with square markers. As expected, 6 common intersections were identified close to ± 90 deg, which correlates with the 6 boundary layers from the binary image.

Computationally, the transform is executed by quantizing the Hough parameter space into discrete intervals, also known as accumulator cells. As the transform algorithm runs, each Cartesian co-ordinate (high value in the binary image,) is transformed into a discretized (ρ, θ) curve and the accumulator cells which lie along this curve are incremented. Peaks appearing in the accumulator array indicate a high likelihood that a line exists in that image.

In the resultant accumulator array for our fibre analysis, it was common that more than one line was identified with the same edge, dependent on its thickness in the binary image. Therefore, an extra layer of edge classification was added, whereby lines that were close together were grouped and identified as the same edge. Lines separate more than 50 pixels apart in the y direction were defined as separate edges (Fig. 6.23.) The figure summarises all the image processing steps that the Y-positioning algorithm uses to identify boundary edges of the fibre. The green lines are the individual lines discovered by the Hough transform and the blue lines are the edges identified. The individual lines for the outer boundaries are not visible as the edge is imposed over. Numerous lines can be seen for the cladding-coating 1 boundary by the thick green lines.

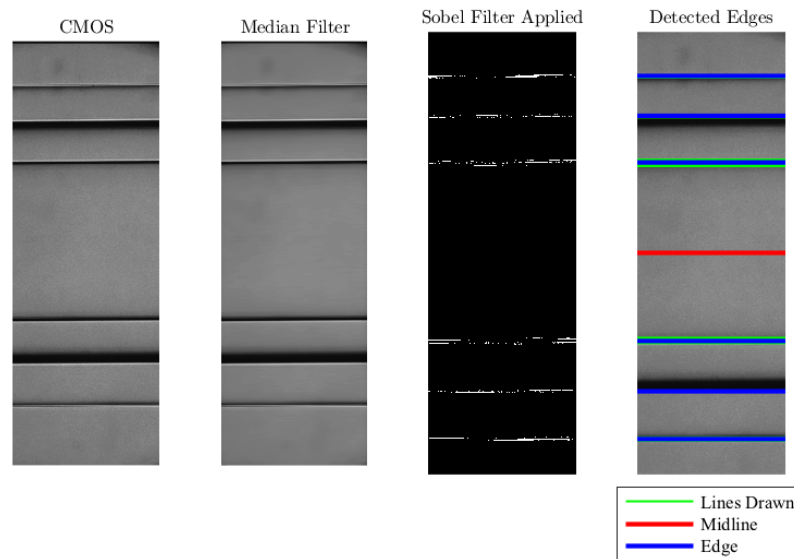


Figure 6.23: A summary of all the image processing steps used for the Y-positioning algorithm (from right to left): the image captured by the CMOS camera; the image after a median filter is applied; the binary image outputted after the Sobel filter and thresholding is applied; and the edges (blue) drawn from the lines (green) that were identified by the Hough transform. The red line is the midline of the image.

6.4.5 Y-Positioning: Search Logic

First, the initial fibre position is assessed. Due to the engineering precision in aligning the wheels within the roller holders, a proportion of the fibre would always be in view after the z -stages lowered it into the oil. Thus, when part of the fibre was in view, the number of edges and their position would be evaluated relative to the midpoint of the image.

If more than 3 edges are located in the top half of the image, the fibre would need to move in the $-y$ direction. Conversely, if more than 3 edges were visible in the lower half of the image, the fibre would be translated in the $+y$ direction. The algorithm would make relatively large steps to ensure the whole fibre was in view.

Once achieved, the script attempted to place the fibre in the centre of the image. The fibre demonstrates a symmetry about the x -axis; one side of the fibre is a reflection of the other. Utilising this symmetry was the basis of the Y-positioning algorithm. Thus, an iterative approach was developed based upon identifying the two cladding-coating boundary edges and placing them equidistant from the a line that runs through the centre of the CMOS image. The two cladding-coating boundaries can be seen equidistant from the midline (red) in the final image of Fig. 6.23 . Once the boundary had been identified by the Hough transform, the y co-ordinate of the edges was noted and their distance from the midline was measured. A symmetry parameter was defined. The

symmetry parameter S , can be mathematically expressed as:

$$S = y_{edge1} - y_{edge2} \quad (6.11)$$

where y_{edge1} is the y co-ordinate of the first cladding-coating boundary and y_{edge2} is the y co-ordinate of the second cladding-coating boundary. The Y-positioning algorithm worked on minimising this parameter as it converges to zero as the fibre approaches the central point. Once minimised, the fibre was ready to be focussed in the z -direction.

6.4.6 Z-Focussing

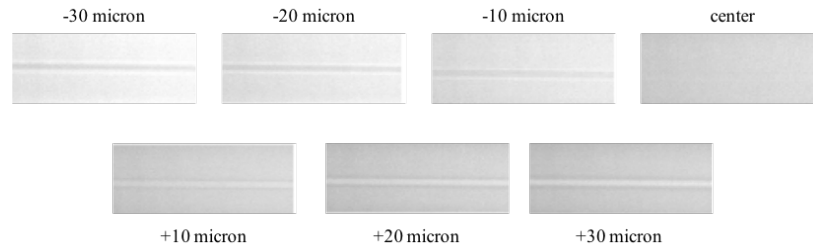


Figure 6.24: CMOS images of the core at heights from -30 micron to +30 micron. When the camera is imaging beneath the core, the core-cladding interface appears white. When the camera is imaging above the core, the core cladding interface appears a dark grey. When at the centre of the core, the core cladding interface is barely visible.

To determine the logic for focussing in the z -axis, understanding of the fibre's visual appearance over changes in height was crucial. The core-cladding boundary exhibits different behaviour depending on the camera imaging plane (Fig. 6.24.) When imaging below the core, the core-cladding boundary appears white. When imaging above the core, the core-cladding boundary appears dark grey. The intensity and thickness of the boundary increases with distance from the centre in both directions, respectively.

Based upon this behaviour, the Z-Focussing algorithm was broken into three parts. First, the direction to the core centre was determined. To do this, an image of the fibre was taken and cropped to show only the core. After cropping, an average of pixel values in the x -direction was taken converting the 2D image into a 1D signal. This process will be referred to as lateral averaging from here on. After, the signal was Fourier transformed and a high pass filter was applied, removing any DC component from the signal.

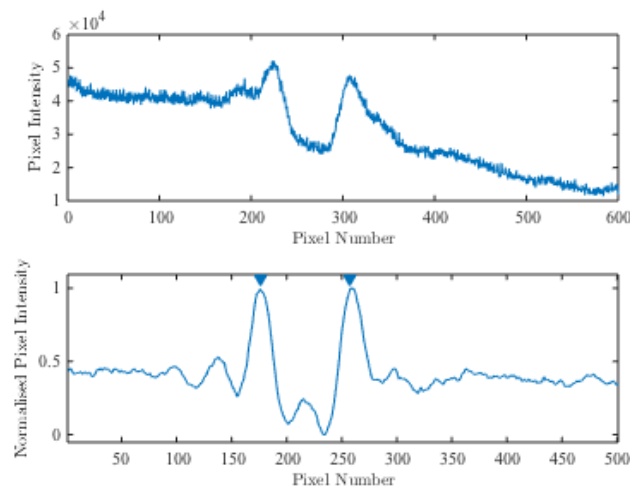


Figure 6.25: Average pixel intensity of the optical fibre at -10 micron (top). The normalised pixel intensity after a high-pass filter was applied (bottom.) The triangular markers show the result of the peak detection algorithm. As peaks were identified immediately, the algorithm has determined the imaging plane lies beneath the core.

The amplitude was then normalized between 0 and 1. This was to allow a peak detection algorithm to find maxima in the signal. If peaks were detected, it was known that the imaging plane was currently beneath the centre of the fibre. Thus, the microscope objective had to move in the positive z -direction. If no peaks were identified, the signal was reflected about the x -axis and normalized. The peak function was applied again. If peaks were identified, it was known that the imaging plane was located above the core centre. Thus, the microscope objective had to move in the negative z -direction. If no peaks were identified, it was known that the fibre was close to the centre.

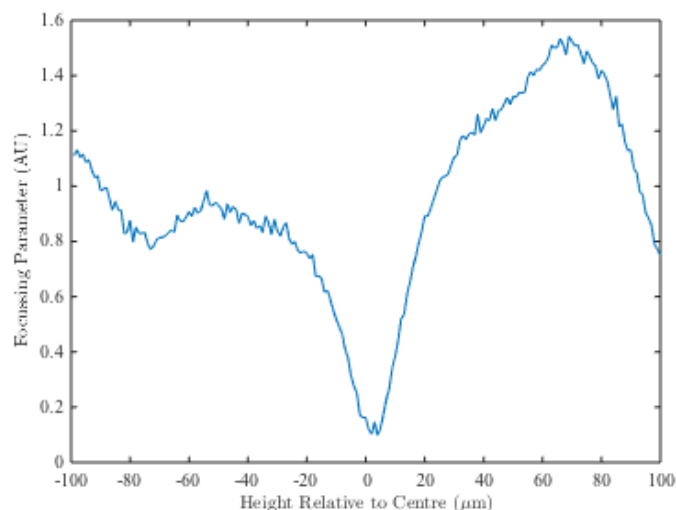


Figure 6.26: A plot of the focus parameter calculated for 201 images from $-100 \mu\text{m}$ below the core to $100 \mu\text{m}$ above the core. A clear convergence to a minima at the position $z = 0$ is visible demonstrating the suitability of this parameter for focussing.

An example of the filtering and peak search when the fibre was positioned -10 micron relative to the centre can be seen in Fig. 6.25. The top graph shows the lateral average of the -10 micron image in Fig. 6.24. The graph beneath shows the result after the top signal was high-pass filtered and normalised. The triangular markers show the result of the peak detection algorithms which have identified the core-cladding boundary. As the peak detection algorithms immediately identified two features, it was known the imaging plane was located beneath the centre of the fibre. The bottom graph has fewer data points than the original signal. This is because the edges of the signal tend to infinity as a result of the Fourier and inverse-Fourier transform. Cropping the signal was essential for calculation of the focussing parameter, which is explained next.

After the direction was determined, the algorithm completed an iterative search to find the central point of the fibre. From Fig. 6.24 it can be seen that the centre is located when the core-cladding boundary is not visible. Based upon this behaviour, a core-cladding focussing parameter was defined:

$$F = C_{max} - \bar{C} \quad (6.12)$$

where F is the focussing parameter; C_{max} is the maximum contrast measured in the image; and \bar{C} is the mean contrast of the image. The focussing parameter was calculated for 201 training data images at -100 to $+100$ micron, relative to the centre of the fibre (Fig. 6.26.) The results show a defined minima at the centre of the fibre. Between -60 and $+70$, a single focussing parameter value relates to two positions, only. Outside

these region, it is possible certain values of the focussing parameter relate to multiple positions.

Thus, the algorithm iteratively stepped every $6 \mu\text{m}$ in the direction towards the centre until the focussing parameter fell beneath a threshold value of 0.2. At this point, the algorithm searched at $1 \mu\text{m}$ intervals from $-4 \mu\text{m}$ to $+4 \mu\text{m}$, relative to the position. The focussing parameter at these 9 positions were calculated and the lowest value was determined to be the centre. The fibre was then moved a set off-set to position it under the laser focal point for inscription.

6.5 Inscription

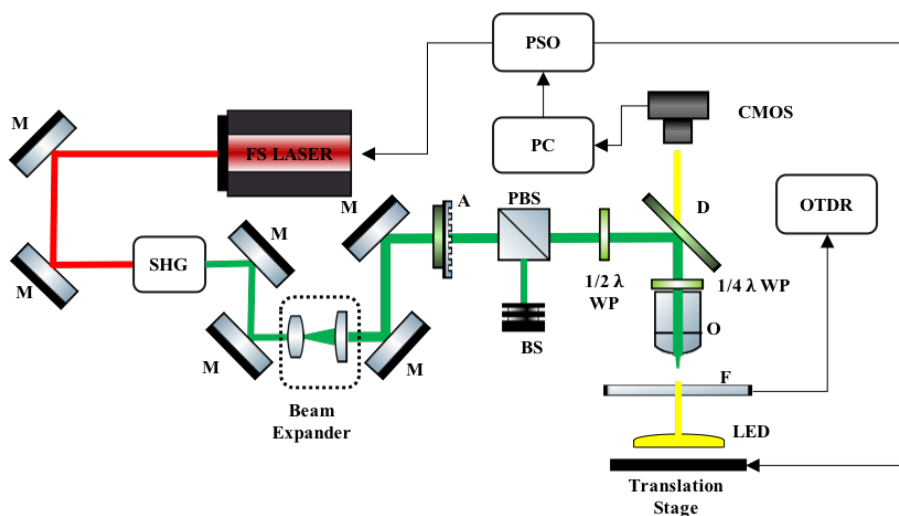


Figure 6.27: A schematic diagram of the femtosecond writing set up used for reflector fabrication. *M* - mirror, *A* - attenuator, *SHG* - second harmonic generation, *D* - dichroic mirror, *PBS* - polarisation beam splitter, *BS* - beam stop, *O* - objective lens, *F* - fibre, *WP* - waveplate, *PSO* - position synchronised output controller, *LED* - light emitting diode, *OTDR* - optical time domain reflectometer, *CMOS* - complimentary metal-oxide semiconductor camera.

Once the fibre is positioned appropriately, the program to inscribe a reflector is triggered. A femtosecond writing set up similar to that used to fabricate waveguides is used (Fig. 6.27.) A 1030 nm solid state Yb:KGW (ytterbium-doped potassium gadolinium tungstate) laser system (Pharos, Light Conversion Ltd) is used for inscription. The laser is frequency doubled to 515 nm. After the second harmonic generation box the laser is guided through a beam expander comprising comprising of a 250 and -25 mm cylindrical lens. The lenses were placed 225 mm from one another. The telescope increased the beam size by a factor of 10. Beam expansion is used to improve the uniformity of the power density across the beam. After the telescope, the following optics controlled the power and polarisation of the beam. A rotatable half-waveplate and polarisation dependent beam splitter is used in conjunction with one another to form an attenuator. After, the laser propagates through a half-waveplate in preparation for a quarter-waveplate, so circularly polarised light can be generated.

Using circularly polarised light has been found to inscribed the smooth, low loss waveguides in bulk silica and lithium-niobate samples samples [10]. In the nanograting

regime with linearly polarised light, small, periodic grating structures have been found to form [11]. With circularly polarised light, the formation of disordered structures have been found to form [12]. Ams et al. found the periodic structures causes larger scattering losses in waveguides compared to the disordered structures [13]. A CMOS camera (IDS, Sony) was placed above a dichoric mirror and microscope objective to optically monitor the writing process. Until now, dry objective lenses had been used to fabricate gratings in sections 3.4.2 and 5.3.1. In the context of the automated set up, this posed a practical issue of removing and replacing a cover slide between each iteration. Given the sub-millimetre thickness of the coverslides, this posed great difficulty. To circumvent this mechanical engineering problem, a low NA oil-immersion lens was used (Olympus). The lens had an iris within it, allowing the NA to be varied from 0.5 - 0.9. For the fabrication of reflectors, the objective was fixed to 0.5 NA to remain in the smooth refractive index regime [14]. Moving to an oil immersion lens also mitigated the potential issue caused by variable thicknesses of oil layers between the fibre and cover slide that may be encountered with a dry objective lens.

6.6 OTDR Monitoring

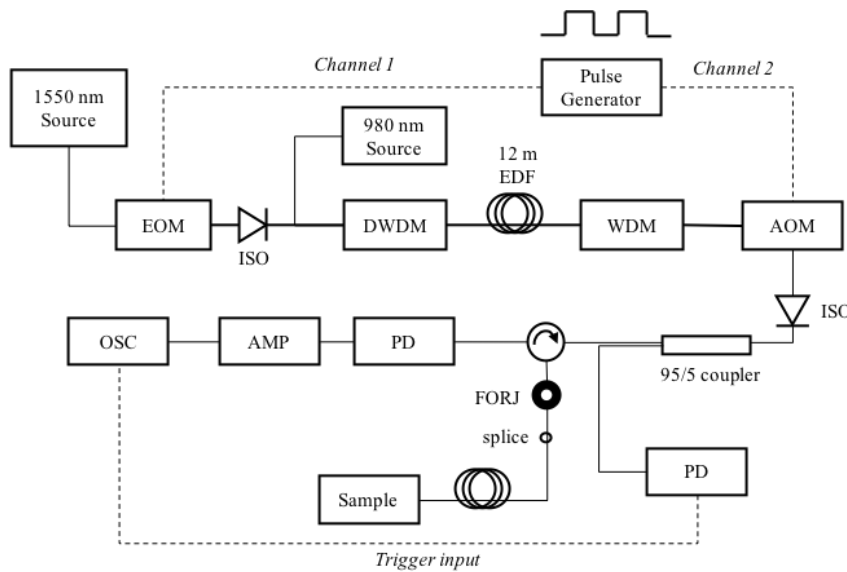


Figure 6.28: A schematic diagram of the OTDR set up used for monitoring the fabrication of the enhanced reflector fibre sample. **EOM** - electro-optic modulator, **DWDM** - dense wave division multiplexer, **EDF** erbium-doped fibre, **WDM** - wave division multiplexer, **AOM** - acousto-optic modulator, **ISO** - isolator, **PD** - photodiode, **AMP** - amplifier, **OSC** - oscilloscope

An optical time domain reflectometry set up was created (Fig. 6.28.) The set up consisted of a 980 nm (QPhotonics) and 1550 nm source (QPhotonics), both operating in a continuous wave regime. The 980 and 1550 nm source had average powers of 300 and 20 mW, respectively. An electro-optic modulator (Lucent Technologies) driven by a pulse generator is used to create pulses on the order of nanoseconds. The two sources are combined with a dense wave division multiplexer and amplified to a peak power of 1 W. A wave division multiplexer is used to separate out the 980 and 1550 nm light. Due to the ~ 10 nm wide bandwidth of the 1550 nm channel, an acousto-

optic modulator (AAOptoelectronics) is used to filter out the amplified spontaneous emission noise created by the erbium-doped fibre amplifier. The acousto-optic modulator is run off a separate channel to the electro-optic modulator and windowed for ~ 70 ns. An isolator was placed after the two modulators to prevent any back-reflected light from damaging the crystals. A 95/5 coupler is used to tap 5% of the pulse for two reasons: first, to measure the parameters of the probe pulse using a photodiode (Thorlabs, DET01CFC/M); and secondly, to trigger a 400 MHz bandwidth oscilloscope (LeCroy) used to measure the back reflected pulse. After the coupler, the pulse is sent into the fabricated sample via a splice to fibre optic rotary joint (Princetel). The back reflected pulse was then redirected via the circulator to an amplified photodiode (Menlo, FPD610 FC-NIR) and a 20 dB, low-noise voltage amplifier (Femto, HVA- 500M-20-B).

Maintaining an optical time domain reflectometry connection to the sample being fabricated was not a trivial task. As the sample is gathered onto the rotating receiving bobbin, an ordinary splice would have led to twisting occurring as the OTDR equipment remains static. Thus, a fibre optic rotary joint is used to permit rotation of the sample whilst the OTDR system remained stationary. A bespoke part was designed using 3D-CAD software and printed using a 3D-printer. The part was designed to hold the rotary joint and screw onto the clamp holding the receiving bobbin in place (Fig. 6.29.) The rotary joint fibre is run through the support arches of the bobbin and spliced to the sample on the opposing side.

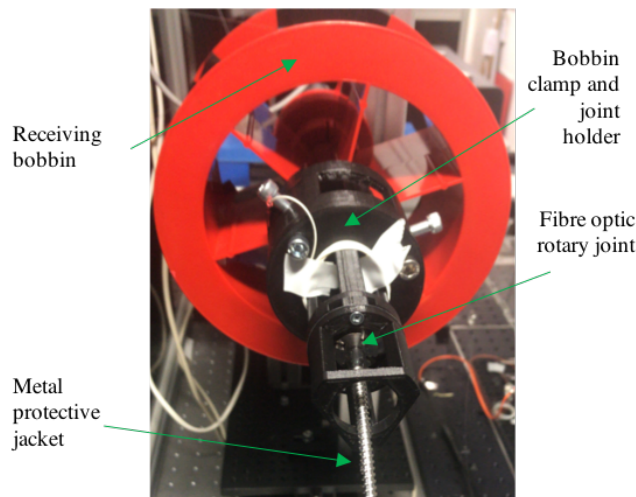


Figure 6.29: An image of the OTDR connection to the sample. The connection is maintained via a fibre optic rotary joint which was secured in place using a bespoke 3D-printed part.

6.7 Conclusions

In summary, an automated fabrication system was designed and assembled. When designing the system, emphasis was placed on ensuring the tension and positioning of the fibre are as consistent as possible. This was to address the reflectivity fluctuations observed in Chapter 5. The fabrication process was divided into 3 parts: winding, positioning and inscription. The winding process was driven by two stepper motors coupled to two fibre bobbins and controlled by an Arduino. The winding process posed an issue analogous to the station stop control problem. As such, terminal iterative

learning control algorithms were implemented on the output of the rotary encoder. This was to ensure the correct length of fibre was wound. A pulley on a low friction rail was monitored by a distance sensor to maintain a constant tension within the fibre. 3D-printed parts and custom wheels were used. Two 1000 iteration tests of the winding system were performed. The error from the rotary encoder converged and subsequently, fluctuated about 0 demonstrating the learning controls were fulfilling their role. The fibre positioning was achieved using basic computer vision techniques. The positioning process was broken into two steps: positioning in the y -axis followed by positioning in the z -axis. The fibre centre could be found to a precision of $\pm 1 \mu\text{m}$. An iterative approach was used. This could be further improved in the future by utilising a template matching model. This would involve storing model images of a fibre. Then, when the first image is captured, a cross correlation over the whole model can be applied to determine its location. Therefore, the movement to central position can be achieved in a single process. The final part of the system was inscription. The optical arrangement for the fabrication of reflectors was detailed. To assess the quality of reflectors, an OTDR arrangement was used. A connection was maintained using a fibre optic rotary joint. The backscatter trace was monitored by a human overseeing the system. Improvements could be made by feeding the output of the OTDR measurement into the MATLAB programme managing the fabrication system. Then analysis could be performed and digital control algorithms could be implemented to maintain the quality of the inscribed reflectors.

Bibliography

- [1] Hicke, K.; Eisermann, R.; Chruscicki, S. Enhanced distributed fiber optic vibration sensing and simultaneous temperature gradient sensing using traditional C-OTDR and structured fiber with scattering dots. *Sensors (Switzerland)* **2019**, *19*, 9–11.
- [2] Askins, C. G.; Putnam, M. A.; Williams, G. M.; Friebele, E. J. Stepped-wavelength optical-fiber Bragg grating arrays fabricated in line on a draw tower. *Optics Letters* **1994**, *19*, 147.
- [3] Bai, W.; Yu, H.; Jiang, D.; Yang, M. All Fiber Grating (AFG): a new platform for fiber optic sensing technologies. *24th International Conference on Optical Fibre Sensors* **2015**, *9634*, 96342A.
- [4] Lefebvre, P.; Vincelette, A.; Beaulieu, C.; Ficocelli, P. Automated manufacturing of fiber Bragg grating arrays. *Optics InfoBase Conference Papers* **2006**, 4–7.
- [5] Westbrook, P. S.; Feder, K. S.; Kremp, T.; Taunay, T. F.; Monberg, E.; Kelliher, J.; Ortiz, R.; Bradley, K.; Abedin, K. S.; Au, D.; Puc, G. Integrated optical fiber shape sensor modules based on twisted multicore fiber grating arrays. *Optical Fibers and Sensors for Medical Diagnostics and Treatment Applications XIV* **2014**, 8938, 89380H.
- [6] Streltsov, A. M.; Borrelli, N. F. Fabrication and analysis of a directional coupler written in glass by nanojoule femtosecond laser pulses. *Optics Letters* **2001**, *26*, 42.
- [7] Hou, Z.; Wang, Y.; Yin, C.; Tang, T. Terminal iterative learning control based station stop control of a train. *International Journal of Control* **2011**, *84*, 1263–1274.
- [8] Lee, J. U.; Yu, S. M. Analytic design procedure of three-mirror telescope corrected for spherical aberration, coma, astigmatism, and petzval field curvature. *Journal of the Optical Society of Korea* **2009**, *13*, 184–192.
- [9] Leavers, V. Which Hough Transform? *CVGIP: Image Understanding* **1993**, *58*, 250–264.
- [10] Nejadmalayeri, A. H.; Herman, P. R. Ultrafast laser waveguide writing: lithium niobate and the role of circular polarization and picosecond pulse width. *Optics Letters* **2006**, *31*, 2987.
- [11] Shimotsuma, Y.; Kazansky, P. G.; Qiu, J.; Hirao, K. Self-organized nanogratings in glass irradiated by ultrashort light pulses. *Physical Review Letters* **2003**, *91*, 247405.
- [12] Hnatovsky, C.; Taylor, R. S.; Simova, E.; Rajeev, P. P.; Rayner, D. M.; Bhardwaj, V. R.; Corkum, P. B. Fabrication of microchannels in glass using focused femtosecond laser radiation and selective chemical etching. *Applied Physics A: Materials Science and Processing* **2006**, *84*, 47–61.
- [13] Ams, M.; Marshall, G. D.; Withford, M. J. Study of the influence of femtosecond laser polarisation on direct writing of waveguides. *Optics Express* **2006**, *14*, 13158.
- [14] Beresna, M.; Gecevicius, M.; Kazansky, P. G. Ultrafast laser direct writing and nanostructuring in transparent materials. *Advances in Optics and Photonics* **2014**, *6*, 293–339.

Chapter 7

Distributed Acoustic Sensing: Characterization of Enhanced Reflectivity Fibre

7.1 Introduction

Distributed acoustic sensing is a rapidly growing area of research driven by its vast range of applications. Today, DAS is employed for perimeter intrusion detection, subsea cable monitoring, oil and gas downhole analysis, pipeline monitoring and structural health analysis [1, 2, 3, 4, 5, 6]. As covered in Section 4.3, sensing methodologies exploiting the Rayleigh backscatter could benefit from an improved signal to noise ratio. A number of solutions have been proposed including weak Bragg grating arrays, continuous grating fibres and enhanced scattering regions [7, 8, 9, 10]. These solutions have been reviewed in depth in Section 4.5.

In Chapter 5, a novel ultra-low loss enhanced reflectivity fibre (ERF) was demonstrated. By utilising the smooth refractive index regime of ultrafast laser micro-machining, reflectors could be inscribed into the optical fibre. The structures are thought to cause a direct Fresnel reflection back along the fibre whilst minimising the light scattered in all other directions. Following this proof of concept, an automated fabrication system was created to fabricate long samples of ERF in 6.

Previous work had investigated the use of femtosecond inscribed scattering voids in distributed sensing measurements [11, 12, 13]. As shown by Yan et al., losses of 0.41 dB/cm were recorded, illustrating the limitation of using scattering voids over large distances. Within this chapter, the ERF is functionally tested and characterised. Samples were produced with the automated fabrication system and characterised with an OTDR measurement to assess their enhancement. After, the samples were functionally assessed within a ϕ -OTDR and OFDR acoustic sensing measurement. The ϕ -OTDR measurement was conducted by Dr Brandon Redding from the Naval Research Labs. The OFDR measurement was conducted by Dr Stephen Kreger from Luna Innovations Inc. Measurements with an unmodified single mode fibre were completed to offer a direct comparison in performance. To further quantify the low-loss nature of the novel

fibre, a sample of 300 reflectors was created for a cutback measurement.

7.2 Experimental Methodology

7.2.1 Reflector Fabrication

All samples were produced with the automated fabrication system detailed in Chapter 6. The methodology was altered from the initial proof of concept in Section 5.3.1. For inscription, a 0.5 NA oil immersion lens was used and the laser frequency was set to 200 kHz. A oil immersion liquid specifically designed for laser interactions was used (Cargille). The oil had a refractive index of 1.545 for 515 nm light at a temperature of 25 °C. Pulse energies did not exceed 30 nJ. This was to ensure writing remained within the smooth refractive index regime [15]. The beam was circularly polarised.

The reflector was intended to be as large as possible to maximise its interaction with the forward propagating mode. The rectangular structure was 35 μm in depth and 83.3 μm wide, centred around the core. A larger structure was not possible as beyond these limits as the fibre coating was susceptible to being damaged. The structure was inscribed at a speed of 0.5 mm/s. A single reflector was inscribed in 60 seconds.

7.2.2 Distributed Acoustic Sensing Measurement: ϕ -OTDR

A ϕ -OTDR system was constructed to test the ERF. A 200 m sample with 10 reflectors, spaced 20 m apart, was created for the experiment. A dual-pulse interrogation set up was employed given its non-local signal rejection and lower sensitivity to laser phase noise. A laser (OE Waves) with a linewidth of <10 Hz was used. An electro-optic modulator was used to generate 20 ns pulses. The electro-optic modulator provided ~ 20 dB extinction. An acousto-optic modulator pulsed at 150 ns was used to provide a further extinction of ~ 50 dB. Subsequently, a 20 ns pulse with a 150 ns pedestal was generated.

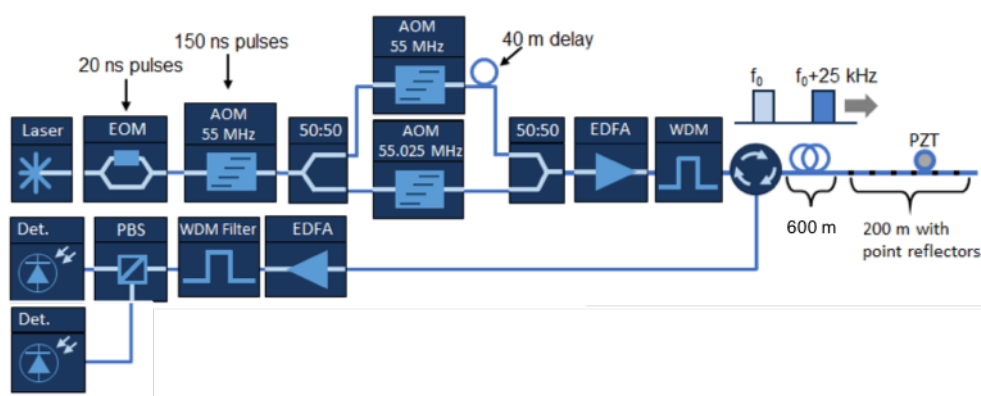


Figure 7.1: A schematic diagram of the dual-pulse ϕ -OTDR arrangement. Two 20 ns pulses, offset by 25 kHz, were combined and launched into the ERF. The back-reflected trace was sent into a polarization diversity receiver. The interference of the two pulses was recorded with a high speed digitizer.

After pulse generation, the pulses were split in half using a 50/50 coupler and injected into an imbalanced Mach Zehnder interferometer. Both arms of the interferometer contained an acousto-optic modulator driven at 55 MHz and 55.025 MHz. Subsequently, the two arms had a frequency offset of 25 KHz. The 55 MHz arm had a 40 m delay fibre inserted. The sample of ERF used in this test had a separation of 20 m. The delay length was set to match the round trip distance between the reflector sites. Hence, sensors could be formed from the light reflected from adjacent reflectors. The relative phase between the two pulses was deduced from the intermediate frequency difference between the two pulses. Then using an erbium-doped fibre amplifier, the recombined pulse was amplified. The pulse had a peak power of 500 mW. Amplified spontaneous emission was filtered out using a 100 GHz wave division multiplexing filter. The lasers were set to a repetition rate of 100 kHz. Using a circulator, the pulse was then sent into the sample. The sample of ERF was spliced after 600 m of standard single mode fibre.

For the distributed acoustic sensing measurement 1 m of fibre, in between two reflectors, was wrapped onto a Piezoelectric transducer (PZT.) The PZT allowed a vibration to be exerted onto the fibre. The backscattered trace was amplified by a second erbium-doped fibre amplifier and filtered using a similar specification wave division multiplexer as before. The backscattered light was then passed through a polarisation diversity receiver. The polarisation diversity receiver minimised the effect of polarisation fading. The interference pattern was recorded on two photodetectors (Thorlabs, PDA10CF). The detectors had a bandwidth of 150 MHz and the data was digitised at a rate of 5 GHz.

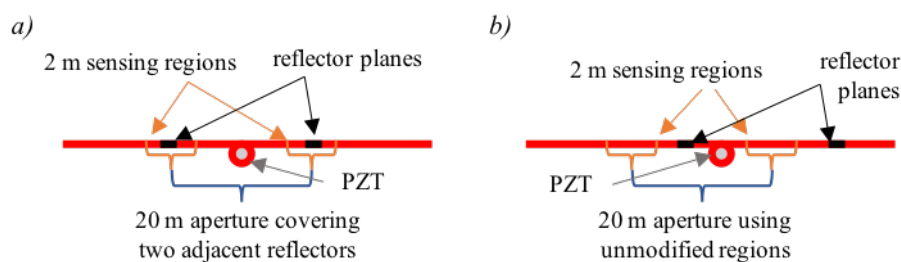


Figure 7.2: A schematic of the sensing regions used to measure the PZT oscillation for a) enhanced reflectors and b) the Rayleigh backscatter from unmodified areas. The sensing regions were 2 m in length and separated by a 20 m sensing aperture.

The arrangement employed enabled measurement of the relative phase between the two frequency offset pulses as a function of position. Therefore, the phase between light back-reflected from a pair of 2 m regions separated by 20 meters could be used for a measurement. The 2 m region was designated by the 20 ns pulse width. The 20 m aperture was dictated by the 40 m delay fibre in the imbalanced Mach Zehnder interferometer. As such, unmodified regions of the ERF can be used to measure vibrations as well as two regions containing reflectors. Therefore, using the same sample, a direct comparison of reflectors and unmodified regions can be made (Fig. 7.2.) By wrapping 1 m of fibre in between to reflectors, sensors made up of reflectors and sensors made up from unmodified regions could be assessed.

7.2.3 Distributed Acoustic Sensing Measurement: OFDR

In this experiment a commercial OFDR system (Luna, OBR 4600) was used to interrogate a sample of 48 reflectors spaced ~ 20 cm apart. The OFDR system consists of two interferometers, a trigger and a measurement interferometer, as well as a polarization sensitive receiver (Fig. 7.3.) The receiver is made up of a polarization beam splitter, 3 wide-band photodetectors, an analogue to digital convertor and a computer. The system uses a tunable laser source swept over a range of optical frequencies. A 90:10 coupler is used, with 10% of the light being sent into a trigger interferometer and 90% being sent into a measurement interferometer. The fibre under test is inserted into one arm of the measurement interferometer and the other arm is used as a reference. The reference arm has a polarisation controller. The polarisation beam splitter has the effect of dividing the incoming light into two orthogonal polarisation states. This technique is used in OFDR to mitigate signal fading due to any misalignment of the two interfering fields [17]. When the laser frequency is tuned, interference fringes related to the reflected signal from the fibre under test are observed at the photodetectors. These detectors are triggered by interference fringes detected at the third photodetector, monitoring the output from the trigger interferometer. Utilising a trigger interferometer in this manner is a well known acquisition technique that helps to mitigate laser tuning errors that could adversely effect the measurement [18].

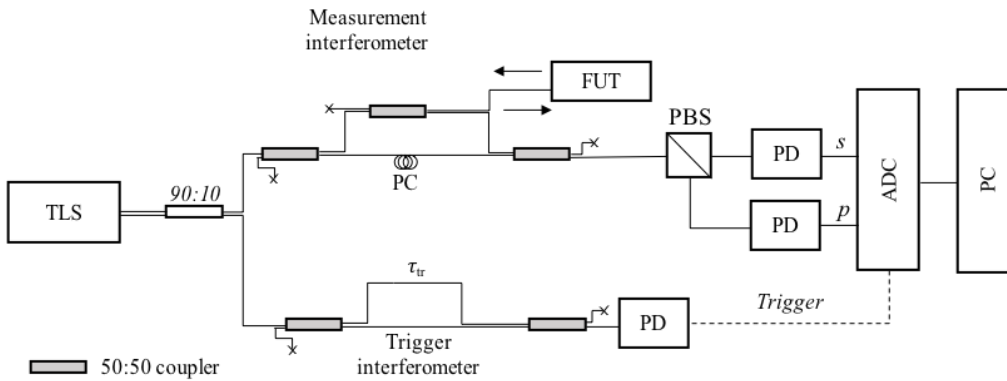


Figure 7.3: A schematic of the Luna OBR 4600 measurement mechanism. The system is made up of a trigger interferometer, a measurement interferometer and a polarisation diversity receiver. **TLS** - tunable laser source, **PD** - photodiode, **FUT** - fibre under test, **PBS** - polarisation beam splitter, **ADC** - analogue to digital convertor **PC** - polarisation controller.

The optical power of the interference pattern for an unmodified fibre can be described by:

$$P(\nu, t) \propto |A_R| + |A_s(\tau)| + 2\sqrt{|A_R||A_s(\tau)|} \cos(2\pi\nu(t)\tau(t)) \quad (7.1)$$

where A_R is the amplitude of the reference arm light; A_S is the amplitude of the back reflected light from the fibre under test, τ is the time-of-flight delay difference between the reference and sensing arm; and ν is the frequency of light as a function of time, t . The frequency of the laser is swept linearly such that:

$$\nu(t) = \nu_0 + \alpha t \quad (7.2)$$

where α is the laser tuning rate. The delay is proportional to the difference in lengths between the two arms of the Michelson interferometer. If the delay is constant along the sensor fibre over time (no vibration is imparted), a Fourier transform of Eq. 7.1

will translate interference fringes which are a function of the frequency of light, into reflection amplitude coefficients as a function of delay. If A_S describes the reflection spectrum from the ERF formed of n reflectors, with each reflector at a different delay from τ_0 to τ_n , the interference pattern would be a sum of interference fringes with periods as a function of frequency inversely proportional to the delays. Hence, a Fourier transform of the interference pattern would produce an array of delta functions in the delay domain.

If the delay of the signal from a reflector is oscillated in time with a frequency f , the delay from the n^{th} reflector can be expressed as:

$$\begin{aligned}\tau_n &= \tau_R(1 + b \sin(2\pi ft)) \\ &= \tau_R(1 + b \sin(2\pi(\nu - \nu_0)f/a))\end{aligned}\quad (7.3)$$

By substituting the time dependent delay Eq. 7.3 into Eq. 7.1, and performing a Fourier transform, the oscillating delay broadens the delta function with a delay spacing of f/α . Thus, this relationship translates the reflector spacing to the maximum vibration frequency that can be discerned. After, if the delay domain data is broken down into each reflector peak, the optical phase can be obtained from an inverse Fourier transform. The transform converts the data to the optical frequency domain, detailing the fluctuations in optical phase along the path of the fibre up to that reflector.

The strain along the fibre can be deduced via an additional spatial derivative. The strain, ϵ is directly proportional to the observed phase difference between two regions, Δx . This can be expressed mathematically as:

$$\epsilon = \frac{(\phi_n - \phi_{n-1})c}{(4\beta\pi n\Delta x\nu_c)} \quad (7.4)$$

where β is a scale factor, ν_c is the central frequency of the laser scan; and n is the group delay refractive index of the fibre.

7.3 Results and Discussion

7.3.1 1 km Sample of ERF: OTDR

A sample of 270 reflectors was fabricated using the automated inscription system. The system was programmed to space reflectors 5 m apart. For inscription, the laser frequency was set to 200 kHz. The 515 nm beam had a pulse energy of 16 nJ recorded after the oil immersion microscope objective. Each reflector inscription (including 5 m winding) took approximately 90 seconds. The 1.35 km sample was fabricated in 7 hours. The sample was then rewound using an industrial winding machine with a 40 g tension. This was to minimise the effect of winding errors, caused by the fabrication system, on the OTDR measurement.

The sample was interrogated with an OTDR measurement. A 1 W pulse was launched into the fibre and the resultant backscatter trace was recorded (Fig. 7.4.) The sample had a region of 10 m that was left unmodified to allow comparison of the reflectors to the Rayleigh backscatter. The final peak at ~ 1.775 km is a Fresnel reflection from the end facet of the fibre. The signal from 1.7 km onwards is the noise level of the oscilloscope. The average noise level was recorded to be ~ -90 dB. A biased

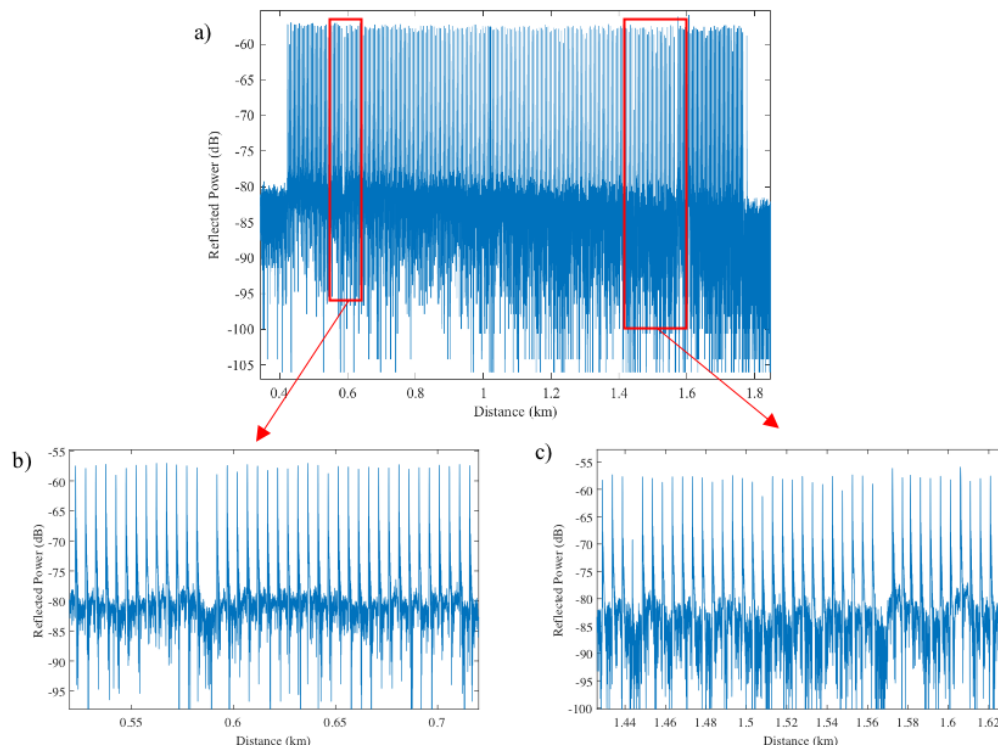


Figure 7.4: a) The OTDR trace recorded from the 1.35 km sample. The sample shows 268 signal enhancements with an average reflection of 22.03 db above the Rayleigh backscatter. b) The OTDR trace from 0.5 to 0.75 km showing an error in the fabrication system. No reflector was inscribed at 0.590 km. c) The OTDR trace from 1.43 to 1.63 km. The trace shows the reflector at 1.45 km was ~ 12 dB lower than anticipated. A reflector was expected at 1.57 km, but due to an error in the fabrication system, no structure was inscribed.

photodetector was used to record the backscattered spectrum. After peaks in signal occurred, the detector caused secondary oscillations, causing the signal to drop below the noise level of the scope. These oscillations cause the signal to fall below -110 dB.

The recorded spectrum shows increases of signal from 0.42 km to 1.76 km caused by the inscribed reflectors. Post analysis of the recorded back-reflected spectra revealed an average reflector separation of 5 ± 0.1 m. From an initial inspection, reflectors 33 and 229 were not visible on the trace (Fig. 7.4b and c.) Enhancements in signal were expected at 0.590 and 1.570 km. The automated inscription system has been programmed to store the camera images before, during and after the positioning algorithms, as well as after inscription. This allows retrospective analysis of the fabrication process. Upon review of the images, no reflectors were inscribed at either of these positions. During inscription of the reflector 32 at 0.59 km, the coating was damaged after inscription (Fig. 7.5) Prior images show that the positioning algorithms were successful and thus, were not responsible for this error. Furthermore, the black distortion of the coating was not present in the images prior to inscription. Therefore, the damage of the coating occurred during inscription. This indicates the laser was being focussed at a shorter focal depth rather than within the core of the fibre. The reasons for this are not clear, but one possibility is a lack of immersion oil.

Upon review of the CMOS images, no reflector was inscribed at 1.570 km due to a

programming error in the fabrication system. When reviewing the files related to this point, no images were stored indicating that the system had encountered an error and the inscription program was not triggered. When the system was restarted, the system was wound to the next position before subsequent inscribing. Hence, no reflector was fabricated at this position. Only one other significant deviation in reflector magnitude was observed at 1.45 km. Reflector 205 was measured to be only 10.73 dB above the Rayleigh, ~ 12 dB lower than the other reflectors. When reviewing the camera images of the reflector, it was found that the structure was inscribed 10 microns off axis due to an error in the positioning algorithms. Why the positioning algorithms were not successful is not fully understood at this point and requires further analysis. The deviation from centre causing lower reflectivity has been reported by Hicke et al. when inscribing void scatterers in single mode fibre [13].

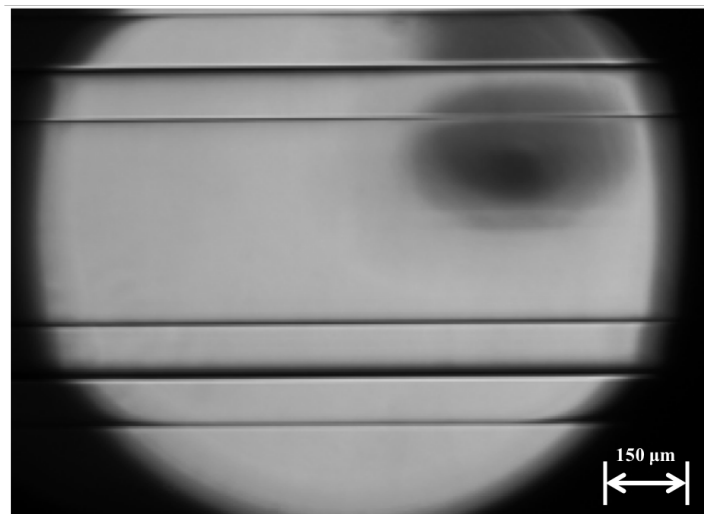


Figure 7.5: A CMOS image of the optical fibre after inscription of a reflector at 0.42 km. No structure was inscribed and damaging of the coating was observed.

A smooth refractive index change can be seen in CMOS images of the inscribed structure. The depth of the structure could not be easily determined from the CMOS images. The structure showed a stronger refractive index change in the central region; evident by the greater contrast in comparison to the ends of the structure. This can be attributed to two factors. Firstly, the spherical nature of the fibre causes coma aberration effects resulting in poorer focussing. The magnitude of this effect increases with distance from the core as the angle of incidence of the beam with respect to the normal increases. The second effect causing this stronger refractive index in the core is the material composition. The core of the fibre is germanium-doped whereas the cladding is pure silica. The refractive index change in pure silica is caused by defect formation and restructuring of the silica matrix [19, 20]. In silica, absorption of femtosecond radiation causes the formation of oxygen deficient and non-bridging oxygen hole centres [21, 22, 23]. In Ge-doped silica, similar oxygen deficient and non-bridging oxygen defects also form [24]. Low concentrations of germanium (~ 1.5 %) allow for absorption at lower energy [24]. Although their thresholds for a smooth refractive index change are similar, the rate of change of index with pulse energy is greater for germanium-doped silica compared to pure silica due to its lower band gap energy. Therefore, we expect, along with the aberration effects, a stronger refractive index change in the core compared to the cladding. Further analysis of the sample would be required to quantify this.

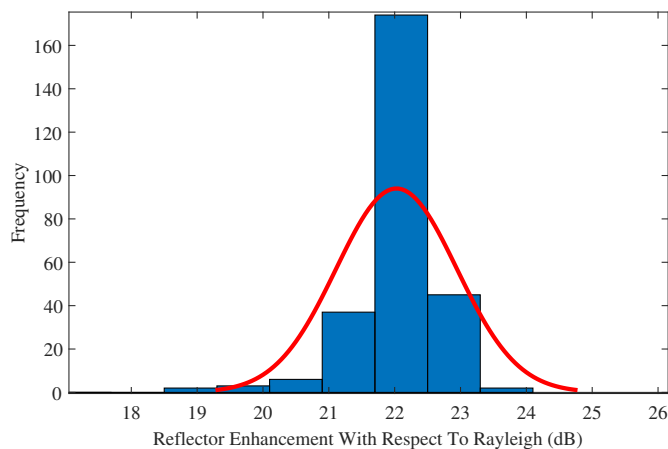


Figure 7.6: A histogram of the reflectivities of the inscribed structures with respect to the Rayleigh backscatter signal. A normal distribution was applied to the data and revealed a mean reflectivity of 22.03 dB and a standard deviation of 0.92 dB.

To assess the consistency of the inscribed reflectors, a histogram of their magnitude was plotted (Fig. 7.6.) A normal distribution fit was applied to the histogram and plotted in red. The reflectivity was recalculated to be expressed as an enhancement with respect to the Rayleigh backscatter signal. The normal distribution revealed a mean reflectivity of 22.03 dB with a standard deviation of 0.92 dB. If a Fresnel reflection is assumed to be the mechanism causing this signal enhancement, a refractive index modification on the order of 10^{-2} was induced. This is consistent with index changes observed when fabricating waveguides [25]. The consistency improvements were attributable to a number of reasons. Firstly, the automated fabrication system allowed precise control of the positioning; the centre of the fibre was found to within $\pm 1 \mu\text{m}$ for all but one reflector (reflector 205.) Furthermore, the system also allowed precise control of the tension of the fibre during inscription due to the addition of the tension control system. The final improvement, compared to the results in Chapter 5, was due to the change in index matching oil. The oil chosen for these experiments exhibited no degradation in optical properties over time. Overall, the combination of these improvements led to a consistency in reflector performance.

7.3.2 Reflector Attenuation: Cut-back Measurement

To evaluate the attenuation caused by the fabrication of point reflectors, a sample of 300 reflectors was produced for a cut-back measurement. The sample was fabricated using the autonomous fabrication system. A pulse energy of 15 nJ was used to inscribe reflectors in a single mode telecommunication fibre (Corning, SMF-28e.) The sample had 3 sections of 100 reflectors, separated by 2 m. The spacing between reflectors was randomised to ensure no coherence was induced. For the cut-back measurement, two APC pigtailed were spliced to each end of the fibre. One end of the fibre was connected to a 1550 nm source (Qphotonics, QDFBLD-1550-50N) and the other to a photodiode (Thorlabs, S122C). The power was measured and after, one section of 100 reflectors was removed. After the removal of a section, the fibre pigtail was spliced back onto the sample and the transmitted power was recorded. Once all sections were removed, the

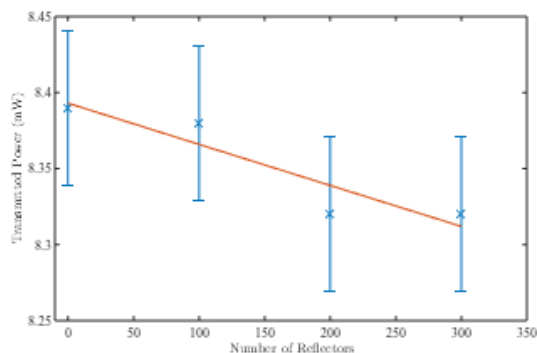


Figure 7.7: A graph of the transmitted power as sections of 100 reflectors are removed during a cutback measurement. An exponential line of best fit was applied to the data and revealed an attenuation coefficient, $\alpha_{ERF} = 3.2 \times 10^{-5}$ per reflector.

power recorded was plotted against the number of reflectors and an exponential line of best fit was applied (Fig. 7.7.) The line of best fit revealed an attenuation coefficient, $\alpha_{ERF} = 3.2 \times 10^{-5}$ per reflector. This corresponds to an attenuation of 1.5×10^{-4} dB per reflector. It may be noted that the transmitted power recorded after 200 and 300 reflectors was equal. This was because the loss from splicing was of comparable magnitude to that from the 100 reflectors.

7.3.3 Distributed Acoustic Sensing Measurement: ϕ -OTDR

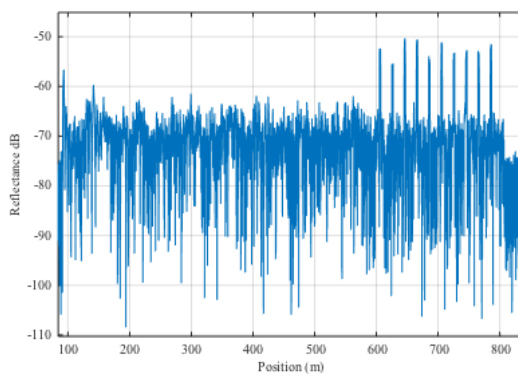


Figure 7.8: An OTDR trace of the ERF used for the ϕ -OTDR measurements. The sample had 10 reflectors spaced 20 m apart. The sample was spliced onto 600 m of telecommunication single mode fibre.

A sample containing 10 reflectors was fabricated using the autonomous fabrication system. The reflectors were placed 20 m apart in a standard telecommunications single mode fibre (Corning, SMF-28e). An OTDR measurement was made to assess the magnitude of enhancement that the reflectors provided (Fig. 7.8.) The fibre was spliced on the end of 600 m of unmodified fibre. The point reflectors had an average reflectivity of -53 dB. Thus, an increase of 17 dB in the signal, with respect to the Rayleigh backscatter, was achieved by the point reflectors. If a Fresnel reflection from

the inscribed structure is the sole mechanism, a change in refractive index on the order of $\sim 10^{-3}$ was induced. Unlike the Rayleigh backscatter signal, the reflectance was found to be independent of pulse duration. The Rayleigh backscatter signal was approximately -70 dB per m.

Using the arrangement in Fig. 7.1, a series of dynamic strain measurements were completed using the PZT. The PZT was located at 790 m along the fibre and driven at 2 kHz. After the back-reflected signal was captured, the raw data was manipulated to provide the interference signal at each measured position along the fibre at a refresh rate of 100 kHz. This meant strain could be evaluated every 10 μ s. Using the 25 kHz frequency offset between the two pulses, the data was demodulated to provide the phase over each 20 m sensing aperture in the fibre (Fig. 7.9a.) The phase was measured over a 10 ms period. The calculated phase is representative of the accumulated phase over the 20 m aperture, centred over that location as demonstrated in Fig. 7.2.

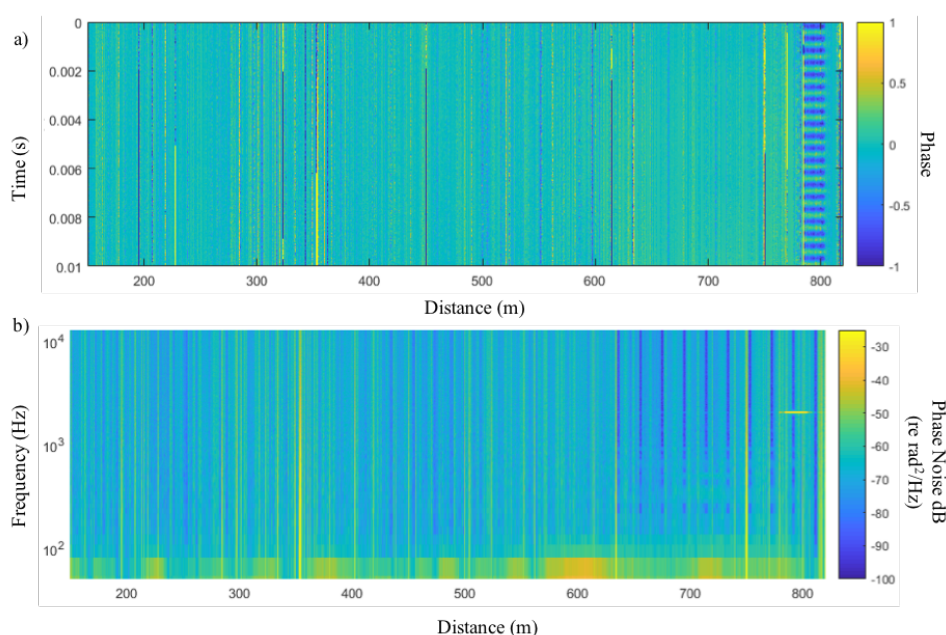


Figure 7.9: a) The measured phase at each position along the fibre. PZT was located between reflector 8 and 9 at ~ 790 m. b) The phase noise power spectral density at each position along the fibre. A 2 kHz signal is visible at ~ 790 m.

The power spectral density of the sensor phase at each position along the fibre was calculated (Fig. 7.9b.) The phase noise is a measure of the performance of the sensing system. Noise in the phase angle of a sinusoid is evident on the power spectral density of the carrier wave, as a spread of the pure carrier frequency. Noise in the frequency domain translates to variations in the time domain. The reflectors had a visibly lower phase noise compared to unmodified regions as shown by the parallel blue regions located between 640 and 820 m. The effect of the PZT is evident in both figures over a ~ 20 m region. For the vibration measurement, the PZT was wrapped between reflector 8 and 9.

Cross sectional plots of the power spectral density at two regions along the fibre were created (Fig. 7.11.) The dynamic strain imparted on the fibre was recorded as a 2 kHz signal by both the Rayleigh scatter sensor and the point reflectors. The point reflectors

demonstrated linear behaviour as a tone was recorded at 2 kHz with a signal to noise ratio of ~ 60 dB, without any harmonic distortion occurring.

No evident signals were recorded at lower or higher harmonic frequencies for the ERF. Reflector 9 and 10 were also assessed during the vibration measurement and for the 2 kHz signal, a >50 dB signal suppression was observed. This demonstrated the enhanced reflectors achieve an excellent non-local signal rejection when used in conjunction with the double probe ϕ -OTDR technique.

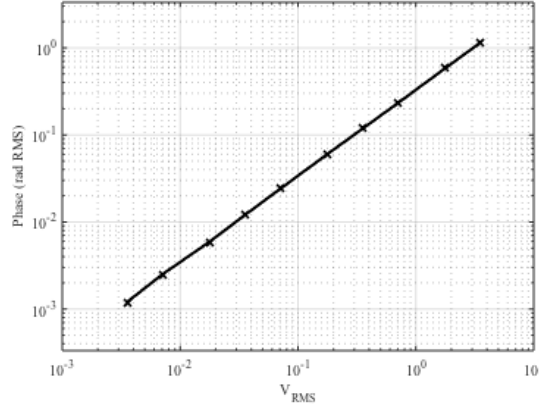


Figure 7.10: The induced phase by the PZT as a function of the drive voltage using reflector 8 and 9.

An additional experiment was conducted whereby the amplitude of the PZT was increased by raising the voltage across it. The measured phase as a function of voltage was plotted (Fig. 7.10). As a sinusoidal voltage and vibration is recorded, the root mean square value (RMS) is expressed. The RMS voltage was raised from 3 mV to 3 V and subsequently, a phase increase from 1.2 mRad to 1.1 Rad was recorded.

The purpose of introducing the reflectors was to achieve a lower noise level. This is evident from Fig. 7.11b. For frequencies above 1 kHz, the point reflectors show an average phase noise ~ 20 dB lower than the sensors formed from the Rayleigh backscatter. For frequencies of 0-100 Hz, there is very little difference between the point reflectors and those from Rayleigh backscatter. For frequencies between 0.1 and 1 kHz, the point reflectors phase noise decreases from -65 to -90 dB. The Rayleigh scatter sensor fluctuates around a constant level of -65 dB.

To evaluate this more thoroughly, the average phase noise for 3 to 13 kHz was calculated. This was intended to be above the drive frequency of the PZT to avoid the imparted vibration to impact the measurement. The phase noise shows a series of minima at the positions of reflectors as shown by the waterfall plot in Fig. 7.9a. The average phase noise from 3 to 12 kHz was -90.9 dB (re rad^2/Hz) compared to an average of -68.7 dB for the rest of the fibre.

From this, the minimum detectable strain ϵ , can be calculated from the measured phase noise as [26]:

$$\epsilon = \sqrt{S_{\phi} \cdot \frac{\lambda}{4\pi n \xi L}} \quad (7.5)$$

where S_{ϕ} is the phase noise spectral density, λ is the wavelength, n is the effective

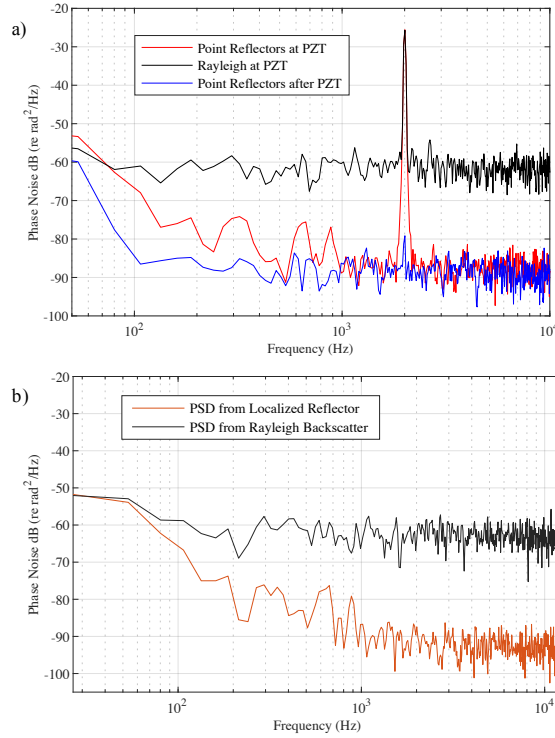


Figure 7.11: a) The phase noise power spectral density at 3 positions along the fibre: a sensor formed from reflectors 8 and 9; a sensor from the Rayleigh backscatter also covering the region wrapped on the PZT; and a sensor formed from reflectors 9 and 10. The sensor using reflector 9 and 10 show a non-local signal suppression of >50 dB. b) The phase noise power spectral density at 2 positions along the fibre: a sensor formed using reflector 2 and 3; and a sensor using the Rayleigh backscatter 2 m after reflectors 2 and 3.

modal index of the fibre, ξ is the elasto-optic coefficient, and L is the sensor aperture. Eq. 7.5 assumes that a uniform strain is exerted over the entire sensing region. From this equation, it was calculated that the minimum detectable strain for a 20 m sensing aperture and a phase noise of -90.9 dB (re rad^2/Hz) is $0.15 \text{ } \mu\text{eHz}^{\frac{1}{2}}$. Furthermore, the standard deviation of phase noise of point reflectors was 4.1 dB lower than that of the Rayleigh backscatter. The Rayleigh backscatter phase noise had a standard deviation of 5.5 dB, whilst the reflector phase noise standard deviation was 1.4 dB. The significant phase noise using Rayleigh backscatter light is a defining characteristic of its intensity distribution. The ERF phase noise is lower due to the defined intensity distribution from the increased reflection points.

The reflectors provided an enhanced signal and minimised noise. Subsequently, the fibre demonstrated immunity to signal fading. In an unmodified single mode fibre, signal fading occurs when light destructively interferes with itself. In ϕ -OTDR techniques, interference fading can significantly affect the phase noise at points along the sensing fibre. In the measurement conducted here, variations of up to 25 dB from the average phase noise occur for the Rayleigh backscatter. In addition, as temperature and strain shift over time, all positions in the fibre will eventually be susceptible to signal fading. Thus, discontinuities in phase and hence, in the measurement of strain occurs as the amplitude of light falls below the noise level of the system.

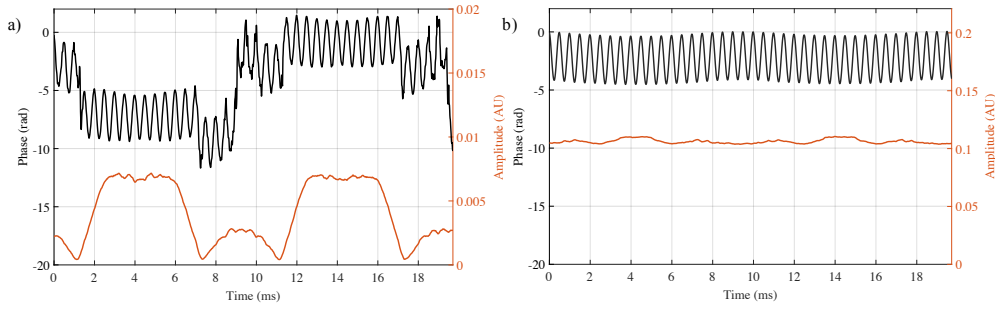


Figure 7.12: The phase and amplitude of a) Rayleigh backscatter sensor b) ERF during an experiment where a PZT was driven at 2 KHz and the seed laser was frequency modulated at 100 Hz with a deviation of 10 MHz.

The immunity to interference fading was demonstrated via frequency modulation of the probe laser. Shifting laser frequency has the same effect that temperature or strain has on the Rayleigh backscatter signal [27]. Hence, modulations of input laser frequency allowed controlled simulation of changing environmental parameters on the ERF.

The amplitude and phase of a Rayleigh backscatter sensor and the ERF were compared (Fig. 7.12). The sensor arrangement as illustrated in Fig. 7.2 was used such that both sensors encompassed the 1 m of fibre wrapped onto the PZT. The PZT was driven at 2 kHz. The laser was frequency modulated at 100 Hz with a shift of 10 MHz. The Rayleigh backscatter sensor is visibly affected by the frequency modulation; the amplitude approaches zero as the frequency is modulated periodically. At these minima in the amplitude, discontinuities in the measured phase occur. In contrast, the ERF shows an immunity to the frequency modulation. Throughout the measurement, the amplitude from the sensor is almost constant. Subsequently, there is no discontinuity in the measured phase of the PZT oscillation. Thus, this observation confirmed the ERF when used in conjunction the dual-probe pulse technique, is immune to signal fading.

7.3.4 Distributed Acoustic Sensing Measurement: OFDR

The Luna 4600 OBR was scanned across the widest possible range, from 1530 to 1616 nm to assess the sample of 48 reflectors. This was completed at first without a vibration imparted on the fibre to analyse the reflectors performance. The scan range meant a sample spacing of $\sim 10 \mu\text{m}$ was possible. The recorded traces were made up of 524k data points (Fig. 7.13.)

For the measurement, a fibre pigtail was spliced onto the sample. This was connected to a pigtail leading in to the OFDR machine using a jumper connector at 3.2 m. The splice to the sample can be seen at 4.2 m. The 48 reflectors were located between 11 and 21 m. During fabrication an unmodified region of ~ 7 m was left prior to the array of reflectors. The return loss of reflectors varied from -48.7 dB to -57.5 dB. The mean of the return loss of the reflectors was -50.5 dB. For an unmodified fibre, an optical scatter level of ~ 123 dB is expected. A return loss of -80 dB was given from a 0.2 m segment, meaning a ~ 43 dB power advantage was attained using the ERF. The collected trace showed a mean spacing of reflectors of 201.63 nm. The largest spacing was measured to be 204.69 mm and the smallest was measured to be 200.45 mm.

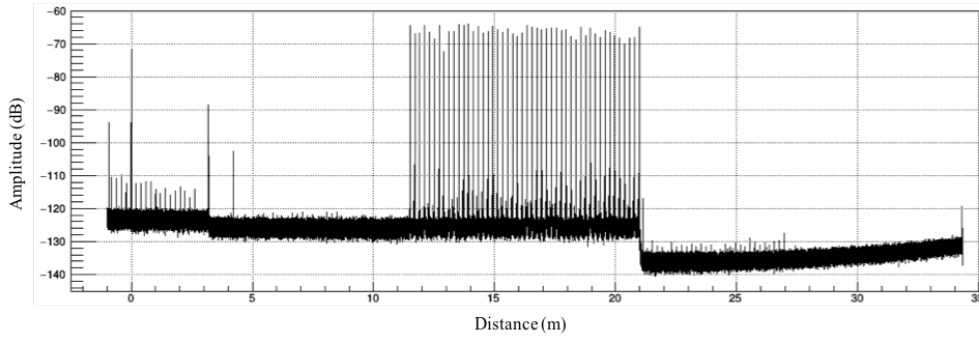


Figure 7.13: The OFDR trace of back reflected light from the 48 point reflectors. The reflectors were positioned 20 cm apart between 11 and 21 m. The reflectors achieved a mean return loss of -50.5 dB.

The reflections measured between -1 and 3 m and > 21 m are artefacts caused by cross-talk between the reflectors. The peaks detected within -1 and 3 m are autocorrelation terms which are produced as one reflector in the array is used as a reference to the others, instead of the true reference path length in the interferometer. The weaker reflections observed passed 21 m are multipath reflection terms.

The maximum detectable vibration frequency is dependent on the sensor element size and the frequency sweep rate of the tunable laser source. In the case of the reflectors, a sinusoidal perturbation generates side-bands in the recorded spectra. As reflectors are placed 20 cm apart, this corresponds to a delay of 2 ns. Hence, a maximum side-band delay of 1 ns is permissible. The maximum detectable frequency, f_{vib} , can then be calculated from:

$$\begin{aligned} f_{vib} &= \alpha \times \Delta\tau_{sb} \\ &= 24 \text{ THz s}^{-1} \times 1 \text{ ns} \\ &= 24 \text{ kHz} \end{aligned} \quad (7.6)$$

where $\Delta\tau_{sb}$ is the side-band delay and α is the laser frequency sweeping rate. The Rayleigh scatter sensor was processed with the same sensor spacing.

For comparison, a standard unmodified single mode optical fibre (Corning, SMF-28e) was used in the same distributed acoustic measurement. Both the Rayleigh scatter sensor and point reflector array was subjected to the same vibration source. In this case, a loudspeaker being driven at 50 Hz was used. The speaker was positioned approximately halfway along the array of point sensors. The acoustic perturbation was generated by guiding the fibre through a tube. The tube was fixed to the speaker's driver. The fibre was attached such that 25 cm of the fibre either side of the speaker was also under tension.

The optical phase as a function of acquisition time along the length of both fibres was plotted (Fig. 7.14.) For the unmodified optical fibre, utilising stochastic Rayleigh scattering, the signal had to be averaged 16 - fold more than the ERF. This was necessary to lower the noise level of the measurement such that the optical phase signal could be successfully unwrapped. The sample spacing on the measurement was 2.32 Hz and the phase noise level was 0.02 radians.

The optical phase noise spectral density for a single sensor at a location along the fibre was also plotted (Fig. 7.15.) The measurement was completed before a vibration

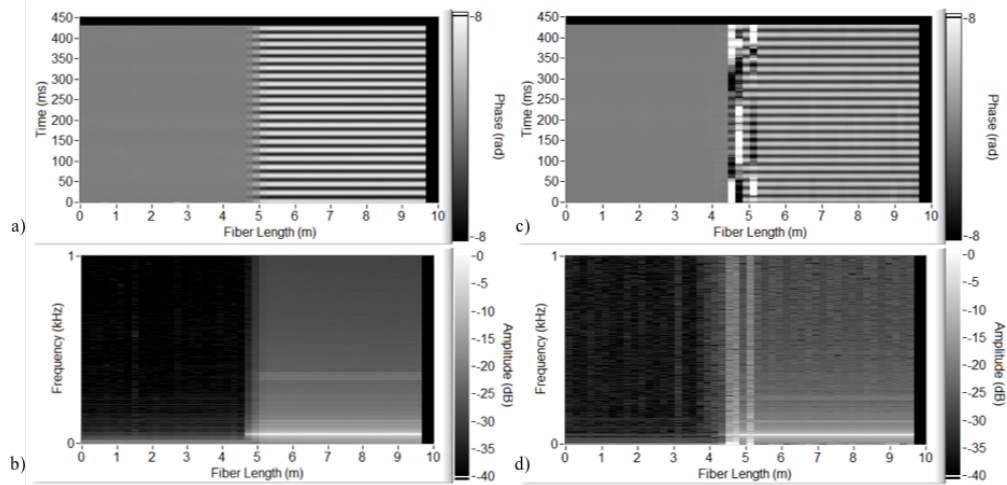


Figure 7.14: The optical phase distribution as a function of distance when measuring a 50 Hz excitation for a) the point reflector array, and c) the Rayleigh scatter sensor. The phase response spectrum from 0 to 1 kHz as a function of distance for b) the point reflector array and d) the Rayleigh scatter sensor.

was introduced. For the Rayleigh scatter sensor, five data sets are visible corresponding to: 1 \times , 2 \times , 4 \times , 8 \times and 16 \times averaging. Without the averaging, the noise floor is 11 dB higher for the unmodified single mode fibre. With the 16 \times averaging the noise floor difference was reduced to 5 dB from the noise floor of the ERF. As the amount of averaging increases, the maximum observable frequency was cut from 24 kHz to 1.5 kHz.

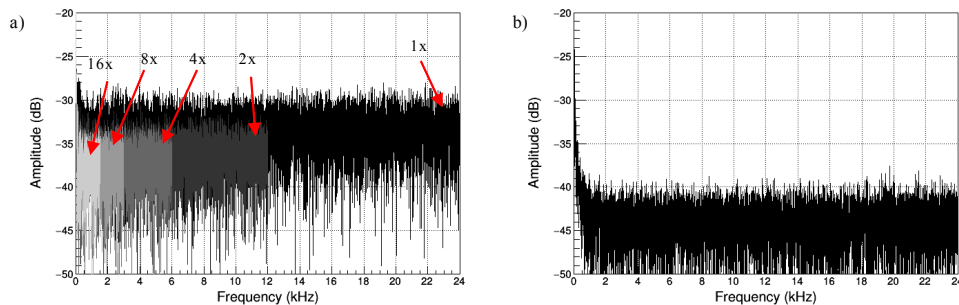


Figure 7.15: The power spectral density at a point away from the imparted vibration for a) the Rayleigh scatter sensor with 1 \times , 2 \times , 4 \times , 8 \times and 16 \times averaging b) the ERF.

Even with 16 \times averaging, the unmodified fibre produced obvious phase errors at 3 positions in between 4.5 and 5.5 m. The measurement of vibrations in an unmodified fibre relies on a constant distribution of the stochastic scatterers. When large strains are applied, this can augment the distribution of scatterers, making it prone to phase tracking errors. The ERF did not produce any clear errors in phase. This is because the point reflector distribution does not shift when large strains are applied, therefore maintaining a consistent phase relationship that can be used to discern the strain imparted upon it. On both fibre measurements, vibrations at \sim 300 Hz were observed. This was thought to be due to environmental noise produced in the laboratory.

7.4 Conclusions

In summary, the ERF was characterised and functionally assessed. A 1.35 km sample containing 268 reflectors was created. The sample was interrogated with an OTDR measurement to assess the reflectivity magnitude of the inscribed structures. Analysis showed the reflectors had an average enhancement of 22.03 dB and a standard deviation of 0.92 dB. 270 reflectors were intended to be fabricated. The fabrication of two reflectors failed due to issues with focussing. The exact reason for this is unknown but it is thought to be caused due to a lack of refractive index matching oil. The sample demonstrated a far superior consistency than the proof of concept demonstrated in Chapter 5. The improvement was due to the development of an extremely precise and accurate automated fabrication system. CMOS images of reflectors showed a smooth refractive index change. However, the magnitude of the index change was greater within the centre of the structure compared to its edges. This is caused by the composition difference between the core and the cladding, as well as a coma aberration effect caused by the cylindrical surface of the fibre. In future, this could be compensated for using a spatial light modulator and altering the power of the laser when inscribing in the core of the fibre. The attenuation of the ERF was assessed using a cutback measurement. 300 reflectors were inscribed and removed in multiples of 100. The measurement revealed each reflector induces a loss of 1.5×10^{-4} dB. This is the lowest attenuation reported for a fibre achieving a >20 dB signal enhancement with respect to the Rayleigh backscatter.

Using the coherent Rayleigh ϕ -OTDR technique, a sample of 10 reflectors spaced 20 m apart was interrogated. In an OTDR measurement the ERF had average a reflectance 17 dB greater than the Rayleigh backscatter. It should be noted that the reflectivity of the reflectors should be balanced with higher return levels without introducing excessive cross talk which could build up from multiple path reflections from many reflectors [28]. The optimum reflectance to minimise cross-talk is a function of spacing and fibre length. The phase noise of the sample was measured to be -90.9 dB (re rad^2/Hz) compared to -69 dB (re rad^2/Hz) using the Rayleigh backscatter. Further to this, the sensor demonstrated linearity with increased amplitude of the PZT oscillation. A non-local signal suppression of >50 dB was observed. When simulating shifts in temperature and strain by modulation of the probe signal, the fibre was unaffected. Thus, it was determined that the fibre was immune to interference fading effects. This permits a relatively simple, single wavelength sensing arrangement. It should be noted that for future applications, the sensing arrangement can be simplified. A single acousto-optic modulator, along with appropriate drive electronics, could be implemented. The modulator could fulfil both requirements of generating a pulse pair and introducing a frequency shift between the two pulses. Another alternative is to use an unbalanced interferometer on the receiver side along with a demodulation scheme to maximize the sensor bandwidth [29].

In the OFDR measurements, a sample of 48 reflectors was interrogated with a Luna OBR 4600 machine. The average return loss of the 48 reflectors was -50.5 dB. The interrogation revealed power enhancements of ~ 40 dB above a standard single mode fibre. Autocorrelation terms and multi-path reflections were observed in the resultant spectrum. The maximum detectable frequency of the enhanced fibre was calculated to be 24 kHz. Using the system, a 50 Hz vibration caused by a loudspeaker was detected. The measurement had a sample spacing of 2.32 Hz and a phase noise level of 0.02 radians. For an unmodified sample, $16 \times$ averaging was required to achieve a similar noise level to the ERF. Subsequently, the averaging meant a frequency range ~ 24 fold

smaller was possible. Even with averaging, the unmodified fibre still incurred phase errors at 3 positions. No phase errors were visible in the measurements made with the ERF.

Overall, the ERF has been demonstrated to have superior qualities in comparison to standard single mode optical fibre, which is commonly used in commercial distributed acoustic sensing applications. The work presented in this Chapter has demonstrated results better than any other enhanced signal fibre reported in literature or commercially available; no fibre achieving a >20 dB enhancement has been reported with a comparable attenuation as has been demonstrated here. Thus, using the smooth refractive index regime of femtosecond micro-machining to fabricate reflector enhancements has been proven to provide an extremely effective, consistent and simple solution for distributed acoustic sensing systems suffering from a poor signal to noise ratio.

Bibliography

- [1] Juarez, J.; Taylor, H. Distributed fiber optic intrusion sensor system. *OFC/NFOEC Technical Digest. Optical Fiber Communication Conference, 2005*. **2005**, *4*, 2081–2087.
- [2] Juarez, J. C.; Taylor, H. F. Field test of a distributed fiber-optic intrusion sensor system for long perimeters. *Applied Optics* **2007**, *46*, 1968–1971.
- [3] Peng, F.; Wu, H.; Jia, X.-H.; Rao, Y.-J.; Wang, Z.-N.; Peng, Z.-P. Ultra-long high-sensitivity Φ -OTDR for high spatial resolution intrusion detection of pipelines. *Optics Express* **2014**, *22*, 13804.
- [5] Frignet, B.; Hartog, A. H.; Mackie, D.; Kotov, O. I.; Liokumovich, L. B. Distributed vibration sensing on optical fibre: field testing in borehole seismic applications. *23rd International Conference on Optical Fibre Sensors* **2014**, *9157*, 91575N.
- [6] Masoudi, A.; Newson, T. P. Contributed Review: Distributed optical fibre dynamic strain sensing. *Review of Scientific Instruments* **2016**, *87*.
- [7] Wang, C.; Wang, C.; Shang, Y.; Liu, X.; Peng, G. Distributed acoustic mapping based on interferometry of phase optical time-domain reflectometry. *Optics Communications* **2015**, *346*, 172–177.
- [8] Handerek, V. A.; Karimi, M.; Nkansah, A.; Yau, A.; Westbrook, P. S.; Feder, K. S.; Ortiz, R. M.; Kremp, T.; Monberg, E. M.; Wu, H.; Simoff, D. A. Improved Optical Power Budget in Distributed Acoustic Sensing Using Enhanced Scattering Optical Fibre. **2018**, *26th International Conference on Optical Fiber Sensors*, TuC5.
- [9] Loranger, S.; Gagné, M.; Lambin-Iezzi, V.; Kashyap, R. Rayleigh scatter based order of magnitude increase in distributed temperature and strain sensing by simple UV exposure of optical fibre. *Scientific Reports* **2015**, *5*, 1–7.
- [10] Liehr, S.; Burgmeier, J.; Krebber, K.; Schade, W. Femtosecond laser structuring of polymer optical fibers for backscatter sensing. *Journal of Lightwave Technology* **2013**, *31*, 1418–1425.
- [11] Liehr, S.; Burgmeier, J. Quasi-distributed measurement on femtosecond laser-induced scattering voids using incoherent OFDR and OTDR. *Fifth European Workshop on Optical Fibre Sensors* **2013**, 87943N.
- [12] Yan, A.; Huang, S.; Li, S.; Chen, R.; Ohodnicki, P.; Buric, M.; Lee, S.; Li, M. J.; Chen, K. P. Distributed Optical Fiber Sensors with Ultrafast Laser Enhanced Rayleigh Backscattering Profiles for Real-Time Monitoring of Solid Oxide Fuel Cell Operations. *Scientific Reports* **2017**, *7*, 1–9.
- [13] Hicke, K.; Eisermann, R.; Chruscicki, S. Enhanced distributed fiber optic vibration sensing and simultaneous temperature gradient sensing using traditional C-OTDR and structured fiber with scattering dots. *Sensors (Switzerland)* **2019**, *19*, 9–11.
- [15] Beresna, M.; Gecevicius, M.; Kazansky, P. G. Ultrafast laser direct writing and nanostructuring in transparent materials. *Advances in Optics and Photonics* **2014**, *6*, 293–339.
- [17] Soller, B. J.; Gifford, D. K.; Wolfe, M. S.; Froggatt, M. E. High resolution optical frequency domain reflectometry for characterization of components and assemblies. *Optics Express* **2005**, *13*, 666.

-
- [18] Glombitza, U.; Brinkmeyer, E. Coherent frequency-domain reflectometry for characterization of single-mode integrated-optical waveguides. *Journal of Lightwave Technology* **1993**, *11*, 1377–1384.
- [19] Chan, J. W.; Huser, T.; Risbud, S.; Krol, D. M. Structural changes in fused silica after exposure to focused femtosecond laser pulses. *Optics Letters* **2001**, *26*, 1726.
- [20] Hirao, K.; Miura, K. Writing waveguides and gratings in silica and related materials by a femtosecond laser. *Journal of Non-Crystalline Solids* **1998**, *239*, 91–95.
- [21] Mao, S. S.; Quéré, F.; Guizard, S.; Mao, X.; Russo, R. E.; Petite, G.; Martin, P. Dynamics of femtosecond laser interactions with dielectrics. *Applied Physics A: Materials Science and Processing* **2004**, *79*, 1695–1709.
- [22] Sun, H.-B.; Juodkazis, S.; Watanabe, M.; Matsuo, S.; Misawa, H.; Nishii, J. Generation and recombination of defects in vitreous silica induced by irradiation with a near-infrared femtosecond laser. *The Journal of Physical Chemistry B* **2000**, *104*, 3450–3455.
- [23] Zoubir, A.; Rivero, C.; Grodsky, R.; Richardson, K.; Richardson, M.; Cardinal, T.; Couzi, M. Laser-induced defects in fused silica by femtosecond IR irradiation. *Physical Review B - Condensed Matter and Materials Physics* **2006**, *73*, 1–5.
- [24] Lancry, M.; Poumellec, B.; Chahid-Erraji, A.; Beresna, M.; Kazansky, P. G. Dependence of the femtosecond laser refractive index change thresholds on the chemical composition of doped-silica glasses. *Optical Materials Express* **2011**, *1*, 711.
- [25] Davis, K. M.; Miura, K.; Sugimoto, N.; Hirao, K. Writing waveguides in glass with a femtosecond laser. *Optics Letters* **1996**, *21*, 1729–1731.
- [26] Kirkendall, C. K.; Dandridge, A. Overview of high performance fibre-optic sensing. *Journal of Physics D: Applied Physics* **2004**, *37*.
- [27] Koyamada, Y.; Imahama, M.; Kubota, K.; Hogari, K. Fiber-optic distributed strain and temperature sensing with very high measurand resolution over long range using coherent OTDR. *Journal of Lightwave Technology* **2009**, *27*, 1142–1146.
- [28] Kersey, A. D.; Dorsey, K. L.; Dandridge, A. Cross talk in a fiber-optic Fabry–Perot sensor array with ring reflectors. *Optics Letters* **1989**, *14*, 93.
- [29] Posey, R.; Johnson, G. A.; Vohra, S. T. Strain sensing based on coherent Rayleigh scattering in an optical fibre. *Electronics Letters* **2000**, *36*, 1688–1689.

Chapter 8

Conclusions

8.1 Summary

In this thesis a number of novel demonstrations were outlined. Firstly, using femtosecond laser writing, a 3rd order fibre Bragg grating (FBG) of ~ 25 dB extinction was inscribed in a high concentration germania fibre ($>40\%$ mol). To the best of my knowledge, this is the first demonstration of a high spectral quality Bragg grating fabricated in high concentration germania fibre. Previous attempts have been reported but no spectra were published [1]. High concentration germania-doped fibres are notoriously difficult to work with using UV-based fabrication techniques due to their highly photosensitive nature. As femtosecond micro-machining relies on intensity dependent non-linear ionization processes, it removes the prerequisite of a photosensitive material. After fabrication, the fibre was thermally tested. It was found stable up to 800° for 30 minutes, with $< 1\%$ movement in the FBG reflectivity. Its sensitivity at both low and high temperatures was greater than the lower concentration fibres reported elsewhere in literature [2]. Based upon these results, there is no theoretical limitation of fabricating Bragg gratings in 100% germania optical fibres.

The second novel element reported in this work was the fabrication of FBGs in a 7 core optical fibre. The femtosecond-material interaction is capable of producing relatively large step-index change. This permits individual grating planes to be inscribed using the point-by-point (PbP) methodology. As each plane is written individually, this allowed direct addressing of individual cores of a multicore optical fibre. Hence, four 3rd order gratings were inscribed into four separate cores of the multicore fibre. A relatively good consistency of extinction ratio was achieved; the maximum variation was 7%. The fibre had a hexagonal distribution of cores with the 7th core running through the centre. The PbP methodology allowed the central core to be addressed as long as no others obstructed the path of the inscription beam. The flexibility of the PbP was demonstrated by inscribing different resonant wavelength gratings in each core. Unlike other methodologies, no intricately fabricated phase mask, nor precise alignment of beams is required. The PbP technique allows fabrication of different grating structures by solely changing the translation parameters of the fibre with respect to the inscribing beam. This was the first report using femtosecond inscription to fabricate core-specific FBGs, with the ability to control the resonant wavelength via the PbP methodology .

The final novel discovery of this thesis was the fabrication of an ultra-low loss, wavelength independent, enhanced reflectivity fibre (ERF). After an initial proof of concept, a sophisticated automated fabrication system was assembled to produce kilometre lengths of ERF. The system utilised computer vision and learning control algorithms. The fibre demonstrated signal enhancements of >20 dB whilst maintaining a fibre attenuation of ~ 0.3 dB/km (with a reflector placed every 1 m). This was measured via a cutback measurement of 300 reflectors. The attenuation measured is lower than any other reported in literature for a ~ 20 dB signal enhancement. By utilising the smooth refractive index regime, it is possible to fabricate intricately designed reflectors, causing a Fresnel reflection of the forward propagating mode. By exploiting this fundamental mechanism, the reflectors are wavelength independent. This could be of great advantage over grating based solutions, especially in harsh environments, where temperature fluctuations can shift the spectral response beyond the bandwidth of the photodetector. The removal of wavelength dependence also removes restrictions on the strain range imposed by grating solutions. The ERF reported here also possesses a performance better than any commercially available solution, suggesting it has the potential to revolutionise the distributed acoustic sensing market. The exceptional performance was demonstrated with the measurement of vibrations using a phase optical time domain reflectometry measurement (ϕ -OTDR). When used in conjunction with the dual-pulse ϕ -OTDR technique, the ERF showed immunity to signal fading. This could be extremely beneficial for perimeter security and oil and gas downhole monitoring applications, where signal fading has a detrimental commercial impact. Furthermore, it demonstrated a ~ 20 dB lower phase noise compared to standard commercial sensing fibre. As well as lower phase noise, the ERF also demonstrated brilliant non-local signal suppression of >50 dB, which again could be of great use for perimeter security applications in locating an intruder accurately. As well as ϕ -OTDR measurements, the fibre was also demonstrated to have superior performance during dynamic strain measurements using an optical frequency domain reflectometer (OFDR). During these measurements, the fibre showed a power enhancement ~ 40 dB greater than a standard commercial sensing fibre. Furthermore, the ERF was able to measure frequencies up to 24 kHz; a standard fibre could only achieve the same noise level with $16\times$ averaging, which in-turn, reduced the frequency range to ~ 1 kHz. Overall, this was the first demonstration of a femtosecond micro-machined, ultra low-loss, wavelength independent ERF, utilising the smooth refractive index regime. The results presented here indicate these are ground breaking result that could be of profound benefit to the DAS industry.

8.2 Future Work

With the novel demonstrations detailed in this thesis, a number of opportunities have arisen that could have tremendous impact with further investigation. The fabrication of gratings in high concentration germania fibre opens up the possibility to fabricate a germania-based Raman amplifier and laser. If two gratings could be fabricated in the same fibre, a cavity could be produced. To be able to produce a cavity, further research would be required into controlling the reflectivity of the inscribed grating. This could be achieved by reducing the magnitude of the induced refractive index modification or by decreasing the length of the grating.

Multicore FBGs remain of great interest for a plethora of applications, in particular wavelength division multiplexing and shape sensing applications. With the automated fabrication system in place, adaptations could be made to accommodate a multicore

fibre. The ability to rotate the fibre would need to be applied to allow each core to be addressable. If this FBGs could be fabricated along the length of fibre, this could be used to produce a sensing fibre for shape sensing applications.

The ERF presents the area of most interest for further research. Although the attenuation was demonstrated with a cutback measurement, it would be advantageous to demonstrate this through the fabrication of a > 2 km sample. Furthermore, the enhanced signal has the ability to increase the range of DAS systems beyond current limits. Recent demonstrations have measured vibrations at 125 km with a 5 m spatial resolution [3]. In principle, the ERF demonstrated here should be able to surpass this to 133 km (with a 1 m reflector resolution.) An investigation to test this theory could be of value to the DAS community. If successful, this could be employed for the monitoring of subsea power cables of offshore wind farms. As of yet, the only demonstration of the fibre has been in lab-based demonstrations. The initial results suggest the ERF is far superior to any other enhanced signal fibre solution. The opportunity to offer a comparison to other solutions was not possible in the time frame of this work. If possible in the future, completing practical field measurements of vibrations in a live environment would be useful. Hopefully, this would certify the initial results reported in this work. Furthermore, if the opportunity to perform the same measurements with other signal fibres arose, a comparison in performance would be extremely valuable.

In addition, the power of femtosecond writing means that inscribing reflectors in other fibre should be possible, as long as their coatings were transparent to the inscription wavelength. In particular, polyimide coated fibre is used widely in the oil and gas industry for downhole monitoring applications due to its ability to withstand temperatures up to 300 °C. The polyimide coating has previously been proven to be transparent at 1 μm for the fabrication of PbP gratings [4]. Hence, it would be good to demonstrate the capability of introducing this technology into other fibres such as this, as well as bend insensitive fibres too. As well as spacing reflectors on the order of meters from one another on a kilometre scale, there is no restriction on placing reflectors on the order of centimetres. With ϕ -OTDR, the resolution of measurement is theoretically determined by the pulse length and the bandwidth of the photodetector. Currently, arrays of Bragg gratings are used to provide distributed strain measurements for the aviation industry. There could be the opportunity to place a higher density of reflectors than are possible with FBGs, due to their lower attenuation. Hence, the ERF could further the resolution limits of current distributed sensing systems. One issue that may be encountered is an increase in cross-talk from multipath reflections. This impact would scale logarithmically, the closer reflectors are placed. This could be countered by lowering the magnitude of the reflectors. A further investigation in collaboration with a DAS specialist would be needed to investigate this possibility.

Bibliography

- [1] Medvedkov, O. I.; Vasiliev, S. A.; Gnusin, P. I.; Dianov, E. M. Photosensitivity of optical fibers with extremely high germanium concentration. *Optical Materials Express* **2012**, *2*, 1478.
- [2] Meltz, G.; Morey, W. W.; Glenn, W. H. Formation of Bragg gratings in optical fibers by a transverse holographic method. *Optics Letters* **1989**, *14*, 823.
- [3] Cedilnik, G.; Lees, G.; Schmidt, P. E.; Herstrom, S.; Geisler, T. Pushing the Reach of Fiber Distributed Acoustic Sensing to 125 km Without the Use of Amplification. *IEEE Sensors Letters* **2019**, *3*, 1–4.
- [4] Mihailov, S. J.; Grobnic, D.; Walker, R. B.; Smelser, C. W.; Cuglietta, G.; Graver, T.; Mendez, A. Bragg grating writing through the polyimide coating of high NA optical fibres with femtosecond IR radiation. *Optics Communications* **2008**, *281*, 5344–5348.

List of Publications

Patents:

1. PCT Patent Application Number: PCT/GB2019/050460 - A fibre with quasi-distributed reflectors for enhanced distributed optical fibre sensing systems

Conference Proceedings:

1. **Donko, A.**, Sandoghchi, R., Masoudi, A., Beresna, M., Brambilla, G. Surpassing the detection limits of current distributed acoustic sensing systems (Conference Presentation). Proc. SPIE Defence & Commercial Sensing 2019, 1
2. Ismaeel, R., Beaton, A., Donko, A., Talataisong, W., Lee, T., Brotin, T., Beresna, M., Mowlem, M. and Brambilla, G. (2019) High sensitivity all-fibre methane sensor with gas permeable Teflon/cryptophane-A membrane. 2019 Conference on Lasers and Electro-Optics Europe & European Quantum Electronics Conference (CLEO/Europe-EQEC), Munich, Germany. 23 - 27 Jun 2019.
3. **Donko, A.**, Gertus, T., Brambilla, G. and Beresna, M. (2018) Applications of ultrafast laser direct writing: from polarization control to data storage. In Laser-Based Micro- and Nanoprocessing XII. vol. 10520, SPIE.
4. **Donko, A.**, Sandoghchi, R., Masoudi, A., Beresna, M. and Brambilla, G. (2018) Low-loss micro-machined fiber with Rayleigh backscattering enhanced by two orders of magnitude. In Optical Fiber Sensors, OFS 2018. vol. Part F124-OFS 2, OSA..
5. Masoudi, A., **Donko, A.**, Talataisong, W., Ismaeel, R., Beresna, M., and Brambilla, G. (2018) New approaches to optical fiber sensing. In Conference on Lasers and Electro-Optics Pacific Rim (CLEO-PR 2018). OSA..
6. **Donko, A.**, Núñez-Velázquez, M., Barua, P., Sahu, J., Beresna, M. and Brambilla, G. (2017) Point-by-point femtosecond laser inscription of Bragg gratings in high NA (>0.4) germania-doped optical fibre. 5th Workshop on Specialty Optical Fiber and Their Applications, Limassol, Cyprus. 11 - 13 Oct 2017. 3 pp .

Journal Publications:

1. Redding, B., Murray, M., **Donko, A.**, Beresna, M, Masoudi, A., and Brambilla, G. (2020) Low-noise distributed acoustic sensing using enhanced backscattering fiber with ultra-low-loss point reflectors. Opt. Express 28(10), 14638-14647 (2020)

2. **Donko, A.**, Beresna, M., Jung, Y., Hayes, J., Richardson, D. J. and Brambilla, G. (2018) Point-by-point femtosecond laser micro-processing of independent core-specific fiber Bragg gratings in a multi-core fiber. *Optics Express*, 26 (2), 2039-2044.
3. **Donko, A.**, Núñez-Velázquez, M., Barua, P., Guzman Cruz, F., Ismaeel, R., Lee, T., Sahu, J., Beresna, M., and Brambilla, G. (2017) Femtosecond inscription and thermal testing of Bragg gratings in high concentration (40 mol%) Germania-doped optical fibre. *Optics Express*, 25 (26), 32879-32886.